TECHNOLOGICAL ATTRACTION POLES

FINAL REPORT

CONTROLLED STRAINING TESTS FOR THE ADHESION AND DAMAGE RESISTANCE OF LASER CLADDINGS (COSTA)

PA/28

K. Van Acker
Flemish Institute for technological research (VITO)
F. Delannay
University Catholique de Louvain (UCL)
A. Dhooge
Belgian Welding Institute (BIL)
K. De Bruyn
WTCM
B. Clyne
University of Cambridge

Compiled by K. Van Acker
K.U.Leuven

February 2006

BELGIAN SCIENCE POLICY

Rue de la Science 8
Wetenschapsstraat 8
B-1000 Brussels
Belgium
Tel: +32 (0)2 238 34 11 – Fax: +32 (0)2 230 59 12
http://www.belspo.be

Contact person:
Dimitri Harmegnies
Secretariat: +32 (0)2 238 37 61

TECHNOLOGICAL ATTRACTION POLES

FINAL REPORT

Controlled Straining Tests for the Adhesion and Damage Resistance of Laser Claddings - COSTA -

PA/67/281

Names of the promoters - Institution/Organisation
K. Van Acker – Flemish Institute for technological research (VITO)
F. Delannay – University Catholique de Louvain (UCL)
A. Dhooge – Belgian Welding Institute (BIL)
K. De Bruyn –WTCM
B. Clyne – University of Cambridge

Compiled by K. Van Acker, K.U.Leuven

February 2006

Rue de la Science 8
Wetenschapsstraat 8
B-1000 Brussels
Belgium
Tel: +32 (0)2 238 34 11 – Fax: +32 (0)2 230 59 12
http://www.belspo.be

Contact person:
Dimitri Harmegnies
Secretariat: +32 (0)2 238 37 61

Executive summary

COSTA is a completed project in the framework of the technological attraction poles (TAP) program of the Federal Science Policy Office. The ultimate goal of the project was to develop a quantitative and accessible method, suitable for standardization, for the determination of damage resistance and adhesion of thick hard coatings on metals, such as laser clads. The method focused on is the controlled straining test. This method is applicable for a wide variety of brittle coatings on more ductile substrate. In this project a derivative of the method is developed and optimised for laser clads and plasma electrolytic oxidation coatings.

An extended literature survey conducted in the beginning of the project shows there was no suitable test method available for the assessment of the adhesion of those coatings. Even promising methods such as the interfacial indentation test, explored as well in this project, are not suited for the coatings studied here. The project aimed to fill up the gap of adhesion testing for thick well-adherent coatings.

Thorough examination of the coatings has been performed, including microstructural characterisation, mechanical and internal stress determination. An overview has been made of the available mechanical test methods for intermediate and thick coatings and evaluated on the laser clad coatings and PEO coatings studied in this project. It can be concluded that the multiphase thick coatings, as LC coatings are, are extremely difficult to characterise, contrary to the general feeling that thick coatings are almost bulk materials and that the bulk test methods should apply. The internal stress can even only be estimated by developing complex models for the distortion during the deposition.

Four-point bending adhesion testing and pure mode I adhesion testing of coated substrates are the most obvious set up to impose a controlled straining. They were thoroughly examined, since the calculation of the adhesion is more straight forward but only yielded lower boundary values for the adhesion strength.

Another way of imposing a controlled straining on a coating is by performing a tensile test. The classical set-up in which (thin) coatings are strained until the crack density reaches a saturation level was not useful since the maximum saturation crack spacing cannot be reached. Moreover, in such method the determined value of the interfacial shear strength is very much dependent on the model used for the stress distribution in the coating between the cracks, and it doesn’t take possible delamination at the interface into account.

The full fragmentation test method has been further explored with the use of image correlation and SEM micro-tensile tests. It was found that the plastic strain in the substrate will be sufficient to propagate the interfacial debonding after a first transverse crack when coating and substrate have a critical thickness ratio, depending on the physico-mechanical properties of the materials as well as the interfacial properties.

A new approach of the controlled straining test has been derived from these experiments. The principle is to decreasing the substrate thickness until a stable interfacial crack growth at the interface after a first transversal crack is obtained. Single cracking followed by delamination has been obtained in a controlled way in the laser clad coated samples. An analytical model has been proposed to calculate the interfacial toughness from the plastic properties of the substrate and the elastic properties of both coating and substrate. This model yields an upper bound of the interfacial toughness. The resulting toughness values may be compared to the toughness of ductile metals.

FEM modelling has been used to calculate the exact interface toughness based on the force needed for the stable delamination. A FEM with cohesive zone at interface is developed to measure the exact interfacial toughness. The model results for the tensile debonding stationary force have been compared with experiments and show the same dependency of the substrate thickness. The calculated value for the interfacial fracture toughness is of the same order of magnitude, but lower than the analytical values which constituted an upper bound.

A modelling tool has also been developed for the prediction of curvature and internal stress generation during cladding and after cooling to room temperature. The results of the 3D modelling show that laser clad coating is in compression due to the bending of the substrate. Comparisons between measured and simulated thermal fields and specimen deflection histories indicate that the main features of residual stress generation in this type of system have been captured in the model.

Finally, the procedure for testing the coatings by the here developed strain-induced delamination test method has been proposed at CEN and a work item has been opened to standardize the method. A round robin with 6 participating laboratories has been set up and the results show an acceptable repeatability and reproducibility of the test results, which confirms the power of the proposed method.

Contents

Symbols and Abbreviations

4PB	four point bending test
AE	acoustical emission
EDX	energy dispersive spectrum
SEM	scanning electron microscope
IET	impulse excitation technique
LC	laser clad
LVDT	linear variable displacement transducer
PEO	plasma electrolytic oxidation
SEM	scanning electron microscope
TEM	transmission electron microscope
TT	tensile test
XRD	X-ray diffraction
b	width of the specimen
c	phase velocity
ε	strain
E	Young's modulus
Γ	resistance to crack propagation, interfacial toughness
G	strain energy release rate
H	hardness
h_c	thickness of the coating
h_{si}	initial thickness of the substrate
h_{sf}	final thickness of the substrate
ν	Poisson's coefficient
ρ	density
σ	stress
ω_t	dimensionless energy release rate
W	work

1 INTRODUCTION

Recent developments in coating technology enable the deposition of strongly adherent thick (>50 μm) coatings. Metal matrix composite coatings containing carbides are ideal for components subject to heavy abrasive wear. An emerging deposition technique for such wear resistant cemented carbide coatings is laser cladding. Another example of a very promising coating technique for light metals is the plasma electrolytic oxidation. Adhesion and damage resistance is improved drastically compared to the classical thermal sprayed coatings.

Whereas known test methods can be applied to prove the outstanding abrasive and adhesive wear properties of these newly developed thick coatings, standard test methods are lacking for the evaluation of the adhesion. In this work, a new approach is presented to measure the resistance of such coatings to debonding from the substrate.

The prevention of damage formation, such as through thickness cracking and interfacial debonding leading to delamination or spallation indeed is a key aspect in the development and design of coatings. Since the performance of coatings often depends on the bond strength between coating and substrate material, it is essential to quantify the adhesive strength of a coating so as to guarantee the overall quality and reliability of the final product.

Most existing adhesion test methods however are at best semi-quantitative assessments of coating/substrate adhesion and are not standardised. A few tests, such as the direct pull test normal to the coating which makes use of adhesives, are suitable for thick coatings, but are able to measure adhesion only of weakly adhered coatings. Modern anti-wear coatings have much higher adhesion levels than can be probed by this method. However, there is a clear need for better understanding of the adhesion of such well-adherent thick coatings and for a quantitative test method. Only a few attempts have been made to assess the adhesion strength of laser clads [1],[2].

The COSTA project aimed to validate simple and cost effective controlled straining tests. The ultimate goal of the project was to attain a quantitative, accessible and standardized method for the determination of damage resistance and adhesion of thick hard coatings on metals.

2 OBJECTIVES

The ultimate goal of the project is to have a quantitative, accessible and standardized method for the determination of damage resistance and adhesion of thick hard coatings on metals, such as laser clads. The method focused on is the controlled straining test. This method is applicable for a wide variety of brittle coatings on more ductile substrate. In this project the method will be further developed and optimized for laser clads.

The specific objectives are:
- the optimization of the observation and detection methods (acoustical emission, optical microscopy) for the progressive coating cracking during the straining test
- a study of the optimum specimen preparation, influencing test parameters and material characteristics
- the evaluation of suitable models for the determination of quantitative values for the adhesion and the damage resistance
- the preparation of test procedures making standardization possible.

3 THICK WELL-ADHERENT COATINGS

3.1 Introduction

The aim of the project was to find a proper quantitative test to evaluate the adhesion of thick well-adherent coatings. In recent years, several new classes of thick coatings have been developed, with a superior adhesion. These coatings are in first instance aimed to protect a substrate against (heavy) wear and corrosion.

A rough classification of thick (>50 µm) coatings is given in figure 1. Coatings belonging to the well-adherent thick coatings mainly are laser clad and PEO coating (both studied in this project and presented in more detail underneath), and HVOF coatings.

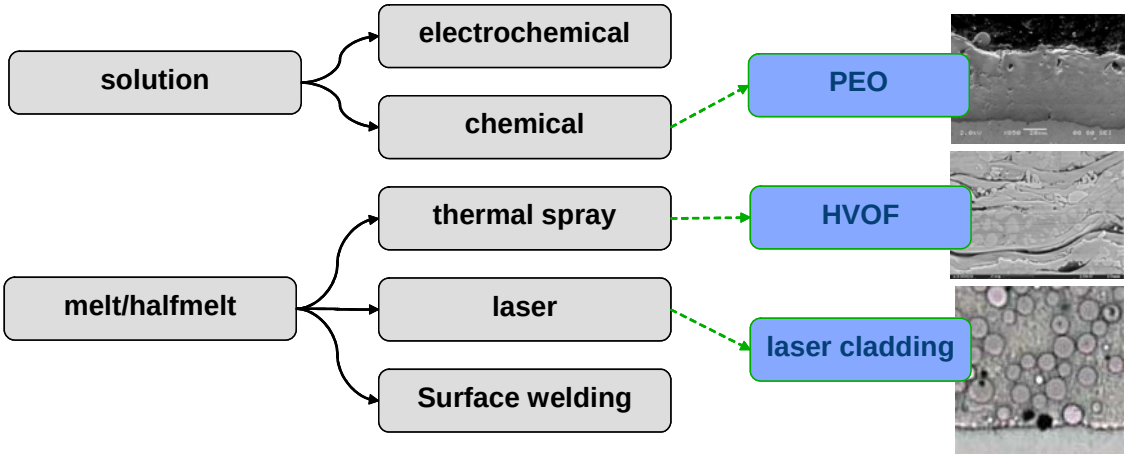

Figure 1: Classification of thick coatings. Examples of well-adherent thick coatings are given at the right.

3.2 Laser clad coatings

Laser cladding is the technique in which a layer is deposited on top of the substrate by supplying metallic and/or ceramic powder in the laser beam (see figure 2 and 3). The particles fully or partially melt in the beam and form a metallurgical binding with the substrate when deposited. Examples of the successful use of laser cladding are wear resistant parts on motor components for the automotive and the aerospace. The application of laser clads with hard surfaces leads to longer component life times and hence of saving of materials.

Compared to conventional methods, laser cladding benefits from a low heat input, an excellent adhesion through a metallurgical bonding, a low degree of dilution, and the weldability of practically all metallic alloys. Furthermore, it is also possible to deposited complex and exotic material combinations. The resulting laser coatings are particularly suited to combine the high mechanical strength, toughness and low cost of the base material with excellent corrosion, wear resistance and high temperature properties of the coated surface. The major disadvantage nowadays if the speed of the laser clad process which is quite slow, and is not well suited for mass production.

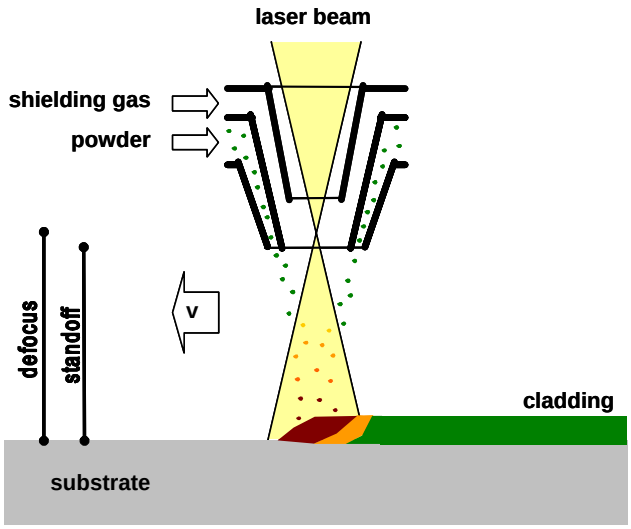

Figure 2: Schematical presentation of the laser cladding procedure.

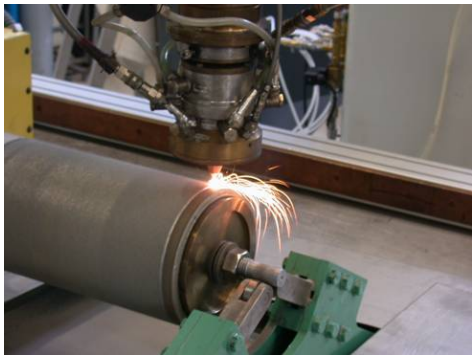

Figure 3: Example of coaxial laser cladding on a tube.

The coatings used in this project consist of a metal matrix containing homogenously distributed very hard ceramic particles. More specifically, they consist of a metallic Ni matrix in which 45 vol% spherical WC particles are embedded and they are deposited by laser cladding. Laser cladding is the technique in which a layer is deposited on top of the substrate by supplying metallic and/or ceramic material. The laser - a 6kW CO2 laser is used in this study - heats the particles and melts the binder phase (Ni) during the deposition on the substrate. The used parameters are 3000 W power, cladding speed of 750 mm/min and powder feed of 26 g/min. A typical thickness of such a coating is 800 µm. They are deposited on a stainless steel plate, type AISI304. The resulting coating, as shown later, is a dense and well adherent metal matrix composite layer.

3.3 PEO coatings

Plasma Electrolytic Oxide (PEO) coatings are hard, dense, wear-resistant, and well-adhered oxide coatings for metals such as aluminium and magnesium. The process by which they are grown may also be referred to as micro-arc oxidation (MAO) or spark discharge anodizing. Essentially, it involves the modification of a conventional anodically grown oxide film by the application of an electric field greater than the dielectric breakdown field for the oxide. Discharges occur, and the resulting plasma-chemical reactions contribute to the growth of the coating. More significantly, local conditions of heat and pressure sinter and anneal the coating. Rapid cooling also modifies the oxide, resulting in a complex mixture of amorphous material and nanocrystalline phases.

The process may be applied to any valve metal such as aluminium, magnesium or titanium, and to a wide range of their alloys. Coating properties depend on the substrate alloy, but also on the electrolyte used and on the many parameters of the electrical system. On aluminium, dense alumina coatings (approximately 3% porosity) up to 130 microns thick can be formed, but more porous coatings up to 600 microns in thickness can also be formed by using different electrolytes. Typical alumina coatings consist of a relatively dense polycrystalline layer of alpha-alumina, with a softer, more porous layer of gamma-alumina formed on top.

Figure 4:. 10 kW laboratory equipment for the production of PEO coatings

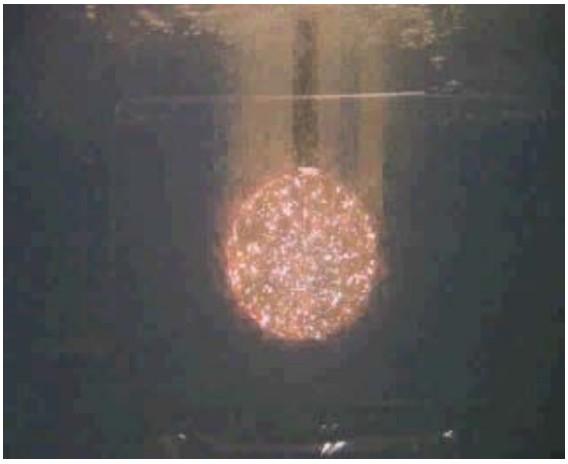

Figure 5: The plasma electrolytic oxidation is a discharge drive process.

4 INTERNATIONAL CONTEXT OF ADHESION TESTING

4.1 Introduction

A literature survey has been conducted in order to situate the project in the international context. In particular, two topics have been followed in detail in the domain of the project research:

- the existing adhesion tests for thick coatings (>50 μm) and the results
- the available methodologies and results of controlled straining tests, mainly on thin brittle coatings

It will be seen none of the existing adhesion tests is valid on the well-adherent thick coatings studied in this project.

4.2 Adhesion tests on thick well-adherent coatings

4.2.1 Introduction

A general overview of adhesion tests on coatings is given in figure 6. Scratch testing, laser spallation and surface indentation are typical adhesion tests for thin coatings. They actually are of no use for thick coatings. The most frequently used tests for thick coatings (>50 μm) are the pull off test, the Ollard test, pure mode I test and 4 point bending test. However, these tests are only applicable on poorly adherent coating, such as thermal sprayed coatings. Four point bending has been extensively tested on well-adherent coatings during this project, without the desired results. Interface indentation has been explored too, without any acceptable result neither. Therefore, the fragmentation test developed for thin brittle coatings has been further adapted for the studied coatings. As in part 5 can be read, this test did give satisfying results neither. It turned out that a completely new method, the strain induced delamination, had to be developed during the project, which was not described in the literature yet.

Adhesion tests	Qualitative	Quantitative	
		Force based	Crack length based
Scratch test	•		
Laser spallation			•
Surface indentation	•		(•)
Interface Indentation	•		(•)
Pull off		•	
Ollard test		•	
Pure Mode I test		•	
4PB Delamination		•	
Fragmentation test	•		(•)
Strain induced Delamination		•	

Figure 6: Overview of different adhesion test methods.

Underneath, the (poorly available) literature on adhesion testing on the two types of studied coatings, the laser clads and the PEO (plasma electrolytic oxidation) coatings, is discussed in more detail.

4.2.2 Laser clads

Several articles are published on characterisation of laser clad coatings, the most recent articles are given in the references [3-10]. They mainly report on microstructure, hardness and wear resistance and the correlation of these properties. An interesting report by Huang[3] describes the dependency of the wear resistance of WC/Ni laser clad layers upon the shape of the WC carbides. Layers with crushed, angular carbides are found to be slightly more wear resistant than coatings with spherical carbides.

The adhesion of the laser clad coatings is in these articles only qualitatively assessed by microstructural investigation of pores and interfacial cracks in cross sections and of the presence of transversal cracks.

Two publications report with more details on adhesion studies of laser clad coatings, both of the group of prof. Dahotre (Tennessee). Kadolkar[2] implements 4PB on laser clads to study the cohesive strength of the coating (force displacement curves are used) and Katipelli[1] investigated the cracking a TiC laser clad coating on Al6061 substrate (Nd-Yag).

4.2.3 Keronite coatings

The Plasma Electrolytic Oxidation process also known as the Keronite process is a modification of the conventional anodizing process. This modification is based on applying high AC voltages that induce an electric field greater than the breakdown field for the growing oxide. The process requires only low concentrations of dilute non-toxic electrolytes to produce a uniform layer, typically ~20-120 μm in thickness, at a growth rate of ~1 μm per minute. The Keronite process can be applied to aluminium, magnesium, titanium and their alloys.

Only very few articles have appeared on adhesion testing of Keronite[11-15]. They are either based on the direct pull test, in which a tensile test is performed perpendicular to the coating with a clamp glued on the coating surface, or the scratch test. The direct pull tests give a minimal value for the adhesion, since in all cases the glue loosened first before any interface failure was initiated. The results of the scratch tests give a value for the cohesive strength of the coatings and not for the adhesion, and are difficult to interpret.

4.2.4 Other adhesion testing

Some other attempts have been made for the evaluation of the adhesion of thick coatings. The two most relevant methods are described underneath.

Pei [16] prepared samples with a groove filled with a laser clad coating and has cut a tensile test sample of which the thickness is smaller than the filled groove depth in order to have two interfaces laser clad/substrate (fig. 7). In those tests however, the test sample breaks in the substrate material and not in the clad nor interface. This means the tensile strength of the substrate material is smaller than of the clad material and than the interfacial strength.

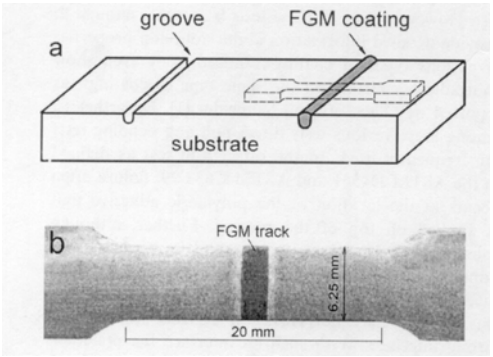

Figure 7: tensile test specimen through one laser clad track [16].

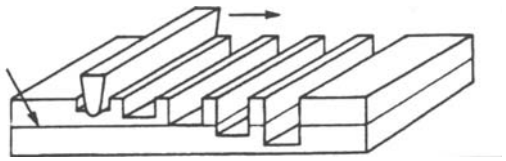

Figure 8: Blickenderfer's test set-up.

The Blickensderfer [17] multi-step shear test (fig. 8) evaluates the shear strength of the different layers as well as the strength of the bond in a single specimen. This technique requires the tedious preparation of a test specimen with a number of machined steps with

increasing depth. Each of the steps is sheared and the results are plotted to show the variation of the shear strength through the thickness. This test requires the construction of a special test fixture and the careful preparation of the test specimen.

4.2.5 Conclusion

The current adhesion test methods are not suited for laser clad coatings or Keronite coatings and do not give quantitative results. There is a clear need for better understanding of the adhesion of such well-adherent thick coatings and for a quantitative test method.

4.3 New adhesion test methods

4.3.1 General

Classically, more work is done on adhesion testing of thin coatings. A lot of adhesion testing methods are developed for thin coatings, but only a few give quantitative results.

The adhesion and damage resistance of coatings on ductile substrates are determined by both geometrical parameters (thickness of the coating, h, relative to that of the substrate) and material parameters (Young moduli, E_f and E_s, residual stresses, σ_r, flaws population – within the coating, $g_t(\sigma)$, and at the interface, $g_d(\sigma)$, resistance of the coating to the propagation of cracks oriented in the direction parallel or perpendicular to the interface, Γ_t, resistance of the interface to the propagation of debonding cracks, Γ_d, yield stress of the substrate, σ_{Ys}) (figure 9).

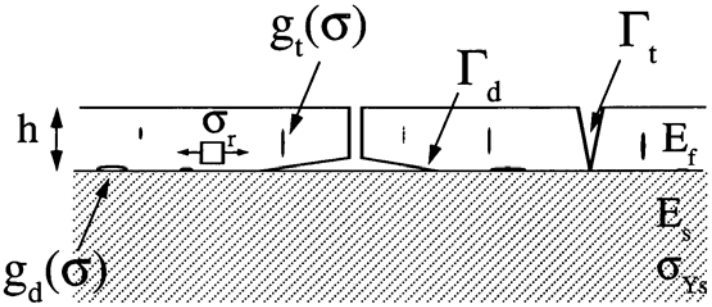

Figure 9: Definition of geometrical and material parameters influencing the adhesion and damage resistance

4.3.2 Controlled straining tests

One technique to characterize the coating/substrate lamina damage resistance is to strain the coating in tension so as to induce the formation of a pattern of cracks. The crack density increases with increasing strain in a manner which is related to the overall parameters of the system as described here above. In practice, empirical tests for assessing damage tolerance of coatings are based on the observation of the crack pattern formed under controlled straining.

4.3.2.1 Tensile tests (TT)

One way of imposing a controlled straining on a coating is by performing a tensile test (see e.g. fig.10). In such a test, the coated sample is subjected to an increasing tensile strain, causing the film to crack and break into segments [18]. The crack initiation and further cracking and/or crack spacing can be observed optically or by acoustical emission [19, 20]. Quantitative values of interfacial properties can be obtained by using appropriate models (see e.g. [21]). The current semi-empirical models are based on an estimate of the maximum interfacial shear strength from the film thickness. Their implementation however gives values which can differ by a factor 3! There is a clear need of more robust modelling and optimising of the method.

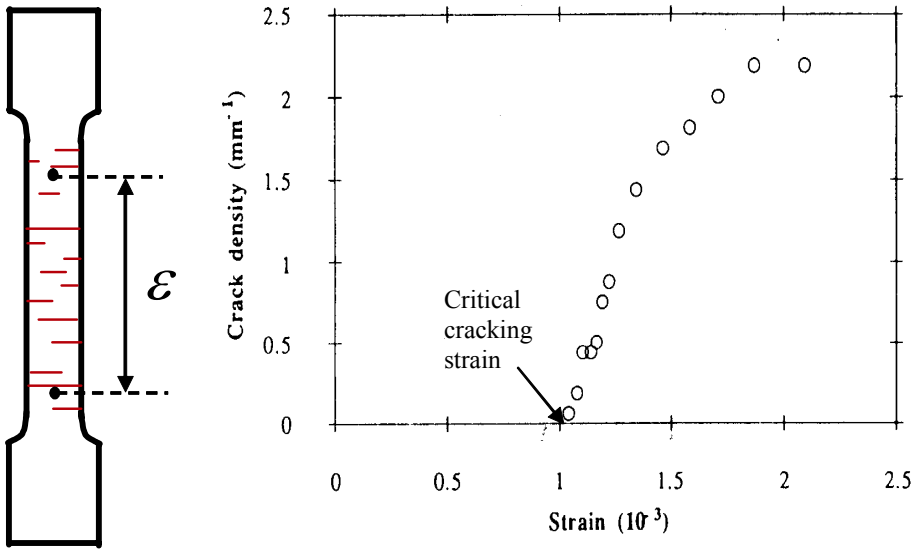

Figure 10: Controlled straining in a tensile test.

4.3.2.2 Four point bending tests (4PB)

Four-point bending testing of coated substrates is an interesting alternative to the tensile test [22]. Strain of the coating is well defined in the four point bending, but for the calculation of the stress, the coating Young's modulus is needed which has to be measured separately. Knowledge of the internal stress state is of major importance in order to obtain reliable adhesion values.

Some authors report tests with precrack in the coating or at the interface between the coating and the substrate (fig. 11). The test method with precrack at the interface makes use of fracture mechanics and the energy release during crack growth is measured [23, 24]. In a previous Federal Science Policy Office project, Ye and Delplancke [25] have used the method on Zn coatings. Chung [26] also used a strain energy release measured on transparent porcelain by cyclic 4PB.

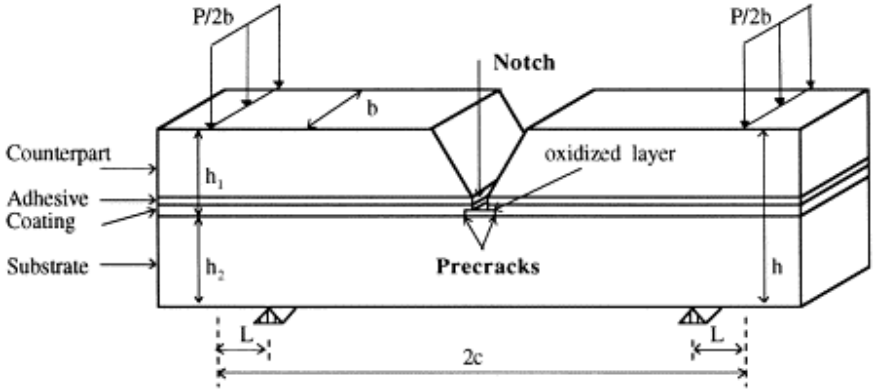

Figure 11: Four point bending test set-up with precrack at the interface.

Katipelli [1] simply produces a notch by a diamond saw perpendicular to the coating in order to create a crack origin near the substrate/coating interface.

The observation of the crack formation during the controlled straining tests can be done by several means. Kucuk [27], Lin[19] make use of acoustical emission (AE) to detect cracks in thermally sprayed test specimen. Ollendorf [28] combined 4PB with AE on TiN coatings loaded in compression and has compared this method with other adhesion testing methods
Richard [29] combined 4PB with AE on WC/Co plasma sprayed on HVOF coatings.

Andritschky [30] uses an optical observation method together with force-displacement curves. The onset of cracking can be seen as a local dip in the force-displacement curve (see fig. 12).

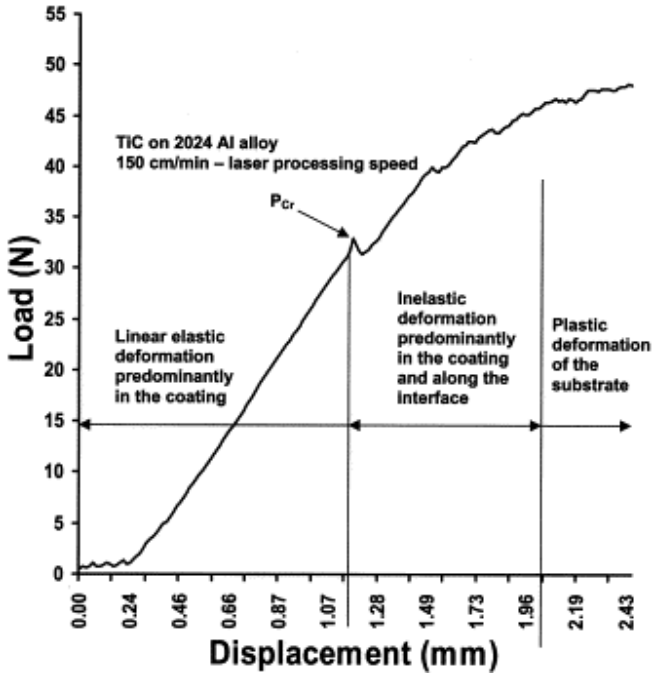

Figure 12: Typical loading curve obtained during the four-point bend test.

Katipelli [1] investigated a TiC laser clad coating on Al6061 substrate (Nd-Yag). He however did not observe the cracking on the surface of the specimen, but at the polished sides of the specimen during and after the test. Erickson [31] and Wiklund [32] describe SEM investigation with in situ 4PB for the cohesion in plasma-sprayed coatings and for TiN and CrN respectively.

4.3.3 Full fragmentation tests

An important study for our project is published by Hjörnhede and Nylund[33]. They have also used a four point bending test on thermally sprayed and laser clad coatings to assess the adhesion. The four point bending is performed on coated tubes (see figure 13), the fragmentation and delamination of the coating is measured in metallographic cross sections and the cracking is monitored by AE. Although no quantitative results of the adhesion are obtained, an interesting comparison is given between different types of thick adherent coatings (see figure 14).

AE is also used [34] for the characterisation of thermal fatigue damage of plasma sprayed coatings. The applied strain in these tests are not induced by a tensile test, but by thermal cycles. Finally, crack density in straining tests on well-adhering britlle coatings is also studied by Hsueh [35]. Contrary to the subject of this project, that article describes how to use the crack spacing for the deduction of an unknown residual stress, based on a master curve of the crack density (per unit coating thickness) versus the applied strain (normalised by the critical initial crack strain).

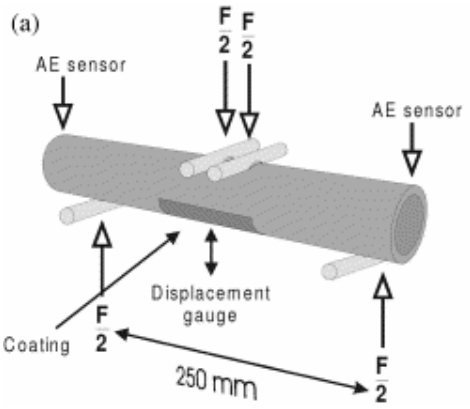

Figure 13: Adhesion testing; experimental set-up for the four point bending and acoustic emission tests used by Hjörnhede[33].

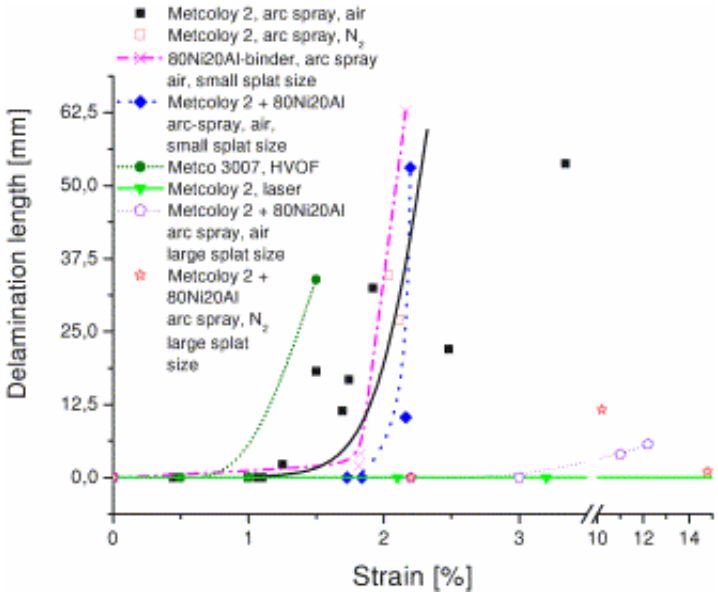

Figure 14: The delamination length as a function of strain for coatings tested by Hjörnhede[33].

4.3.4 Other new adhesion test methods for thin films

New methods are proposed by Kamiya [36, 37]. The interface toughness was measured using so-called “film bricks”, small islands of coating on a substrate, machined using a FIB (focussed ion beam). Such island is loaded under shear by a diamond needle, until it was pushed off. On the other hand, film projections, i.e. free beams of coating material obtained by etching the substrate away, are used for evaluation of film toughness, Young’s modulus and residual strain. The “film brick” method is similar to the Blickensderfer’s method [17] (see figure 8), and it is doubtful the method is very useful for the coatings studied in this project.

Bouzakis [38, 39] proposes a method to evaluate the adhesion under impact loading, by an inclined impact test. Although the method is only developed for thin coatings, it could also be interesting for thick coatings, since they are frequently used for improved impact resistance. It is evident, this method is related to the fatigue behaviour of the interface, and demands time-consuming experiments.

Cross sectional indentation has been used [40] to study the coating fracture toughness of WC-Co thermally sprayed (thick) coatings. The method could possibly be extended to study the interfacial fracture toughness.

4.3.5 Conclusion

Controlled straining tests are mainly explored on thin brittle coatings. There is very few work done on thick coatings such as thermally sprayed coatings. This work is not straightforward in interpreting the results, in other words a lot of work still had to be done to obtain quantitative values for the adhesion. There is also a need to link the observed cracking during a controlled straining test with the microstructural phenomena. Not much is yet known of the physics of adhesion of well-adherent thick coatings such as laser clads

5 SAMPLE PREPARATION – WP1

5.1 Introduction

In view of the objective of the proposed project, a large amount of laser clads have been deposited with different adhesion and different composition. As second well-adherent coating type, the PEO coating or Keronite™ on Aluminium has been chosen, because of its promising applicability for light metals.

5.2 Laser cladding

5.2.1 Materials and parameters

After a short screening of possible laser clad materials, a Ni-WC metal matrix composite laser clad layer had been selected to study further during the project. The layer consists of 45 vol% WC carbides in a Ni-based matrix. Since the focus of the project was on the development of a proper adhesion test and results of different attempts had to be comparable with on another, the composition of the laser clad coatings has been kept constant.

The carbides used in the first series of specimen were angular. The coating thickness was 500 μm. From the second year on however, spherical carbides have been used instead, since to induce less stress concentrations in the coatings and the yield less brittle coatings. Another motive for using spherical carbides was to decrease the (geometrical) complexity of the coating system. The final coating thickness from the second year on was 800 μm.

The coatings have been deposited on stainless steel 304 substrate of different thickness, which surface first has been sand blasted with Al_2O_3. The mechanical properties of the substrate material are given in table 5-1.

The laser beam and cladding parameters have been optimised for this coating-substrate assembly:

- laser power: 3000W
- cladding speed: 1000 and 1500 mm/min
- powder feed: 20 g/min
- 50% overlap

In total, 290 laser clad samples have been produced for WP3 and another 74 for WP5.

Table 5-1: Mechanical properties of the three AISI types of austenitic stainless steel

AISI steel grade	Yield strength $R_{p0,2}$ (MPa)	Yield strength $R_{t1,0}$ (MPa)	Tensile strength R_m (MPa)	Strain at fracture A (%)	Reduction of area Z (%)	Impact toughness K_{CV} (J)	Hardness HB30
304	≥ 190	≥ 225	500-700	≥ 35	60		≤ 215
304L	≥ 180	≥ 215	460-680	≥ 35	60	≥ 100	≤ 215
304LN	≥ 270	≥ 305	550-760	≥ 30	-		≤ 230

5.2.2 Samples

Typical sample geometries used throughout the project are shown in figure 15 and 16 and are tabulated underneath. The general dimensions of the tensile test samples for the straining tests are given in figure 15. Tensile test samples have also been made for testing in situ in a SEM, see figure 16. The ratio between the coating thickness and substrate thickness, shown on figure 16 as h_c/h_{si} , was equal to 0.12, 0.45 and 1.27 for the samples tested.

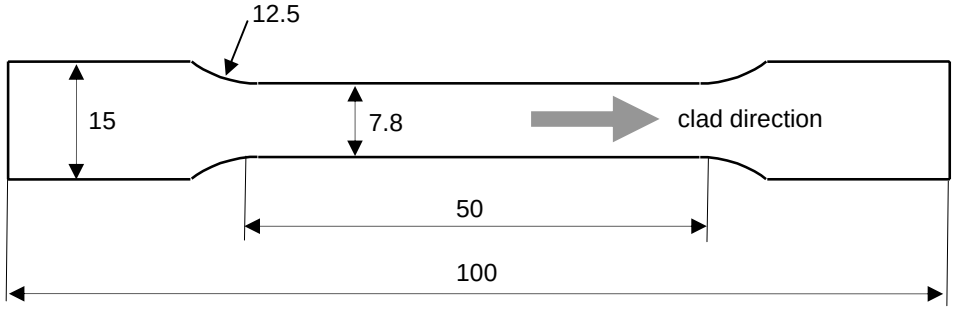

Figure 15: Tensile test sample dimensions.

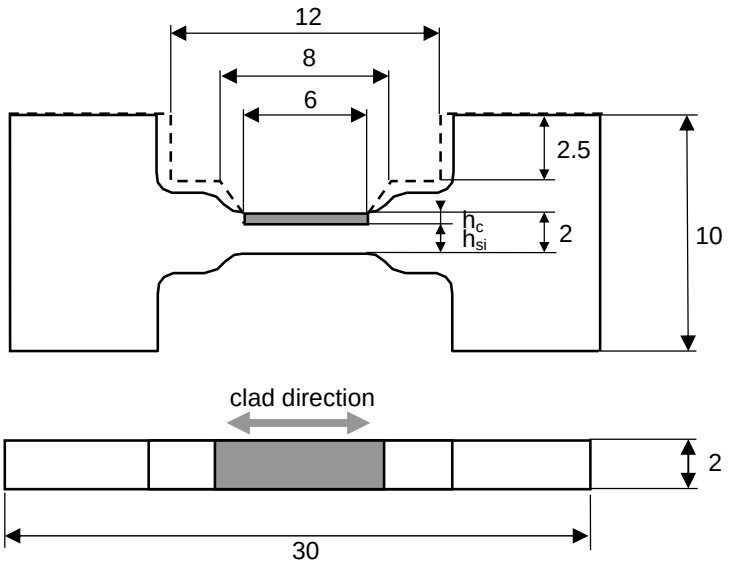

Figure 16: Micro-tensile test sample dimensions.

Table 5-2: Typical sample dimensions used in the project

Test	*dimensions*		
	l	*w*	l_{coated}
4PB test	90	10	70
tensile test (EN10002-1)	100	15	70
micro-tensile test	30	10	6
bending fixed side test	60	100	50
free standing tensile test	100	12.5	100
Characterisation, Internal stress state, wear resistance	40	40	fully clad

Some problems were met during the optimisation of these coatings, mainly due to the distortion of the substrate during the laser surface welding. This causes a problem since the coating has to be ground after deposition in order to allow for the observation of cracking during testing and the sample has to be flat for this machining. Therefore, thicker substrates (10mm) and thicker layers consisting of 2 clad passes have been used for the largest specimen (the tensile test specimen). The substrate has been ground to the desired thickness and the coatings layer to 800 µm total thickness. Other test samples were coated at both sides in order to reduce the distortion. However, this method has been abandoned for the final tests and the round robin.

5.2.3 Adhesion

Several attempts have been made to weaken the interface of laser clads, for comparison in the examined test methods:

Method	cladding speed [mm/min]	powder feed [g/min]	Comments
Polished substrate surface	750 600 500	22.5-26 26 26	good adhesion transversal cracks in coating transversal cracks in coating
Sand blasted substrate surface	750 750 1000 1200	22.5 26 26 26	vertical cracks (i.e. surprising) good adhesion good adhesion good adhesion
Cu layer at interface	750-1000 750-1000	26 22.5	thickness Cu-layer: **1** µm no cracks – probably good adhesion thickness Cu-layer: **2** µm cracks in the region of the layer + bad adhesion

It has been decided to proceed with samples with a 2 μm thick Cu interlayer, since this gave the best results, i.e. the most substantial difference in the adherence of the laser clad coating.

5.3 PEO coatings

A Keronite plasma electrolytic oxidation system was acquired in 2003 for research purposes by the Composites and Coating Group, University of Cambridge. This device has a 25-litre electrolyte bath, with transparent walls for observation, and its power output can varied up to a maximum of 10 kW. It operates at 50 Hz, typically applying anodic potentials of 400 to 600 V, and cathodic potentials of 100 to 200 V, adjusted so as to maintain a constant current of 1 kA m^{-2}.
With this device, improved familiarity with the Keronite process is currently being obtained. Aluminium 6082 samples have been coated with Keronite. The geometry of these samples is 200 mm by 20 mm by 3 mm. A Keronite layer 60 μm thick is produced by placing the specimens in the Keronite plasma electrolytic oxidation system for 60 minutes.

6 CHARACTERISATION – WP2

6.1 Introduction

Both Laser clads and PEO coatings have been thoroughly characterized. The development of a robust adhesion test first requires knowledge of the physical background of adhesion, and the possible influencing parameters. These influence include a.o. the internal stress state, the microstructure, the dilution, the mechanical properties of coating and substrate,…

6.2 Microstructural characterisation

6.2.1 Ni/WC Laser clad

Samples with laser clad layer deposited by VITO on an AISI304 stainless steel substrate as described above were sectioned parallel and perpendicular to the welding direction. The coating surface had been slightly ground at VITO after welding. These sections were ground and polished (not etched) to reveal the morphology of the clad layer and of the interface and to detect possible, local debonding. The deposited coatings have been systematically examined on their porosity, homogeneity and microstructure.

Fig. 17 and 18 show the typical microstructure of the coatings with angular carbides and observed by optical microscopy of respectively for the direction parallel and perpendicular to welding. The length of the small white rectangle at the right bottom corner of each figure is exactly 60 μm. The thickness of the single-layered coating after grinding was about 250 μm.

A typical example of a coating with spherical carbides is shown in figure 19 From that figure it can be concluded the layers have a very low porosity ratio and the homogeneity is very good, although the transition between the laser clad tracks can be discerned by a slight depletion of WC carbides in that region. Another example is given in figure 20, in which a cross section through a micro-tensile test sample is shown. The coating fills well the foreseen gap in the samples.

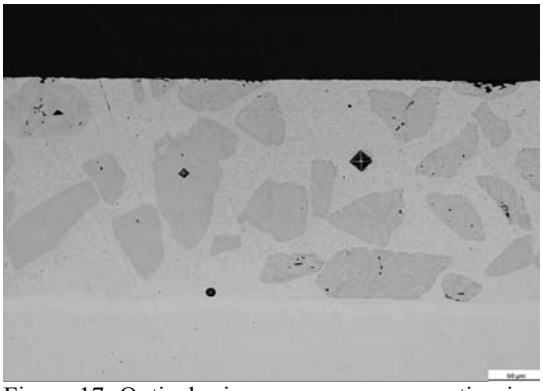

Figure 17: Optical microscopy on cross section in the direction of the cladding.

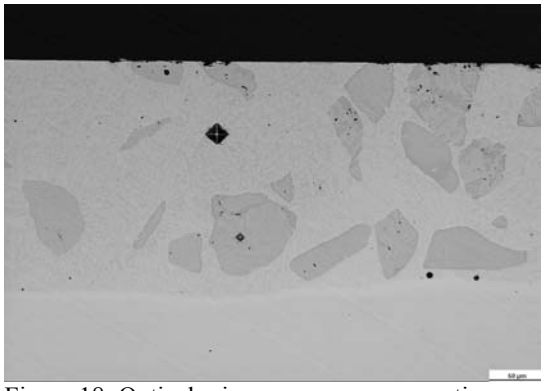

Figure 18: Optical microscopy on cross section transverse to the direction of the cladding.

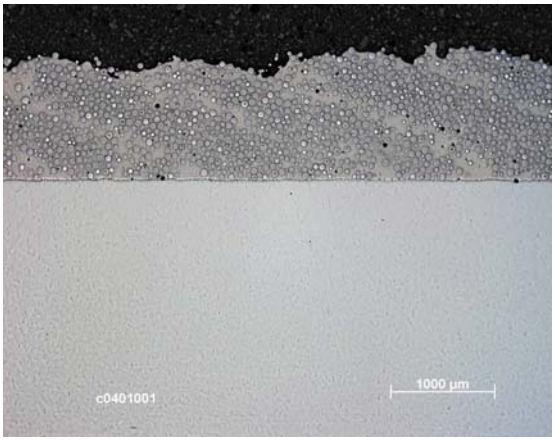

Figure 19: Cross section of as deposited laser clad with sperical WC carbides.

Figure 20: Cross section of laser clad on micro-tensile test specimen.

Figures 17 and 18 illustrate the rather inhomogeneous distribution of the W-carbides in the matrix as the left photograph for instance shows a denser distribution than the right photograph, but the difference most surely is not attributed to the difference in orientation of both sections.

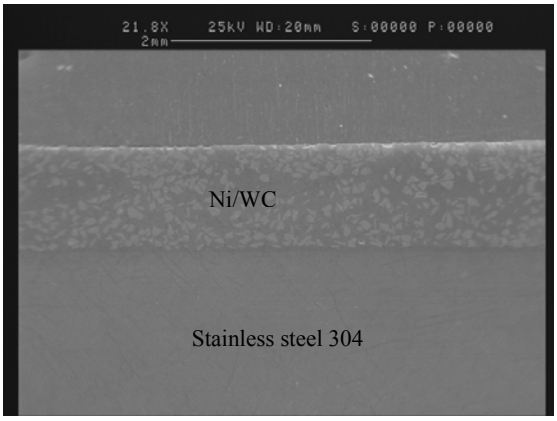

Figure 21: Typical backscattered electrons micrograph of the stainless steel substrate coated with two layers of Ni/WC (45 vol%)

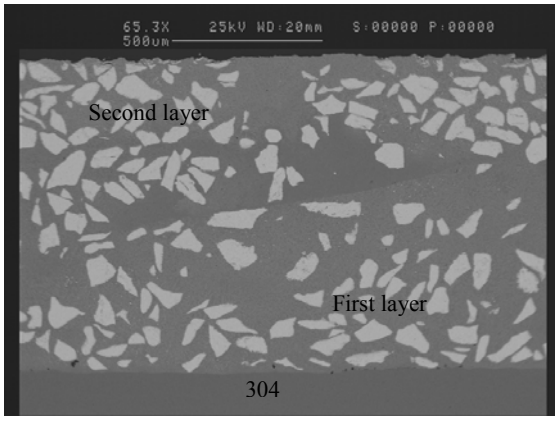

Figure 22: Micrograph showing the two layers of coating.

A cross section of a two layered Ni/WC coating was studied by electron microscopy (SEM). Figure 21 represents a general backscattered SEM view of the structure. A closer view of this coating is shown on figure 22, where one may observe an inhomogeneous distribution of the carbides:

- In the first layer, the carbides are more concentrated at the bottom of the layer near the interface;
- In the second layer, transverse areas of nickel matrix have no carbides.

Figure 22 shows also small porosities at the interface (or nearby) and a difference in the matrix constitution of the two layers (the first one is brighter, i.e. has a bigger fraction of heavy atoms than the second one, and is more homogeneous). An EDX analysis at the interface between the two layers shows that the atomic fraction of tungsten is different in the two matrix (6 at% in the first layer and 1.5 at% in the second one), due to a different level of dilution of carbides in the matrix (figure 23). This figure also shows quite porous carbides (some broken carbides have also been observed).

The dilution of the carbides in the matrix is better observed on figure 24, taken in the second coating layer. The atomic percent of tungsten is given at some locations and it may be seen that the matrix is quite different on both sides of the carbide. It is thought that compounds of the form $Ni_xW_{6-x}C$ are formed inside the eutectic matrix.

The interface between the substrate ant the composite coating is shown on figure 25. Porosity is observed, as well as a thin substrate dilution zone of a few micrometers.

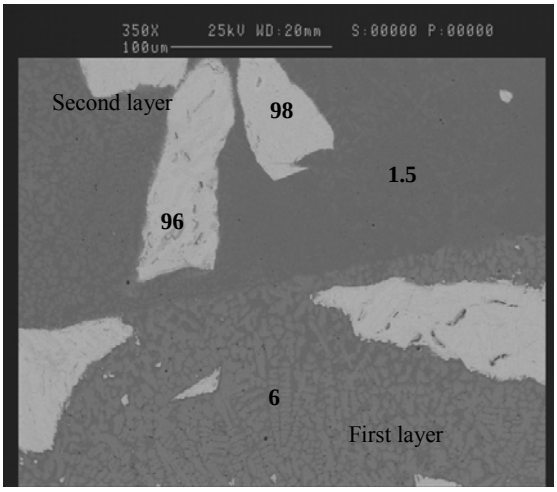

Figure 23: Backscattered electrons micrograph at the interface between the two coating's layers. The atomic percent of Tungsten has been evaluated by EDX.

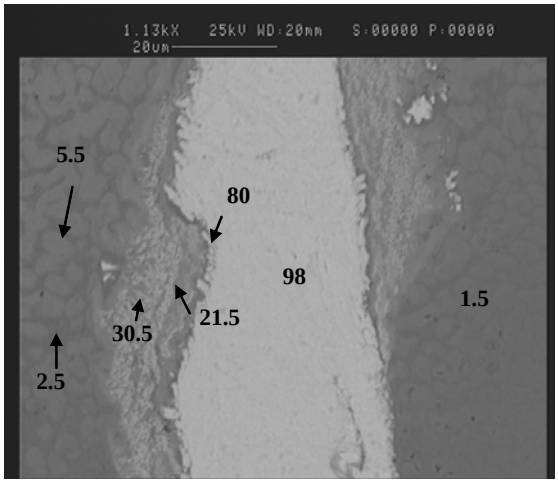

Figure 24: Backscattered electrons micrograph showing the dissolution of Tungsten carbide in the Nickel matrix. Atomic percent of Tungsten is given by EDX.

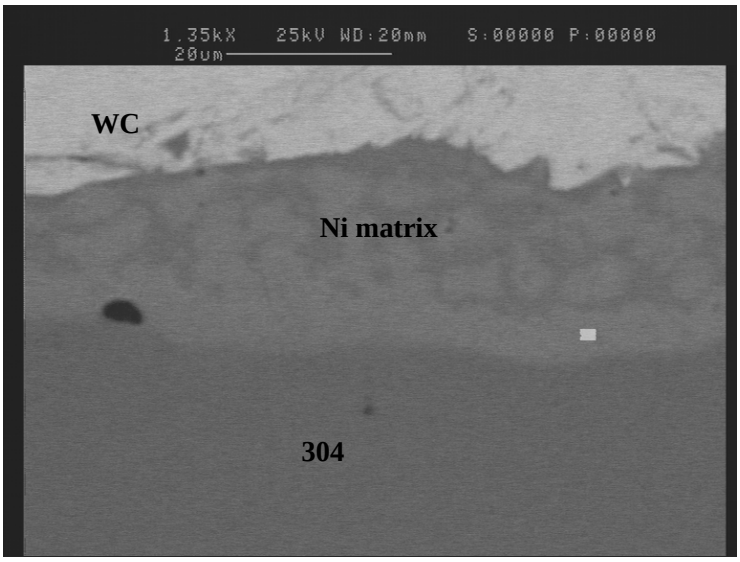

Figure 25: Backscattered electrons micrograph at the interface between substrate and coating. Thin layer of substrate dilution in the matrix with porosity.

6.2.2 PEO coatings

A Keronite coating consists of three layers:
The *External* layer (labelled I in fig. 26) can have a total thickness of 20 μm. It has porosity higher than 15 % and it can be easily polished.
The *Functional* layer (labelled II in fig. 26) can be up to 120 μm thick. It has a very low porosity 2 to 5 % and has very high values of hardness, ~2000 Vickers[41].
The *Transitional* layer (labelled III in fig. 26) is up to 5 μm thick. The interface between the metal and the ceramic upper layer is rough and has deep channels. X-ray diffraction

data indicate that the coating mainly consists of α- and γ-alumina crystallites, together with amorphous material.

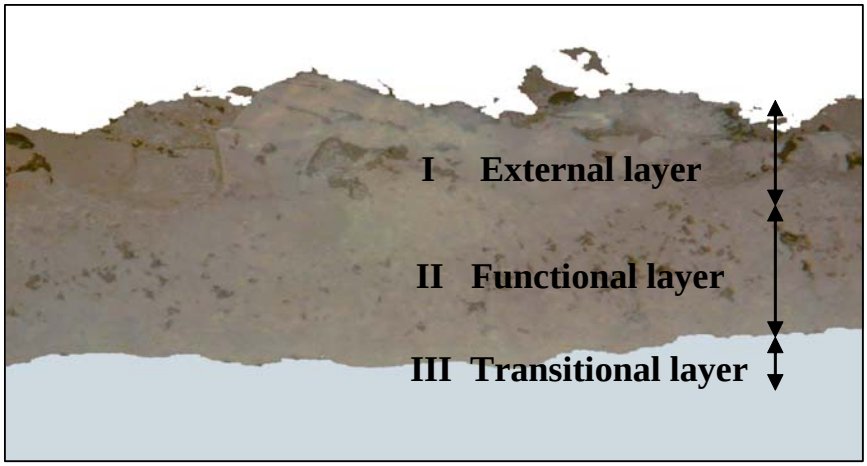

Figure 26: Typical macrostructure of a Keronite coating[42]

Additional characterisation has been performed on PEO coatings by TEM (transmission electron microscopy). SEM and TEM analysis of the interface between the PEO coating and the aluminium substrate, revealed that it is a non porous, sharp and wavy interface. Figure 27 shows TEM microscopy of the interfacial region. Typical grain sizes varied between 0.5 μm and 1 μm. The microstructure of the interfacial region suggests that a high adhesion of the coating to the substrate is to be expected.

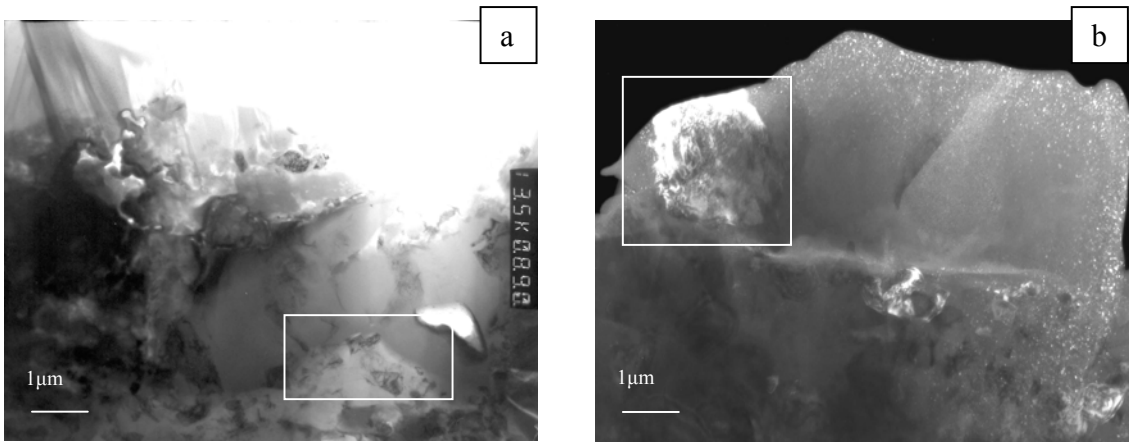

Figure 27: TEM of the interfacial region. In (a), the highlighted area shows the sharp division between the oxide coating and the aluminium substrate. In (b) the highlighted area shows a single grain of the coating.

6.3 Mechanical properties

6.3.1 Hardness

The hardness of the composite material can be measured on a macro-scale with know hardness tests such as Brinell hardness test. The hardness of the constituent phase can however be measured individually, by micro-Vickers or nano-indentation and the overall hardness can then be determined by applying the rule of mixtures.

6.3.1.1 Macro hardness

The macro hardness of the composite coating (see fig. 28) can be measured on the surface on condition the coating thickness is large enough to avoid large influences of the substrate hardness in the measured value. The indenter has to be large enough to cover a representative mixture of both phases.

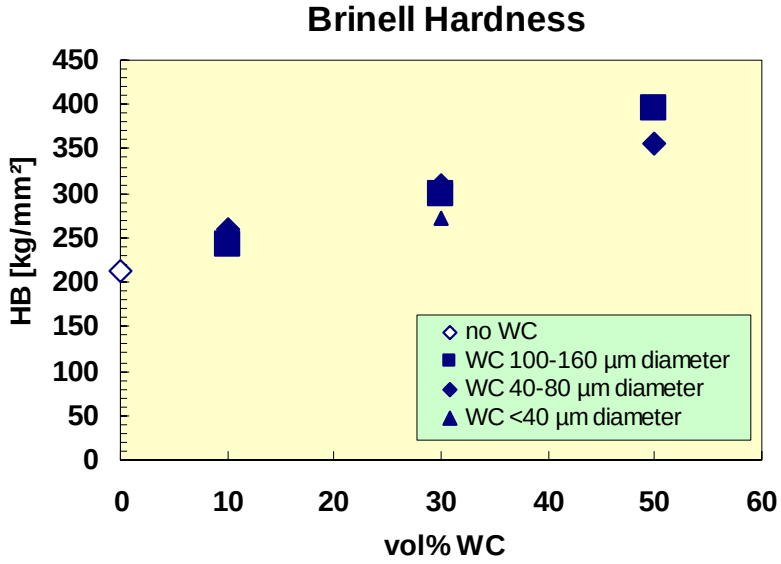

Figure 28: Macro hardness measurement with Brinell on Ni-WC coatings with different WC content.

6.3.1.2 Micro hardness

Hardness HV0,2 and HV1 measurements were performed at the Ni-based matrix and at the tungsten carbides to measure the hardness of each phase and to decide on the most appropriate method to be used within the project.

The hardness of the Ni-based matrix in the clad layer of the parallel section was equal to 490HV0,2 (mean of three individual but equal results) or 465HV1 (mean of 507, 435 and 453). The hardness of the particles contained in the matrix instead was 2170HV0,2 (mean of 2035, 2281 and 2194) or 2113HV1 (mean of 1652, 2365HV1 and 2323).

The hardness of the matrix in the clad layer of the perpendicular section was equal to 474HV0,2 (mean of 509, 441 and 473) or 433HV1 (mean of 309, 482 and 507). The hardness of the carbides now was 2740HV0,2 (mean of 3064, 2686 and 2471) or 2131HV1 (mean of 2640, 2452HV1 and 1301).

6.3.1.3 Nano-indentation

On the scale of the phases of the material, depth sensing indentation or instrumented nano-indentation gives the possibility to determine the hardness of the individual phases [43]. The hardness of the carbides and of the Ni matrix is determined separately, see figure 29 and 30. Nano-indentation experiments can also be used to determine the Young's modulus E out of the hysteresis map (figure 29). The data are corrected for the deviation of the ideal geometry of the diamond indenter and the finite rigidity of the instrument itself.

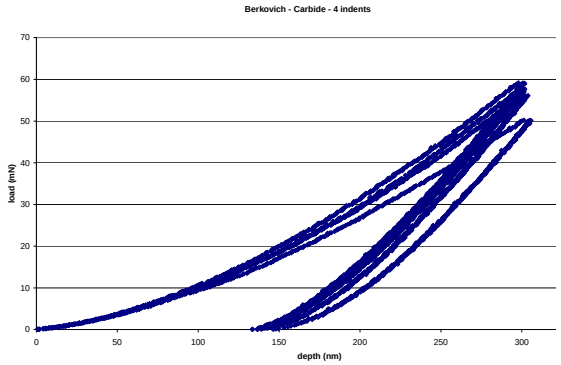

Figure 29: interface indentation with 200 gram load.

	H		Es	
	[GPa]	[GPa]	[GPa]	[GPa]
Matrix	5,2	(0,9)	258	(11)
Matrix2	6,3	(1,2)	260	(16)
Carbide	36,7	(2,3)	576	(1)

Figure 30: interface indentation with 200 gram load.

The hardness of PEO is easier to measure, since it is single phased. Nano-indentation measurements yield an average hardness of 16.1 ± 4.6 GPa. The resulting Young's modulus is 199 ± 65 GPa in plane and 217 ± 45 GPa through thickness.

6.3.2 E-modulus

The E-modulus has to be measured on the coating itself, in order to enable further calculations of cooling stresses and adhesion. This can be realized in several ways: by producing a free-standing film and doing a tensile test on it, by IET on free-standing films or on film-substrate composites, or by nano-indentation. The results obtained by nano-indentation are discussed above.

6.3.2.1 Straining tests on free-standing films

Several attempts have been directed to produce a free-standing Ni/WC carbide film by careful grinding. Chemical etching was not possible since both substrate and coating

contain Ni. Mechanical grinding did not work neither since the coating deformed the thin substrate which was left after initial milling due to internal stresses and the curvature of the sample obstructed further grind/polish. Furthermore, the obtained samples broke while setting up tensile tests due to the brittleness. However, it has been made possible to perform a 4 point bending test on a free-standing film. Therefore, the coating was detached from the substrate by grinding down the substrate using a diamond whetstone. This method produced a flat surface while preventing the coating from cracking. The E-modulus could be derived from this experiment (see figure 34).

6.3.2.2 Impulse Excitation Testing (IET)

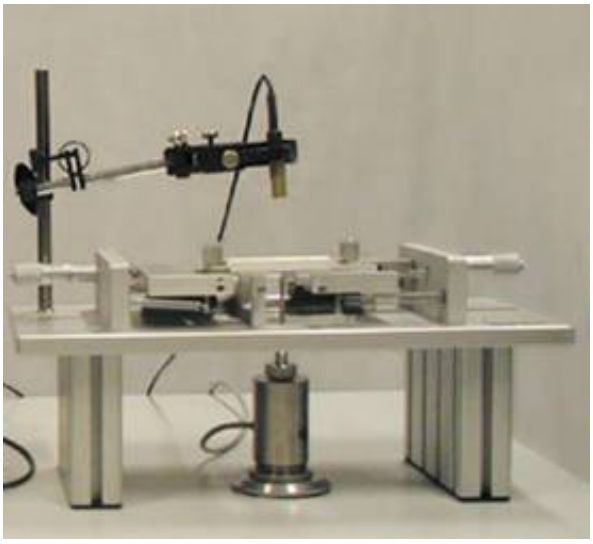

Figure 31: IET equipment and set-up.

The third technique to measure the Young's modulus was the Impulse Excitation Technique (IET). This test is standardized (ASTM E 1876-00, ASTM C 1259-01). With this technique a vibration is introduced in the material by means of a small mechanical impulse. The energy of this impulse is absorbed by the material. The frequency spectrum of this vibration is based on different resonance frequencies and is dependent on, for example, the elastic properties of the material, the geometry, the density and the microscopic and macroscopic structure of the material.

For simple shapes such as rectangular bars, cylindrical rods and discs there are well defined vibration modes. Therefore, IET tests on a free standing Ni/WC clad yield reliable results. Since obtaining a free-standing film requires very time consuming sample preparation, the IET method has also been tried on a coating-substrate assemble, without the desired effectiveness. It seems not to be difficult to separate the coating and substrate moduli properly.

6.3.2.3 Laser Acoustic waves

A new method for the determination of the E-modulus is the laser acoustic measurement (performed at Fraunhofer-institute in Germany). This technique seems to give good results for thin coatings. With this technique a laser (left in figure 33) introduces a surface acoustic wave in the sample which is picked up by a piezoelectric detector further on the sample (right in figure 32).

The detector measures the phase velocity of the surface wave which depends on the mechanical parameters of the sample (for a homogeneous, isotropic material) as follows:

$$c = \frac{0.87 + 1.12\nu}{1+\nu}\sqrt{\frac{E}{2\rho(1+\nu)}} \qquad (6\text{-}1)$$

with:
c = phase velocity
E = Young's modulus
ν = Poisson's ratio
ρ = density

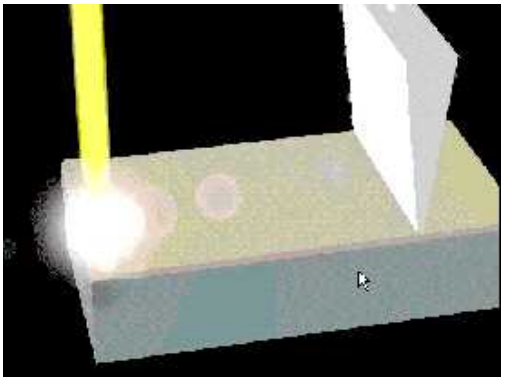

Figure 32: measuring principle (laser acoustic waves).

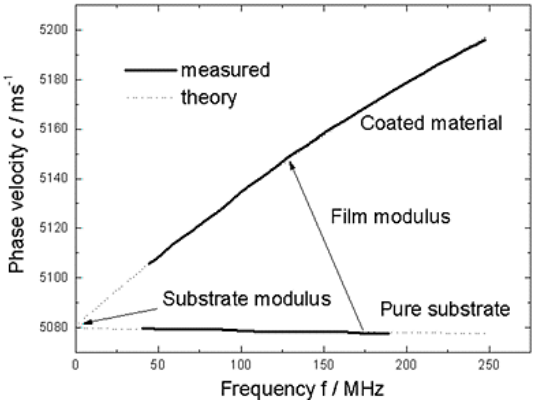

Figure 33: Phase velocity as a function of frequency.

The signal amplitude decays exponentially in the material and the penetration depth decreases with increasing frequency. For low frequencies (deep penetration) the mechanical parameters of the substrate determine the wave velocity, for high frequencies (low penetration) the mechanical parameters of the coating are more dominant as is shown in figure 33. The slope of the curve can be higher or lower depending on the ratio of Young's modulus to density being higher for the coating or the substrate.

An E-modulus of 259,6 +/- 1,5 GPa was measured which is lower than expected and measured with other methods.

6.3.2.4 Conclusion

The overall Young's modulus, needed in a later stage of the project to enable proper modelling, is difficult to measure. The IET method and 4 point bending testing are bound to the preparation of a free standing film. Nano-indentation needs less sample preparation and gives reliable results of the elastic compliancy of the different phases. Models, such as Eshelby, can be used to calculate than the composite modulus. A summary of results is given in figure 34. The calculated moduli make use of literature values of the moduli of matrix and carbide (Ni 207 GPa; WC 677 GPa), while the volume fraction of the specimens was determined using backscattered SEM images of the cross section of laser clad coatings, and image analysis. The volume fraction was found to be wt 41% WC.

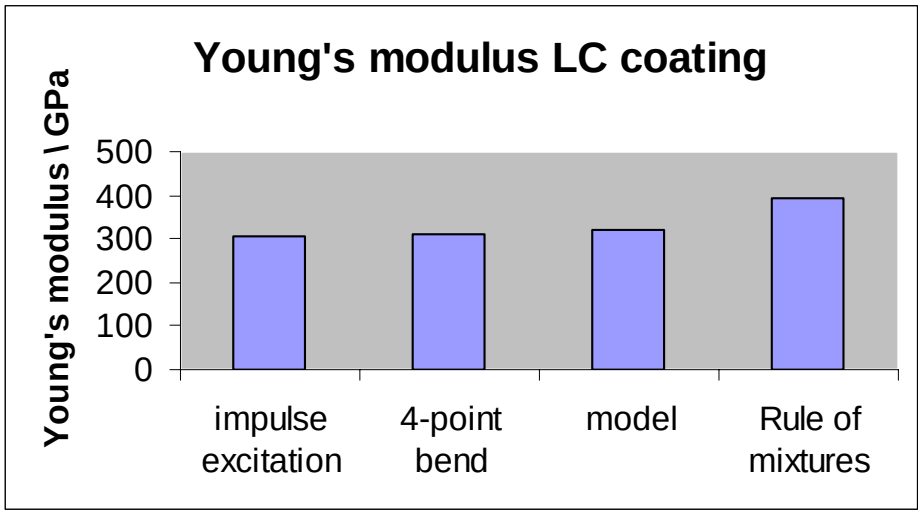

Figure 34. Schematic illustration of the measured and predicted values of the Young's modulus of LC coating..

6.4 Internal stress state

As the critical strain and stress for transverse cracking and the critical thickness ratio for debonding will depend on the internal stress state of the material, this stress state must be known. There are mainly two methods to assess the internal stress state in coatings (and in bulk materials): diffraction methods and mechanical methods. Both methods are tested in this project on the (complex) laser clad coatings: XRD was the diffraction method used and the different mechanical methods were hole drilling and curvature measurements during deposition. A diffraction method gives the stress specific for one phase in the material, while mechanical methods yield the overall macrostress.

6.4.1 XRD method

RX diffraction is well known to measure internal stress state of coatings [44]. X-ray diffraction offers an in situ observation of the elastic strain of the crystal lattice close to the surface of polycrystalline materials. The lattice strain is measured in several directions. The strain tensor, characteristic of the sampled phase, can then be derived. From the strain tensor, the stress state can be calculated with the aid of elastic constants.

As one may see on figure 35, the diffractogram of the deposited Ni/WC coatings was very complex and did not allow to determine the shift of the (331) Ni peak, necessary for the implementation of this method. The resolution of the diffraction peaks could not be improved by etching a surface layer away. In this particular case, the XRD method can unfortunately not be implemented.

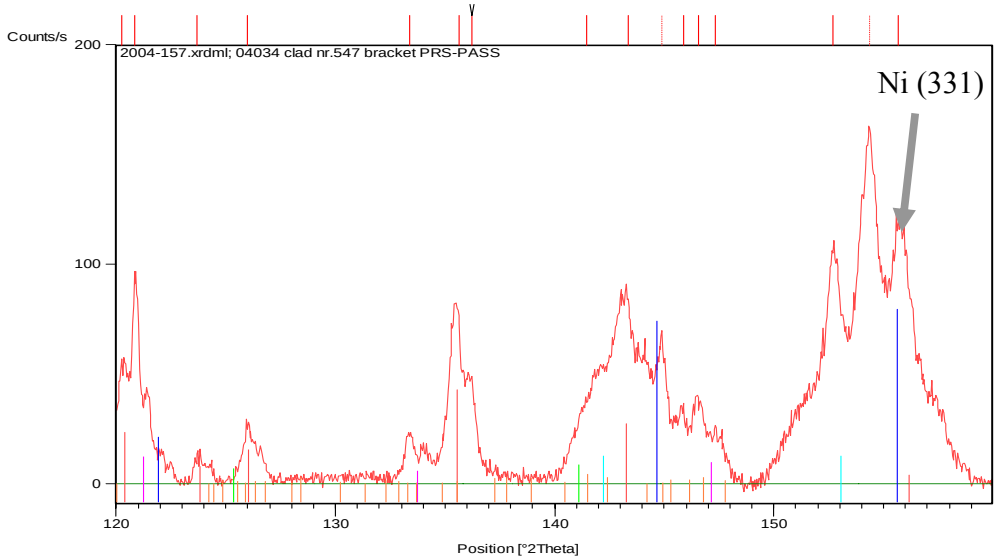

Figure 35. RX diffraction on the Ni/WC coating..

6.4.2 Hole drilling

Hole drilling is a mechanical stress determination method in which the relaxation at the surface is measured during the progressive deepening of a hole by drilling. The relaxation is than correlated with the stress at the tip of the hole.

Several trials were made to drill the necessary holes but due to the presence of the extremely hard carbides this turned out to be impossible. Even diamond drills gripped and overheated in the coating material.

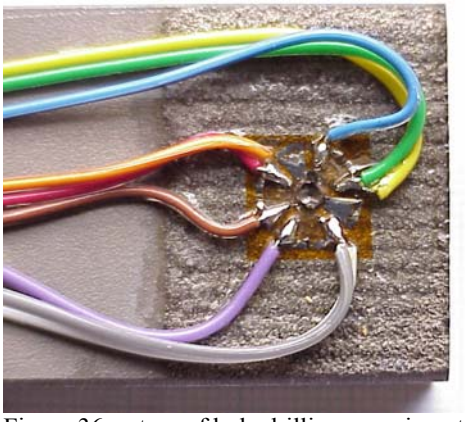

Figure 36: set up of hole drilling experiment.

Figure 37: drill geometry for hole drilling stress measurements.

6.4.3 Curvature during deposition

Several tests have been performed on the measuring of the curvature during deposition of the laser clad. Simple experimental results showing the relationship between deflection after cladding of a beam and the thickness of the substrate is shown in fig. 38. The final goal is to correlate the measured deflection and temperature profiles in function of time with the modelled internal stress state (see paragraph 8.1).

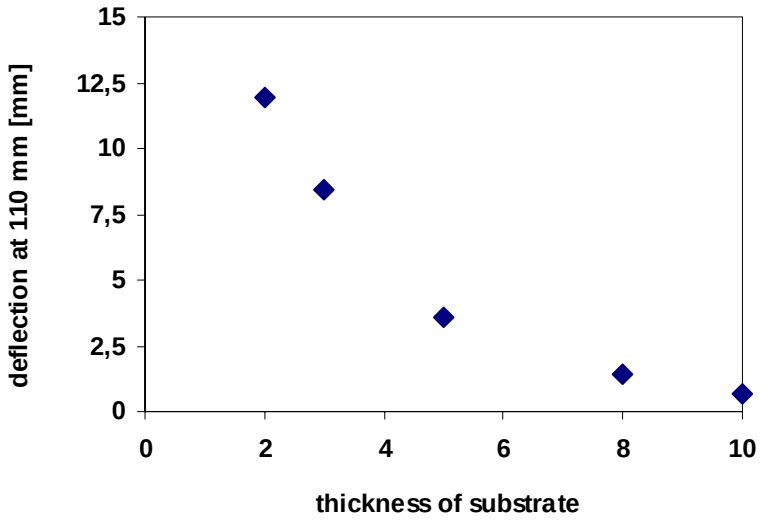

Figure 38. RX diffraction on the Ni/WC coating..

The obtained curvature, in the case of laser clad coated samples, is the combination of the thermal stresses due to thermal gradient through the sample causing a non homogenous plastic yielding and those originating from the differential thermal expansion. This makes simple models such as the Stoney formula cannot be implemented here, but complex modelling taking the plastic properties of the substrate into account had to be developed.

The deflection and temperature inside and at the bottom of test specimen have been monitored during laser cladding. The geometry of the tests samples is shown in figure 39. An area of 110 by 20 mm has been clad. Samples with 5, 8 and 10 mm substrate thickness have been clad, and similar samples have just been heat treated by the laser beam without adding a coating. The fluctuations of the temperature correspond to the transit of the laser beam above the 2 thermocouples. The thermocouples were mounted at 100 mm from the end, one at the bottom of the specimen and a second one in a drilled hole in the middle of the specimen. At the same time, the deflection has been measured by a LVDT. It can be seen that after an initial drop, the specimen bends in the direction of the coating, and relaxes slowly after deposition. These data are indispensable as input for heat flow modelling, with the aim to calculate the internal stress in the final coating.

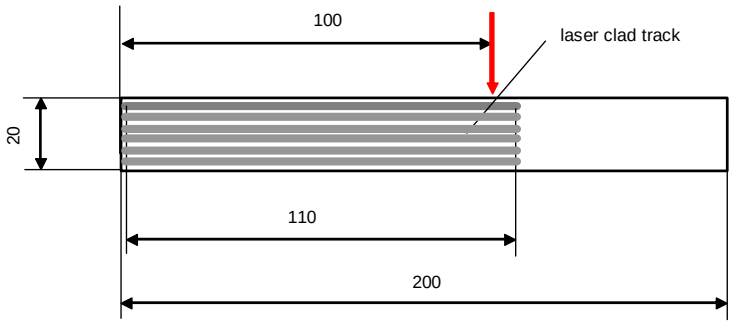

Figure 39: test specimen geometry for the measurement of temperature (red arrow) and deflection (clad end) during cladding

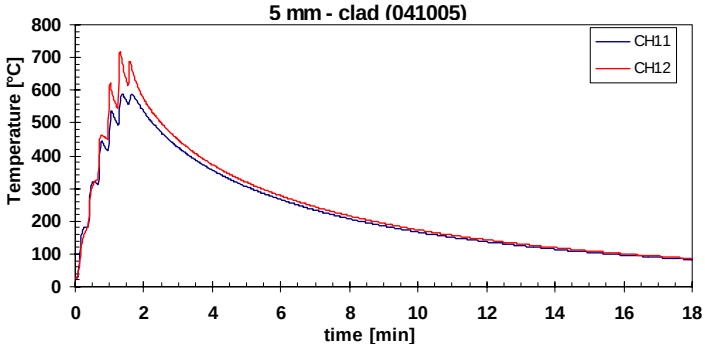

Figure 40: Temperature evolution during cladding of the specimen defined in figure 39, in the middle of the sample (red, CH12) and at the bottom (blue, CH11).

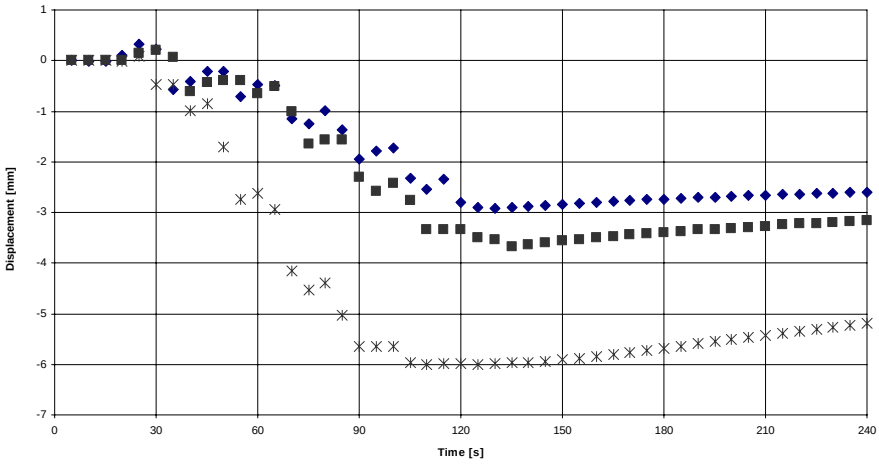

Figure 41: Deflection of the substrate during cladding for a 5, 8 and 10 mm thick coating.

6.5 Conclusion

As conclusion, an overview is given of the methods to characterize the mechanical properties of coatings. All mentioned methods have been evaluated on the laser clad coatings and most of them on the PEO coatings studied in this project. It can be concluded that the multiphase thick coatings, as LC coatings are, are extremely difficult to characterise, contrary to the general feeling that thick coatings are almost bulk materials and that the bulk test methods should apply. The hardness and Young's modulus were determined with success, however, the internal stress should only be estimated by developing complex models for the distortion during the deposition.

		thin coatings [0.5 – 10 µm]	intermediate thickness [10-100 µm]	thick coatings [100-1000 µm]	multiphase
Hardness	macrohardness	-	-	+	±
	microhardness	-	+	+	±
	nanoindentation on surface	+(1)	-	-	-
	nanoindentation on c.s.	+	+	+	+(2)
Young's modulus	tensile/4PB (free standing)	-		+	+
	nano-indentation	+	+	+	-
	Laser acoustic waves	+	+	±	-
	IET (free standing)	-		+	+
Internal stress	XRD	+(3)	+	±	±(4)
	hole drilling	-	-	+	-
	curvature during deposition	+	±	±	±
	curvature after etching	-	±	±	+

(1) dependent on surface roughness
(2) can be used to determine hardness of individual phases
(3) for crystalline films
(4) phase specific stress

7 CONTROLLED STRAINING TESTS – WP3

7.1 Introduction

The heart of the project is the evaluation of controlled straining tests for the adhesion of the laser clad and plasma electrolytic oxidation coatings. It turned out to be more than an evaluation of existing methods. A completely new methodology had to be derived in order to meet the specific behaviour of these thick well-adherent coatings. Basic principles (discussed in §7.2) form the basis of the methodology, but also modelling (chapter 8) is needed to complete the method.

7.2 Theory

The condition for crack extension transversely through a layer is that the strain energy release rate, G, must be at least equal to the total work per unit crack surface area consumed by the physical mechanisms involved in the process of transverse cracking.

$$G_t = -\frac{d(W_e - U)}{dA} \geq \Gamma_t \tag{7-1}$$

For thin brittle coatings on thick substrates, the cracking and debonding of the coating usually appears for elastic straining and the following points have been demonstrated:

- ⇨ Critical cracking stress and strain increase as $h^{-1/2}$ when both the coating and the substrate behave elastically, so a thicker coating will be more sensitive to damage (figure 42).
- ⇨ A coating is more prone to cracking when deposited on a more compliant substrate (figure 43).
- ⇨ If the substrate shows an elastic-purely plastic behaviour, the yielding in the substrate will induce an increase of G, so the lower the yield stress of the substrate, the lower the critical cracking stress of the coating (figure 44).
- ⇨ There is a strain energy release rate related to the debonding of the coating (figure 45). Conditions for cracking/debonding can be found (figure 46).
- ⇨ It has been demonstrated that there is no crack interaction when the distance between cracks is superior or equal to $8h$. When cracks are closer to each other, the effective stress exerted on the flaws is reduced by crack interaction and there is a decrease of the strain energy release rate, G, which will be at its maximum halfway between two cracks (figure 47).

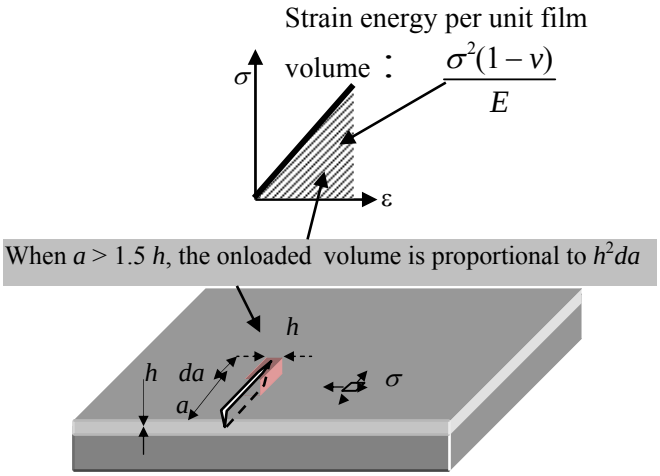

$$dU = 0$$

$$G_t = -\frac{dW_e}{hda} \propto \frac{\sigma^2}{\overline{E}} h = \omega_t \frac{\sigma^2 h}{\overline{E}} = \Gamma_t$$

$$\text{with } \overline{E} = \frac{E}{1-\nu^2}$$

$$\Rightarrow \sigma_c = \frac{1}{\sqrt{\omega_t}} \sqrt{\overline{E}\,\Gamma_t} \frac{1}{\sqrt{h}}$$

$$\Rightarrow \varepsilon_c = \frac{1}{\sqrt{\omega_t}} \sqrt{\frac{\Gamma_t}{\overline{E}}} \frac{1}{\sqrt{h}}$$

Figure 42: Conditions for crack extension in a brittle coating on a ductile substrate with a purely elastic behaviour (ω_t is the dimensionless energy release rate).

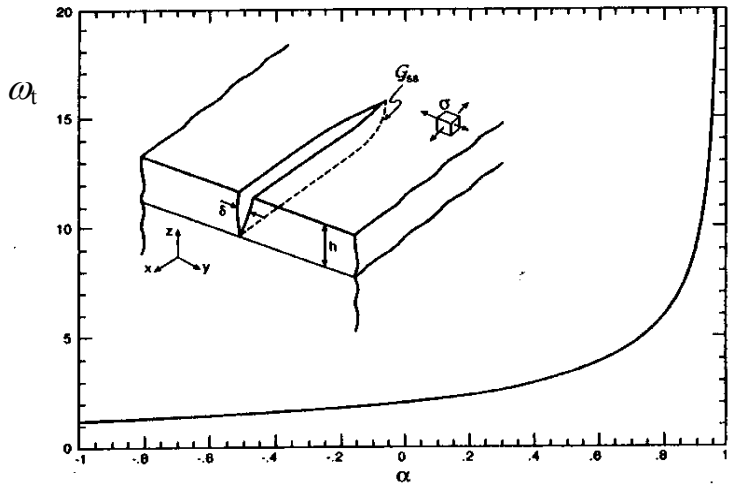

$$\alpha = \frac{\overline{E}_f - \overline{E}_s}{\overline{E}_f + \overline{E}_s}$$

$$G_t = \omega_t \frac{\sigma^2 h}{\overline{E}} = \omega_{t0} \frac{\sigma^2 l}{\overline{E}}$$

$$\text{with} \qquad l = \frac{\omega_t}{\omega_{t0}} h$$

Figure 43: Evolution of the dimensionless strain energy release rate, ω_t, in function of the substrate compliance (elastic behaviour). l is the equivalent layer thickness and ω_{t0} is the strain energy release rate for $\alpha = 0$.

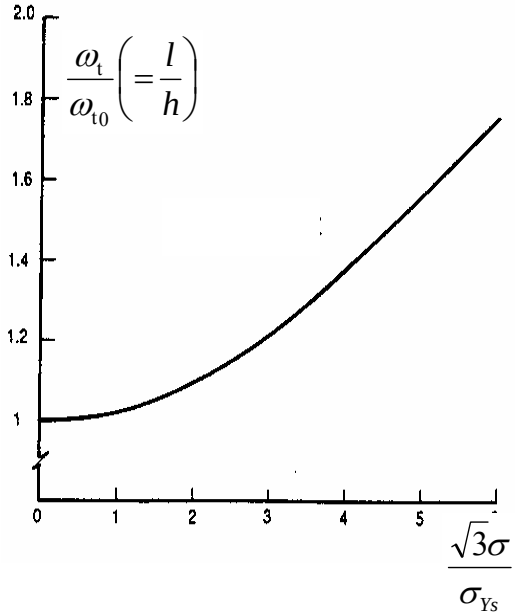

Figure 44: Evolution of the dimensionless strain energy release rate, ω_t, in function of the substrate yield stress (elastic-purely plastic behaviour).

If the coating is thick and not too brittle, after the first transverse coating crack (assumed to happen at elastic strain), the force applied on the substrate may be above yielding. This means that the substrate will deform plastically under the crack. Due to this local straining, debonding may initiate at the tip of the transverse crack and then propagate along the length of the interface. The coated material can then be described as in figure 48: an "equal strain" behaviour is assumed for the part of the sample still bonded, and for the debonded part, the coating is free of charge and the substrate is uniformly plastically strained (i.e. the applied force to propagate the interfacial fracture is constant).

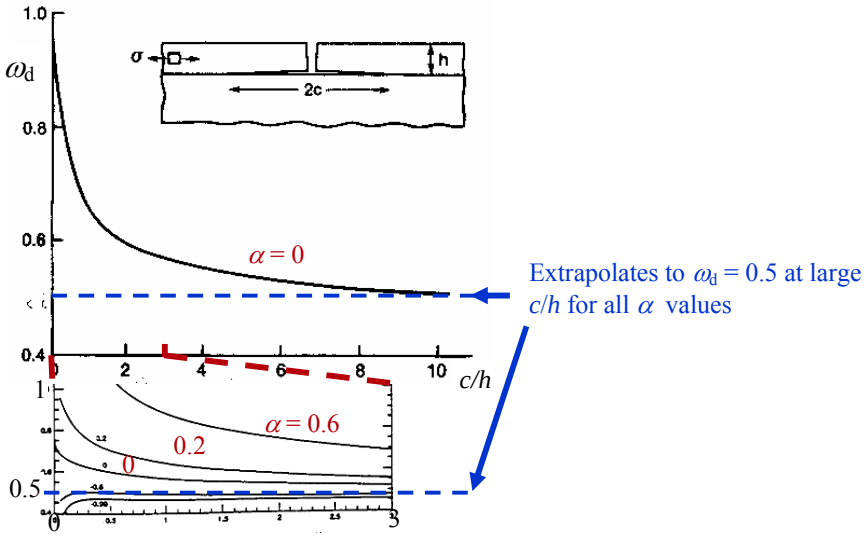

Figure 45: Evolution of the dimensionless strain energy release rate for debonding, ω_d, in function of the interfacial crack extension.

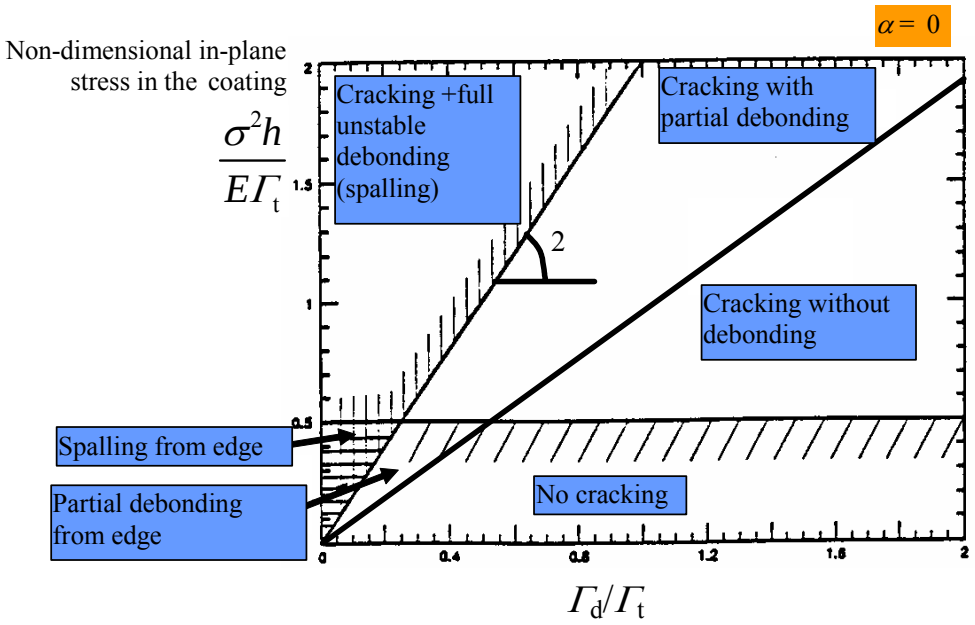

Figure 46: Conditions for cracking with debonding.

Applying the force balance to this system gives:

$$\sigma_{sf}\frac{A_{si}}{\varepsilon_f+1}=\sigma_{si}\frac{E_c}{E_s}A_{si}\frac{h_c}{h_{si}}+\sigma_{si}A_{si} \tag{7-2}$$

where σ is the stress applied on the material, A is the section on which the stress is applied, E is the Young modulus, ε is the strain and h is the thickness of material. The subscripts s, c, i and f are respectively for the substrate, the coating, the initial bonded material and the final debonded material.
One may assume that the energy given to the system through this constant applied tensile strength is mainly transformed to plastic strain of the substrate and debonding of the coating. This entails that the energy needed to propagate a crack at the coating/substrate interface is the sum of the elastic energy relaxed by the debonded coating and the part of the energy given by the applied force not used to strain the substrate. This sum is an upper bound for the fracture toughness of the interface, Γ :

$$\Gamma=\frac{\sigma_c^2}{2E_c}h_c-\frac{\sigma_{sf}^2}{2E_s}h_{si}+h_{si}\int_0^{\sigma_{sf}}\varepsilon d\sigma \tag{7-3}$$

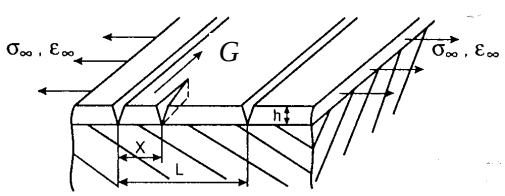

$$\omega_{t0L,x} = 2Bx(1-x)\left(\frac{L}{l}\right)^2$$

In case of substrate yielding, $l = l(\sigma/\sigma_0)$
In case of partial debonding, $L \rightarrow L\text{-}2c$

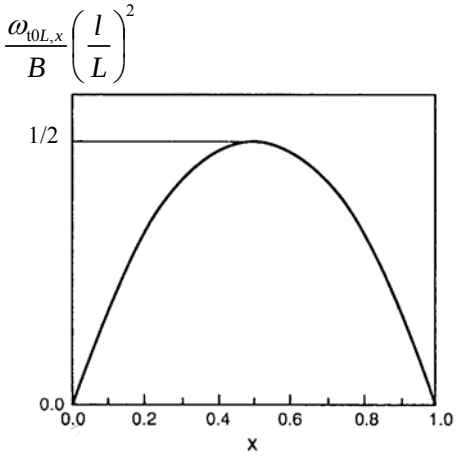

"Effective stress" at each crack tip :

$$\sigma_{eff}(x,L) = \sqrt{\frac{\omega_{t0L,x}}{\omega_{t0}}}\sigma_\infty$$

Figure 47: Dependence of G_t on distance from closest crack.

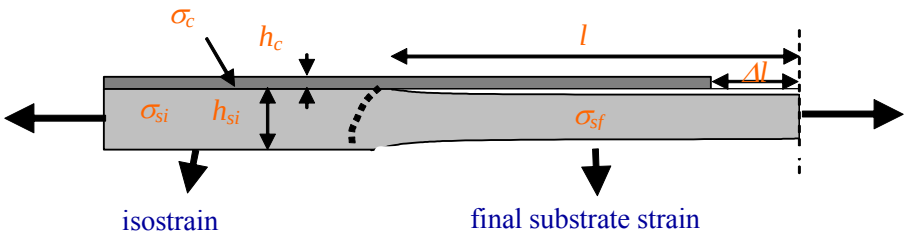

Figure 48: Description of thick coating debonding under constant applied tensile force with strain hardening of the substrate.

7.3 Pure mode I testing

The test principle is shown in figure 49. At a certain moment M a steady crack growth is to be observed. The strain energy release rate is then easily calculated from the formula given in figure 49. However, the crack propagated along the PEO/epoxy glue interface, and not to the desired PEO/Al interface, and a steady state crack growth wasn't observed. No glue is strong enough to make this set up succeed. This straining test is no further use for the coatings considered in this project.

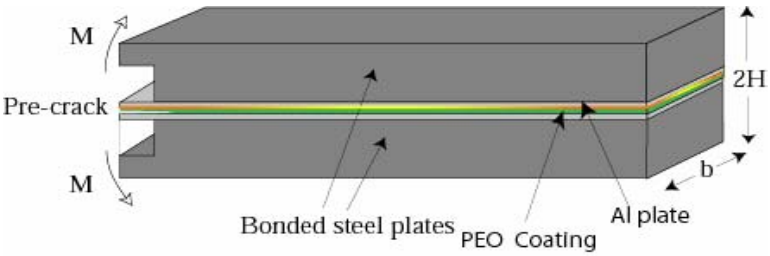

$$G_{ic} = 12(1-\nu^2)\frac{M^2}{Eb^2h^3}$$

Figure 49: Test set up for pure mode I testing on PEO coatings.

7.4 Four point bending without pre-crack

Samples with one WC/Ni clad layer have been tested in a four point bending test set-up. The crosshead displacement rate was 0,2 mm/min for most testing. A typical plot of load against cross head displacement is given in figure 50. The graph shows no discontinuities succeeding the normal elastic behaviour, contrary to the tensile tests. In case of four point bending, a completely smooth plot was recorded for all specimens.

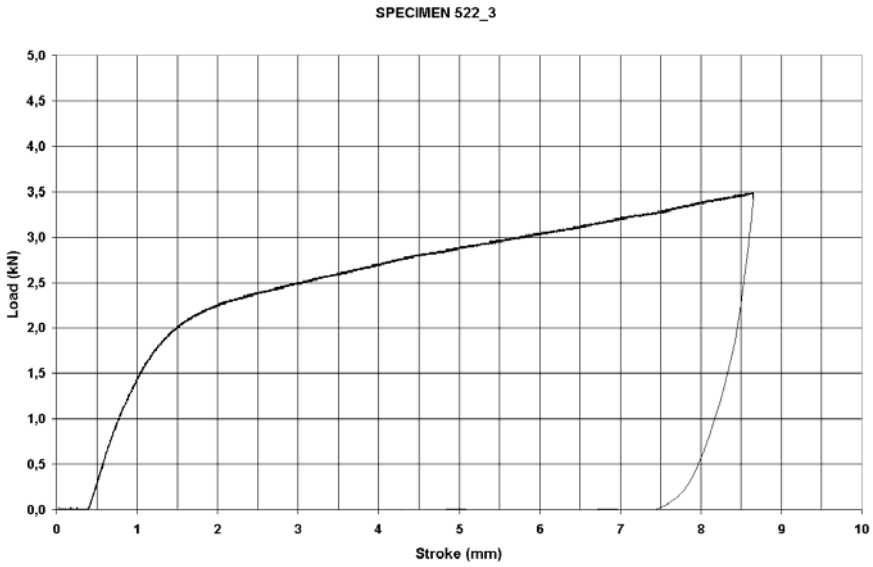

Figure 50: Load versus crosshead displacement of four point bend specimen 522-3

Optically the crack density evolution could be followed by microscopic investigation of the sample surface during testing (figure 51). After testing, cross sections were made thorugh the bend specimen (figure 52). The cracks propagate through the carbides.

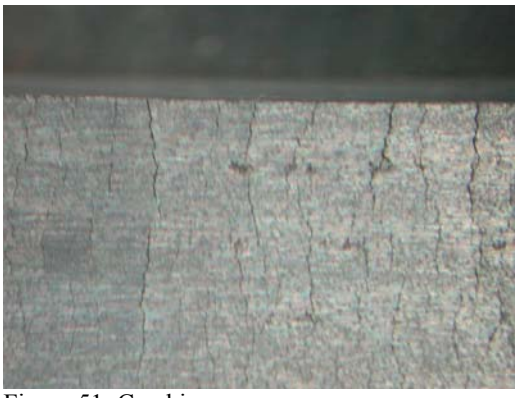

Figure 51: Cracking

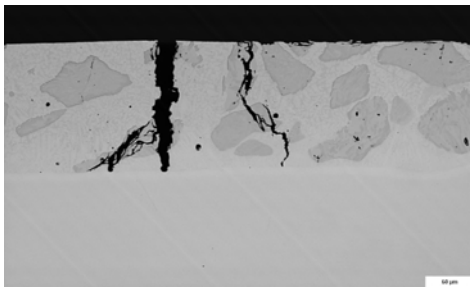

Figure 52: Longitudinal cross sections illustrating cracks present after testing in bend specimen 522-3

An acoustical emission equipment has been installed and coupled with the controlled straining test at Vito. Typical amplitude versus time graphs are shown in figures 53 and

54. The curve of the accumulated events (figure 55) clearly show the onset of cracking and the saturation of cracking after a certain time.

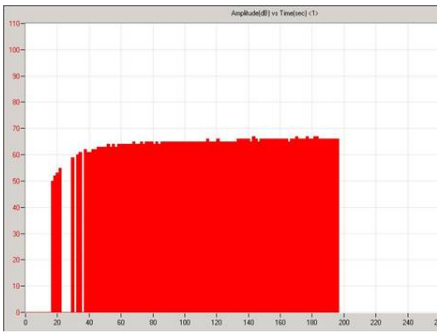

Figure 53 Amplitude versus time curve for uncoated substrate.

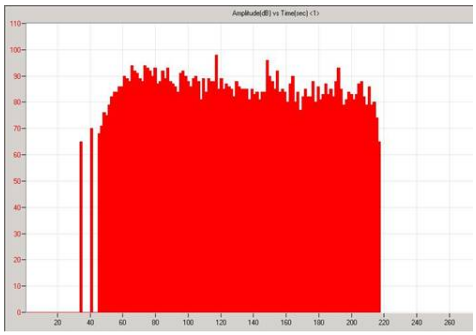

Figure 54:Amplitude versus time for Ni/WC clad sample.

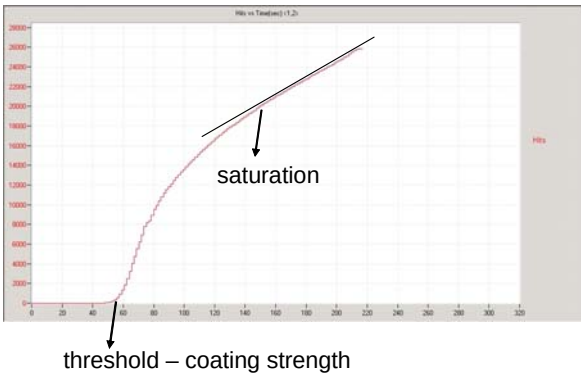

Figure 55: Accumulated events during the four point bending test of clad sample.

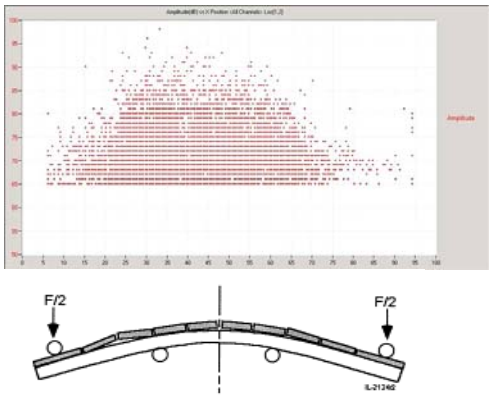

Figure 56: Place of origin of the events.

Additional metallographic examinations on longitudinal sections within the inner span showed that a lot of cracks had initiated during bending, which again were all located at the clad layer perpendicular to the direction of maximum stress and to the outer surface. These cracks were finer than those present in the former tensile specimens but obviously wider cracks were detected in the specimens tested up to higher crosshead displacements. Cracks tended to initiate from carbides present close to the ground outer surface and to propagate through other carbides located towards the substrate. No cracks were observed at the interface parallel with the surface again demonstrating a very good adhesion between the clad and the substrate.

The inhomogeneous strain distribution during a bending test, the plastic deformation of the substrate when the coating cracks and the complicated test set-up clearly hinders this method to be the most appropriate controlled straining test. On the other hand, the method also has some clear advantages: the geometry is very simple and easy to produce and the strain energy release is smaller than in the tensile test.

7.5 Four point bending with pre-crack

Since the Keronite coating is relatively thin, it is difficult to generate sufficient driving force for debonding during the 4-point bend delamination test without a strongly-adhering, relatively stiff over-layer (figure 57). This was produced by vacuum plasma spraying an Al-2%Mg layer of 100 µm thickness. The specimen was then notched using a diamond wire saw. The notch was made as close to the interface as possible and pre-cracks were introduced by using well developed techniques.

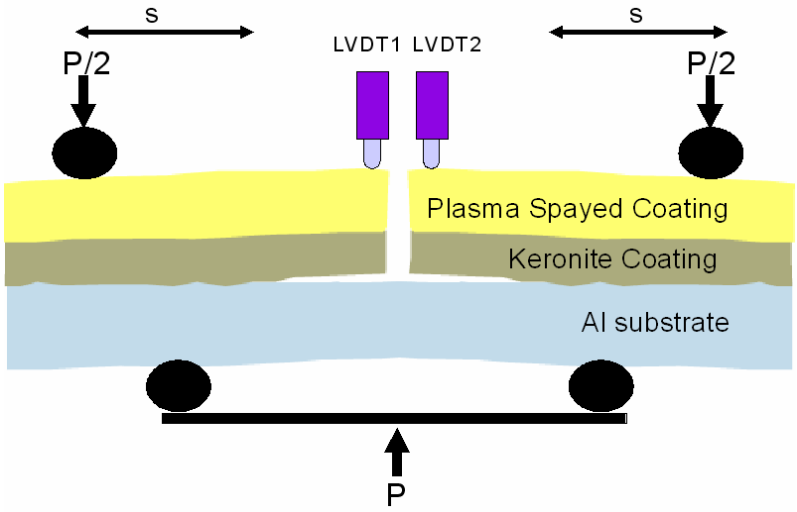

Figure 57 : Four Point Bend Test

The inner and outer spans were chosen to be 17 mm and 24 mm, respectively. When the interface crack propagates between the inner and outer loading points, the energy release rate exhibits a steady state. A data acquisition system (MacLab) interfaced to a Macintosh computer will be used to record the load roller displacement and Linear Variable Displacement Transducer (LVDT) versus time.
The strain energy release rate G_{tot} is given by:

$$G_{tot} = G_p + G_{pr} + G_r \tag{7-4}$$

where G_p is the contribution to the driving force due to application of four point bend load, G_r is the contribution from the residual stress state and G_{pr} accounts for the interaction between the residual and applied loading configuration[45]. Expanding the terms in Equation 1 gives:

$$G_{tot} = \frac{P^2}{4b}\left(\frac{dC}{da}\right) + G_r + \frac{P}{2b}\left(\frac{du_r}{da}\right) \tag{7-5}$$

where P is the applied load, a is the half-crack length , u_r is the displacement of the neutral axis of the beam at the loading roller after unloading is the specimen compliance and b is the width of the specimen.

Statistical treatment of the obtained data from four point bend test of specimens that are not notched and pre-cracked is needed as input for the determination of the Young's modulus of the substrate, and the thermosprayed coating. The Young's modulus of the Keronite layer was found by cantilever bending[41] to be 28 GPa.

It turned out to be necessary to add a strongly adhered stiff upper layer to the specimens (on top of the oxide) to protect the coatings from cracking and to promote debonding between the coating and substrate. Various methods were used, including plasma-spraying of Al, and epoxy gluing of Al plate, but all of them resulted in a new interface and was weaker than the interface of interest. The crack propagated along the new interface between the coating and the new stiff upper layer, rather than along the coating-substrate interface. Even the maximum critical strain energy release rate measured (G_{ic}=150 J m^{-2}) can only therefore be considered as a lower bound for the interface of interest.

7.6 Tensile straining tests

The only test method that yielded good results for testing the adhesion of the laser clad coatings was the newly developed tensile straining tests or the "strain induced delamination" test.

The controlled tensile straining tests have been made on coated stainless steel 304L substrates by laser cladding (Ni/WC(45%)). All the samples for which results are shown hereunder had a layer thickness of about 0.8 mm, but different substrate thicknesses have been tested. In order to reduce the interfacial strength, samples with a layer of Cu at the interface have also been tested.

Typical force-displacement curves for these samples are shown on figure 58. One may observe a transition from multiple cracking behaviour to debonding of the coating when the substrate thickness is reduced. The propagation of debonding is done with a constant force applied on the substrate layer. The substrate is strain-hardened until its plastic deformation reaches a limit giving enough energy to propagate further the interfacial debonding.

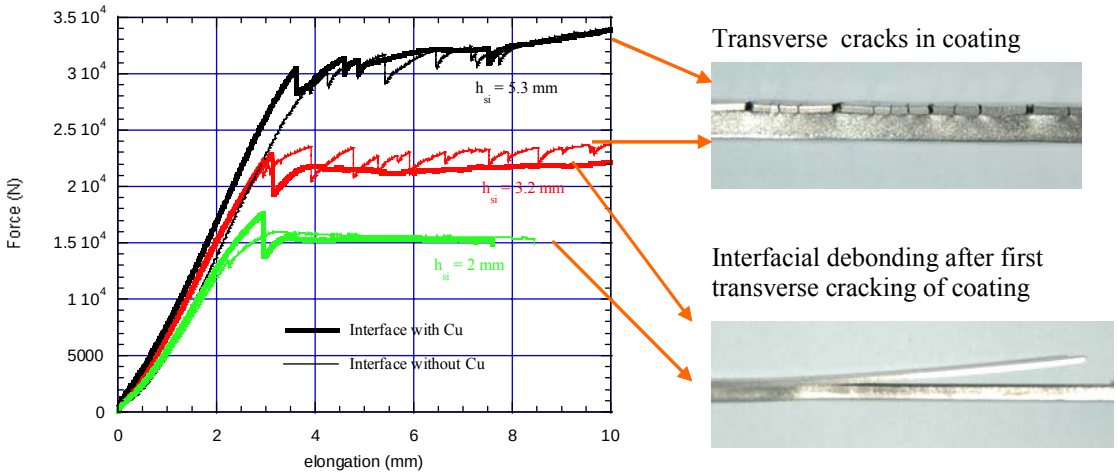

Figure 58 : Typical force-displacement curves obtained on the tensile tested coated samples and their associated damage behaviour.

Some of the tensile tests have also been performed with a CCD camera recording images (1280 x 1024 pixels) of the coated face or of the sample side. A random level of grey was created on that face with either a white paint film and black paint small dots, or white and/or black paint small dots. This procedure enables images taken at different stages during testing to be correlated with a strain mapping software, ARAMIS. The computation of displacement and strain is done by matching facets at different stages. These facets are subdivision of the measured area, in our case they have a side of 7, 9 or 15 pixels. They must be contrasted. The resolution of the measurement was chosen to be of 0.05 pixel, i.e.1.25 µm. The strain map obtained gives the following information:

- mean technical strain for the analysed area (optical extensometer);
- local strain for each facet, enabling the measurement of strain at crack tip and strain gradient through cracks or along them.

These results can be observed on figure 59 where one sees two different damage evolutions during straining: for sample 305, the coating was damaged by multiple transverse cracks, while for sample 338, the damage was a debonding of the coating along the interface after a first transverse crack. The difference in damaging behaviour could be accounted for by the different substrate thicknesses of the samples, i.e. 3.2 mm for the multiple cracks behaviour and 1.2 mm for the debonding one.

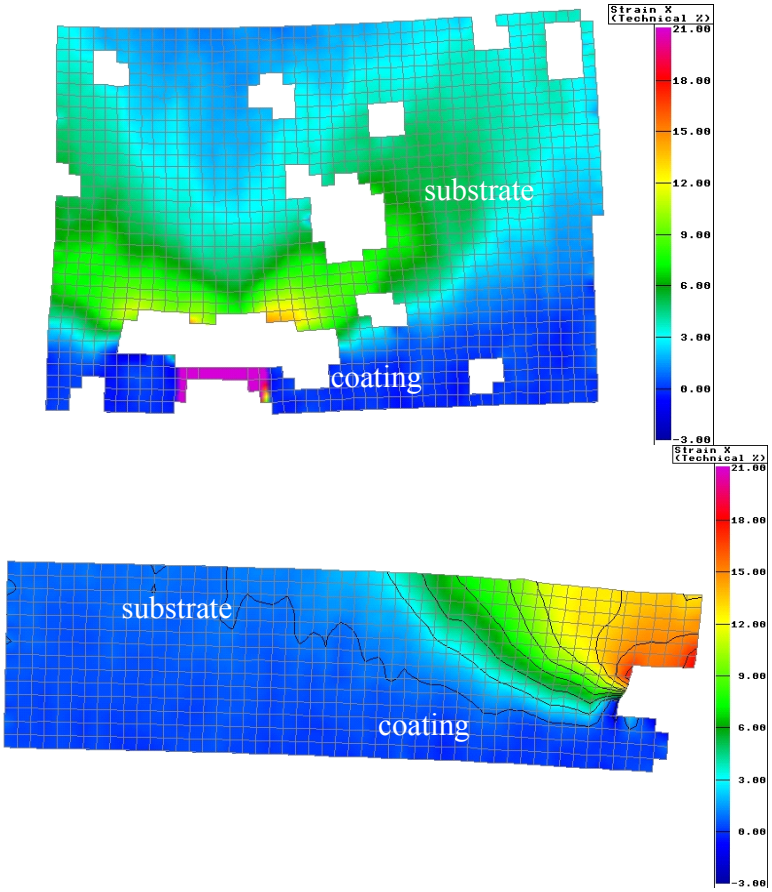

Figure 59: ARAMIS computed local strain in the tensile direction for samples with different initial substrate thicknesses.

In the case of multiple transverse cracking, an analyse of the density of cracks per unit length during straining is shown on figure 60. The density of cracks is higher for the samples without any Cu at the interface, showing a higher interfacial toughness for these samples than for the ones with a Cu interlayer. However, the saturation of the crack density is not reached after a strain of 10%.

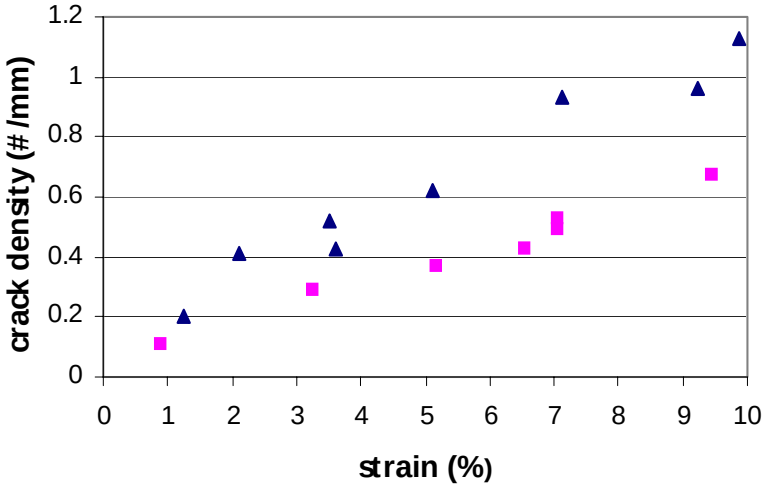

Figure 60 : Evolution of the density of cracks with strain for samples damaged by multicracking.

These full fragmentation tests have been carried out with Acoustical Emission (AE) monitoring. In figures 61 and 62, it is clear that the crack pattern is different in a clad without or with Cu interlayer. In the case of the weaker interface, less cracks appear and the coating delaminates from the substrate interface. The AE shows that the cracking starts earlier in the case of the Cu interlayer, but the number of AE signals raises slower due to the progressive delamination (see figures 63 and 64).

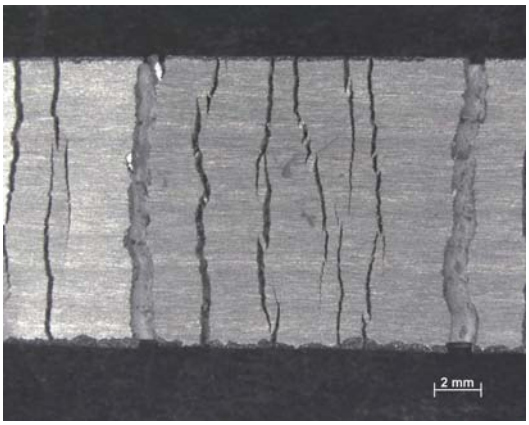

Figure 61: Crack pattern in Ni/WC clad after full fragmentation test. No interlayer has been applied.

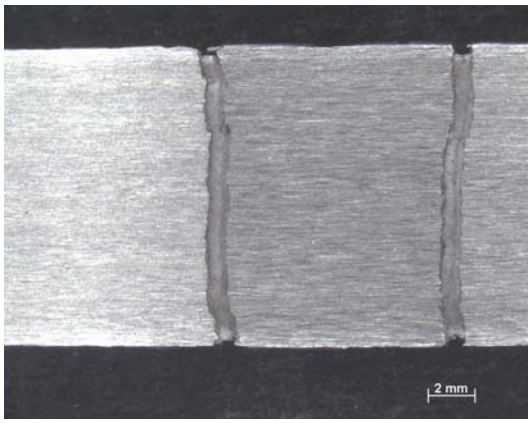

Figure 62: Crack pattern in Ni/WC with 2 µm Cu interlayer after the full fragmentation test.

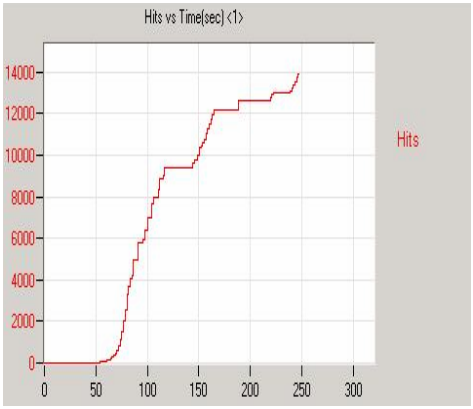

Figure 63: Cumulative AE signal during the full fragmentation test of NiWC clad without interlayer.

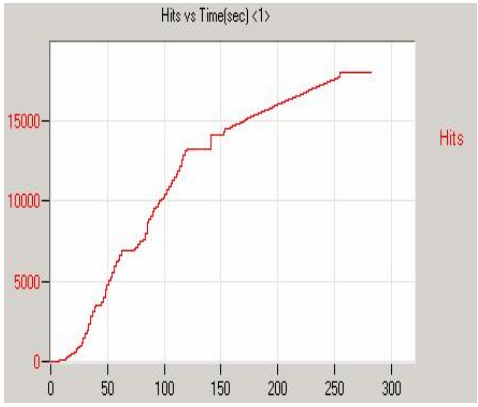

Figure 64: Cumulative AE signal during the full fragmentation test of NiWC clad with Cu interlayer.

Additional full fragmentation tests have been carried out on PEO coatings. During the full fragmentation testing, the coating broke into small fragments with no interfacial debonding. The crack spacing was approximately equal to the thickness of PEO coatings (50-90 µm). The fracture strength of the PEO coating was estimated between 18 MPa and 24 MPa and the interfacial shear strength between 38 MPa and 48 MPa.

In the case of debonding at constant tensile force, the analytical model exposed hereabove (see part 7.1) is applied to the results obtained on the samples with and without

interfacial Cu interlayer. The measured final stress and strain of the debonded substrate are plotted against a typical 304 tensile behaviour (see figure 65).

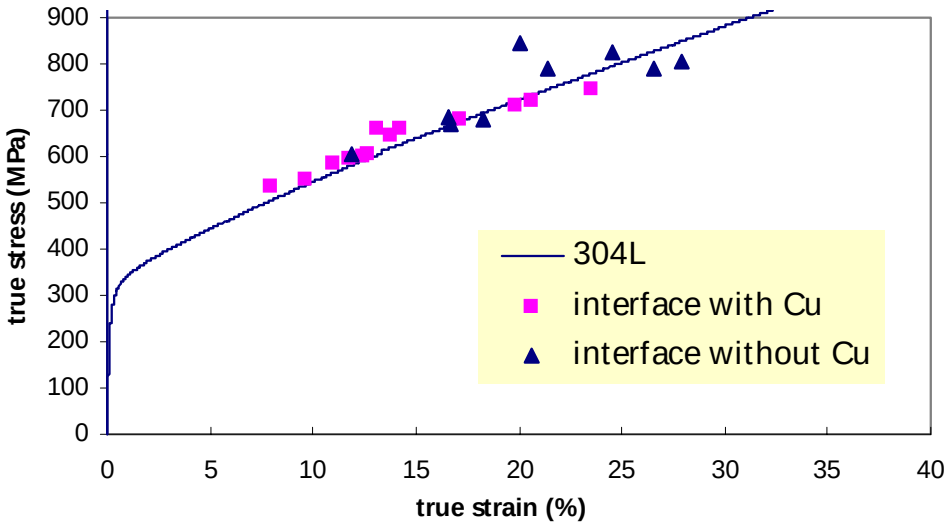

Figure 65 :Measured final stress and strain of the debonded substrate .

The upper bound of the interfacial toughness is then calculated as in the expression here above and plotted in function of the inverse of the substrate thickness. One may observe on figure 66 the lower toughness of the interface containing a Cu interlayer and the quite high toughness of both interfaces studied here. These toughness values may be compared to the toughness of ductile metals where crack extension involves nucleation and growth of voids.

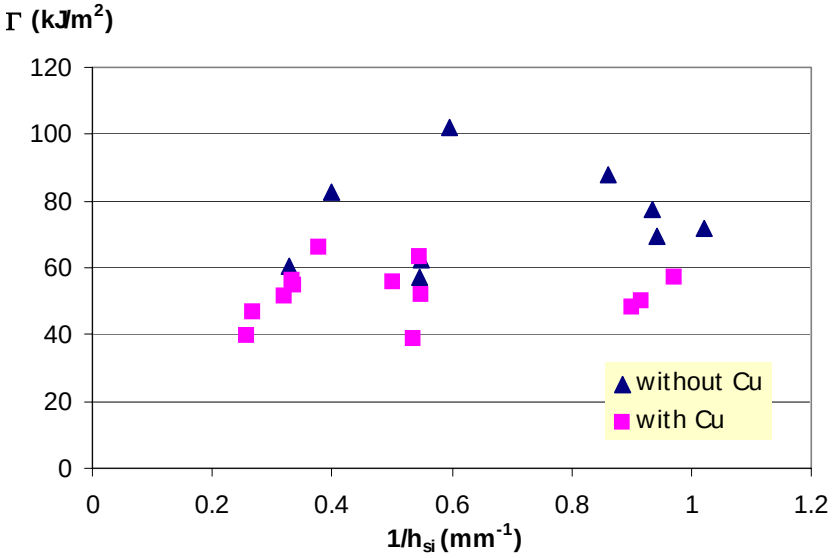

Figure 66 : Upper bound interfacial toughness.

7.7 Micro-tensile testing

Tensile tests have also been done inside a SEM, the samples being observed on their side, so that the interface could be monitored while the tensile test was going on. The sample shape is shown on figure 16, the ratio h_c/h_{si} was equal to 0.12, 0.45 and 1.27 for the 3 samples tested.

The displacement and force were recorded during the test and digital images were taken at different stages. Strain mapping of the substrate was build up with another digital image correlation software, Sifasoft. The results obtained are shown on figures 67, 68 and 69. One may again notice that debonding is more prone to appear at the interface after a first transverse crack when the ratio e_c/e_s is big, as it was observed for the macro-tensile tests.

The damaging behaviour of elasto-plastic coated substrates could be explained by the competition between coating fracture and the debonding due to the energy dissipated by the plastic deformation of the substrate.This means that for a critical thickness ratio, r_c, depending on the physico-mechanical properties of the materials as well as the interfacial properties, the plastic strain in the substrate will be sufficient to propagate the interfacial debonding after a first transverse coating crack (see figure 70).

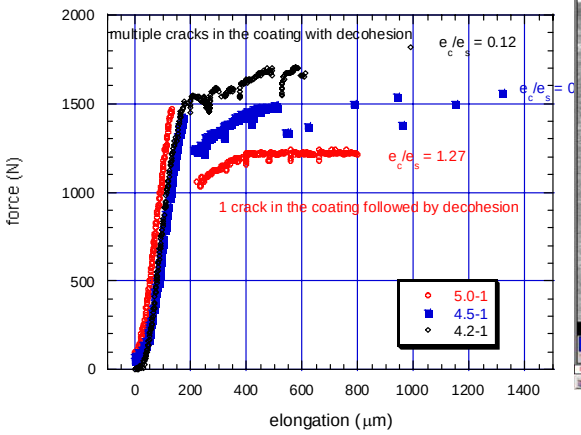

Figure 67: Force-elongation curves for the micro-tensile tests.

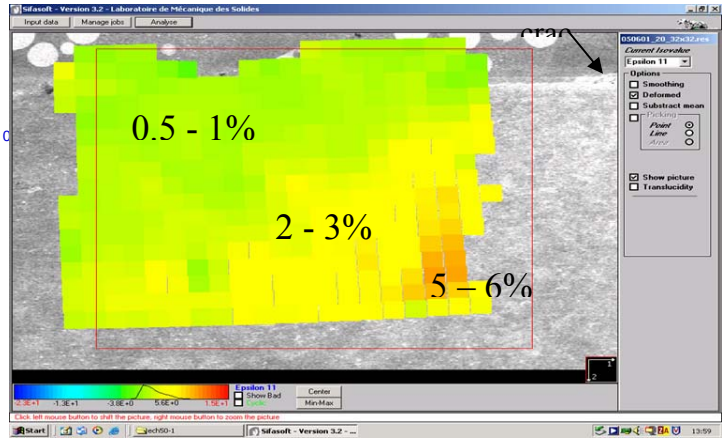

Figure 68: Strain mapping in the direction of straining done with Sifasoft software on sample 5.0-1 in the substrate in front of the interfacial debonding crack.

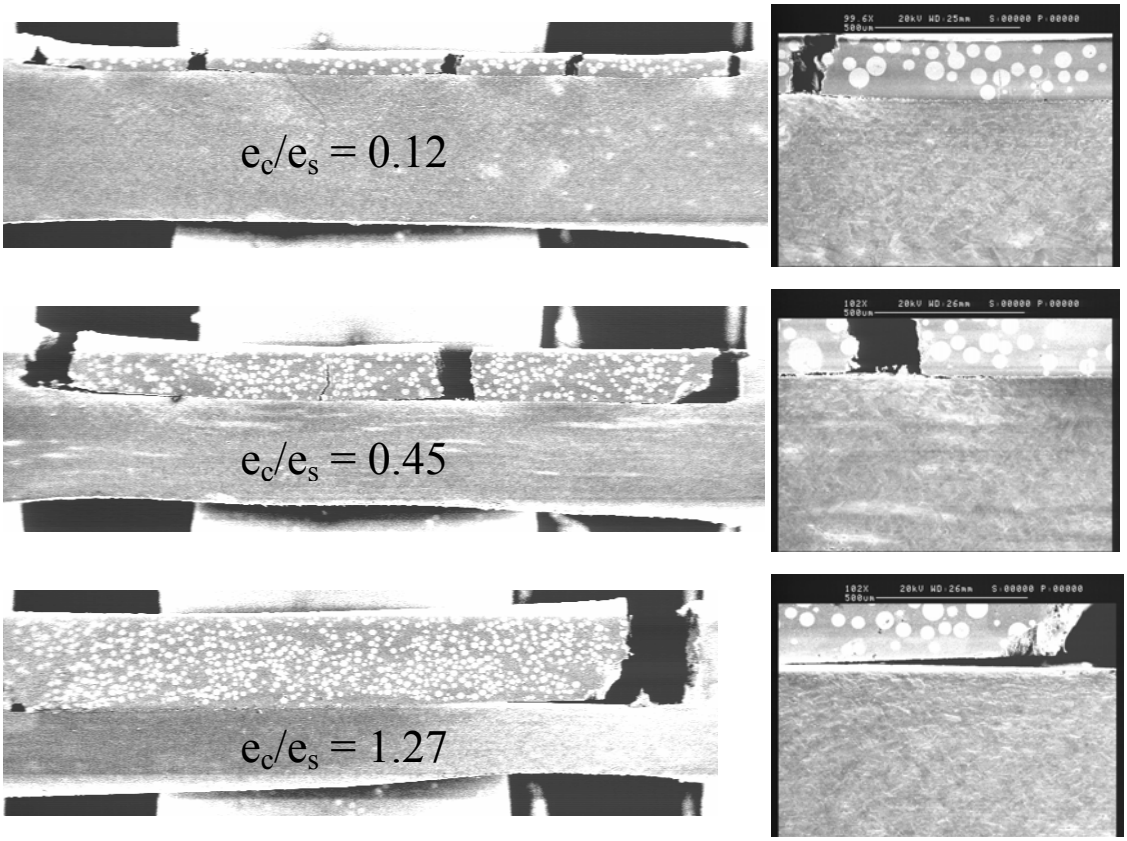

Figure 69. SEM digital images showing the samples after tensile test.

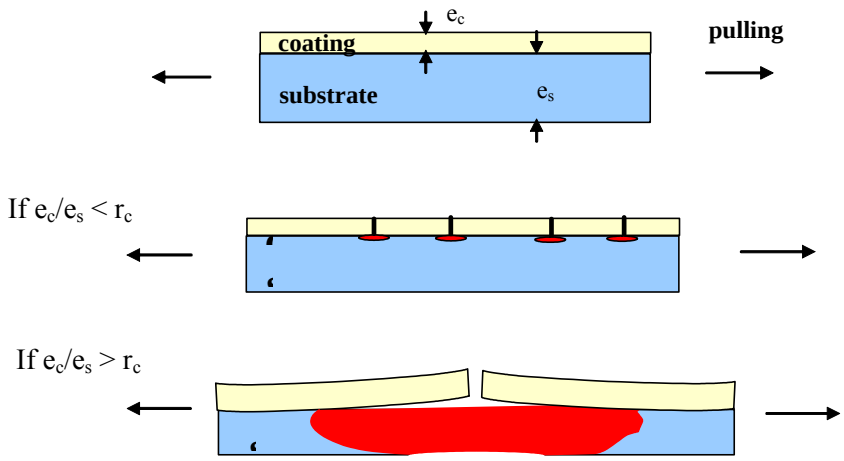

Figure 70. Principle of the local plastic deformation of the substrate generating debonding of the coating.

7.8 Conclusion

Four-point bending testing of coated substrates is the most obvious set up to impose a controlled straining. However, several test set-ups have been explored, with stiff overlayers and with pre-cracks, but none of them was successful in introducing delamination at the interface between the laser clad coating and substrate.

Another way of imposing a controlled straining on a coating is by performing a tensile test. In such a test, the coated sample is subjected to an increasing tensile strain, causing the film to crack and break into segments. The crack initiation and further cracking and/or crack spacing can be observed optically or by acoustical emission. Tensile tests mostly are performed until multiple cracking occurs and the crack density reaches a saturation level. In the case of the studied laser clads, it turned out to be difficult to determine the maximum saturation crack spacing, which is needed to calculate the interfacial shear strength. Moreover, in such method the determined value of the interfacial shear strength is very much dependent on the model used for the stress distribution in the coating between the cracks, and it doesn't take possible delamination at the interface into account. It is not simple to check for delamination after the tensile test. Finally, the thickness and fracture strength of these thick coatings is so high that the steel substrate deforms plastically at the crack tips.

Another approach of the controlled straining test has been developed in this work. The idea is that decreasing the substrate thickness h_{si} with respect to the coating thickness h_c will decrease the number of cracks in the coating and promote the delamination between the coating and substrate. The driving force for the delamination will increase, with decreasing substrate thickness and even a stable interfacial crack growth will be obtained due to the strain hardening of the substrate. Test results are shown in figure 58. Single cracking followed by delamination has been obtained in the laser clad coated samples. The critical ratio h_c/h_{si} could be determined for coatings with and without Cu interlayer, i.e. respectively ± 0.25 and 0.4. The larger the number, the better the interfacial toughness. It is also clear form Figure 58 that a stable debonding occurred at a constant force at and above this critical h_c/h_{si} ratio. In principle, coatings can be compared and ordered on basis of the found critical h_c/h_{si} ratio.

An analytical model has been proposed to calculate the interfacial toughness from the plastic properties of the substrate and the elastic properties of both coating and substrate. This model yields an upper bound of the interfacial toughness. The latter is typically plotted in function of the inverse of the substrate thickness. One may observe on figure 66 the lower toughness of the interface containing a Cu interlayer and the quite high toughness of both interfaces studied here. These toughness values may be compared to the toughness of ductile metals where crack extension involves nucleation and growth of voids.

Further research was however indispensable to determine by FEM modelling the exact interface toughness based on the force needed for the stable delamination.

8 MODELLING – WP4

8.1 Introduction

The test procedure for obtaining stable delamination developed in the previous chapter, needs modelling for deriving the exact interfacial toughness value. The plastic deformation of the substrate is an important factor in this modelling.
The level of internal stresses in the coating is in all traditional adhesion testing an important parameter. Since classical methods for the direct determination of internal stresses are not very successful on the coatings studied here, modelling of the stress development during deposition of the coating and the subsequent cooling to room temperature is indispensable. The results of the calculations are controlled with the deformation of beam specimen in cladding experiments.

8.2 Thermal and stress modelling of laser clad coatings

8.2.1 Experimental Procedures

8.2.1.1 Thermal analysis

Free standing laser clad samples were heated from room temperature to 1200^{o}C at 1^{o}C per minute. Expansion of the coating was measured as a function of temperature on both heating and cooling.
The results for the thermal expansion of a free-standing coating are presented in Figure 71. The dilatometer results suggest that the coating behaves plastically at temperatures above 1000^{o}C. The average measured value of the thermal expansion coefficient for the coating below 1000^{o}C is 11.97 $\times 10^{-6}$ K^{-1}.

The heat capacity of the laser clad coating was measured as 400 Jkg^{-1}K^{-1} over the temperature range of 290 K -500K.

The Thermal conductivity was calculated using the Eshelby method for 300K, 600K and 1000K. The results are presented in Figure 72.

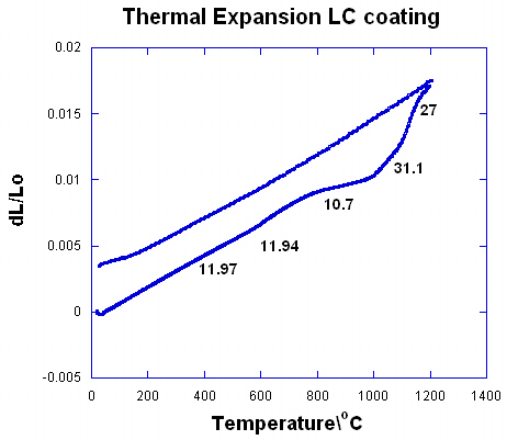

Figure 71. Temperature-expansion curve obtained from dilatometry measurements of LC coatings.

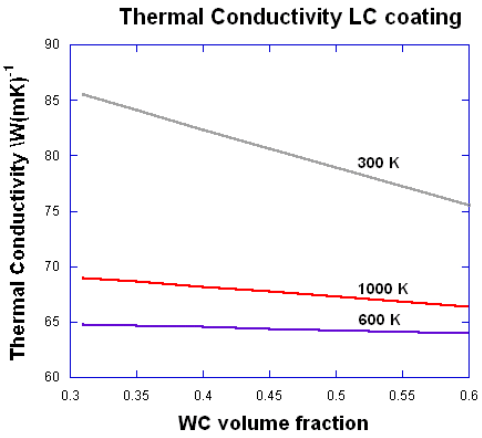

Figure 72. Predicted values for the thermal conductivity of LC coatings at 300K 600K and 1000K.

8.2.1.2 curvature measurements

One end of the substrate, which had dimensions of 170×10×3.8 mm, was bolted to a steel block – see Fig. . 73 and paragraph 6.4.3. The laser beam moved at 12.5 mm sec^{-1}, towards the bolted end. The powder passed through the laser beam and was deposited onto the top-surface of the substrate. The length of the laser-clad track was 110 mm and the thickness of the coating was 1 mm. The thermal history of the substrate was monitored via two thermocouples, which were positioned at the mid-section and on the back surface, 80 mm from the bolted end. Specimen bending was monitored using an LVDT (linear variable differential transducer) to measure the transverse deflection at the free end – see Fig. 73.

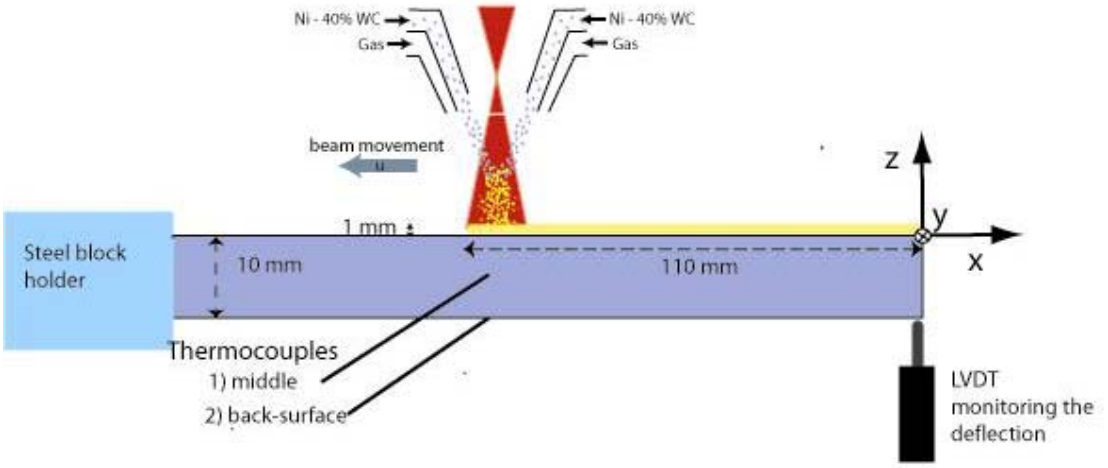

Figure 73. Schematic representation of the set-up during laser cladding.

8.2.2 Model Development

Thermal and mechanical phenomena were decoupled in the analysis. In practice, any coupling between them is expected to be small. Results from the thermal analysis were used to calculate the stress and strain fields, and hence the specimen deflection behaviour, which was compared with experimental data. It was assumed that any inter-penetration of the clad and the substrate, which could arise if there were appreciable substrate melting, was in fact of negligible extent. Microstructural studies revealed that this zone was always less than about 60 μm in thickness, which is of little or no significance in terms of its effect on the thermal field or the associated stresses and strains.

8.2.2.1 Thermal Analysis

The thermal analysis was performed first, using Abaqus 6.5.1. The substrate and the coating were both represented by 8-noded heat transfer elements. The deflection of the substrate at the area of the impingement of the laser beam is not large enough to have a considerable impact on the distance between the laser nozzle and the substrate, therefore the value of the heat flux on the substrate surface is assumed to remain constant. The

intensity distribution of the laser beam exhibited radial symmetry, with Gaussian heat flux distribution, such that the flux at a radial distance r from the axis of the beam is given by

$$Q(r) = \frac{2P_{abs(surface)}}{\pi r_b^2} \exp\left[\frac{-2\left(r - r_0(t)\right)^2}{r_b}\right] \tag{8-1}$$

$$r_{centre}(t) = -vt + x_0 \qquad (x_0 = 0, y_0 = 0, z_0 = 0) \tag{8-2}$$

where r_b is the radius of the laser beam on the surface of the substrate, $\vec{r}$ is a point on the surface the substrate, $\vec{r}_{centre}(t)$ is the position of the beam centre on the surface of the substrate. The position of the beam centre as shown in Eq.8-2 is given as a function of time, t, and as a function of the velocity of the laser beam, v, while x_0, y_0, and z_0 are the initial coordinates of the laser beam. $P_{abs(surface)}$ is the energy that the substrate actually absorbs. The initial energy of the laser beam, P_0, during laser cladding is redistributed according to Eq. 8-3.

$$P_0 = P_{abs(powder)} + P_{abs(surface)} + P_{refl(powder)} + P_{refl(surface)} \tag{8-3}$$

The energy redistribution during laser cladding involves energy that is absorbed by the powder, $P_{abs(powder)}$, the energy absorbed by the substrate $P_{abs(surface)}$, the energy reflected by the powder, $P_{refl(powder)}$, and the energy reflected by the surface of the substrate $P_{refl(surface)}$. The percentage of the power that is absorbed by the substrate was taken as 30% of the initial energy of the laser beam based on published values for the energy redistribution of CO_2 laser beams[46].

An environmental temperature of 25^{o}C was used in the model.
The thermal boundary conditions also include the heat losses from Stefan –Boltzman radiation and convectional air cooling. The value of 25 was used for the convection coefficient and 0.3 for the emissivity.
The addition of the coating was modelled using the element deactivation and reactivation technique [47]. The elements of the coating are initially deactivated and when the beam spot (taken as a circle of radius 0.17 mm from the centre of the beam) passes from a specific point on the surface, the corresponding coating elements are activated. Upon activation, the initial temperature of the coating elements is taken as the melting temperature of Ni. The Ni powder is assumed to be molten and the WC particles remain solid and stay at the molten temperature of Ni. This assumption is confirmed by that the fact that the intermetallic phase of the WC particles was measured to be less than 5%. After the completion of the activation of all the coating elements the external heat flux was switched off and the thermal analysis continues until the system temperature reaches the environmental temperature.

During the thermal analysis, the thermal history of all the substrate and coating was recorded and subsequently used in the stress analysis. Both for the thermal and the stress analysis temperature dependent properties of substrate [48], and the coating, see Table 8-1, were used.

Table.8-1 Properties of Ni-40% WC.

Temperature ^oC	Thermal Conductivity $^{\alpha}$ $W(mK)^{-1}$	Thermal Expansion $^{\beta}$ $Mm(m\,^oC)^{-1}$	**Yield Stress $^{\alpha}$ MPa**
25	65	11.97	199
325	68	11.94	187
725	83	10.7	65

$^{\alpha}$ Calculated values using the Eshelby method
$^{\beta}$ Measured values

8.2.2.2 Stress Analysis

For the stress analysis, the temperatures from the thermal elements were assigned to the corresponding stress elements. The elements used in this part of the analysis are 8-node stress elements and an elastic plastic assumption is adopted.
The stress analysis assumes a perfect mechanical bonding between the substrate and the coating which can be justified by the strong metallurgical bond formed during laser cladding. The elements of the coating in the stress analysis are always activated. This is a good approximation given that the initial temperature of the coating elements is at the melting temperature of the matrix (Ni). Our model assumes that the elements whose temperature is above their melting point are stress free and consequently the tensile strength of the molten coating is almost zero. The temperature history produced from the thermal analysis is used in the stress analysis to calculate the thermal expansion and the plastic strains.
The only boundary condition taken for the stress analysis is that one side of the substrate is rigidly fixed to the steel block, hence the system was treated as a cantilever beam.
Similar to the thermal analysis automatic time increments were used in the model. The deflection history of the free-floating side of the beam is recorded and used for model validation.

8.2.3 Modelling Results

The thermal history recorded with the thermocouples comes in reasonable agreement with the thermal histories that are calculated using our model. The molten pool of the substrate is 0.1 mm deep, almost half of the radius of the laser beam, and is surrounded by a large heat sink resulting in a rapid cooling of the deposited coating.
Figure 74 illustrates that the predicted deflection history is similar to the measured deflection history. During the first 4 seconds of laser cladding, the high temperature of

the top surface of the substrate around the free-floating area of the specimen causes it to expand leading to the bending of the specimen. After 4 seconds, the thermal gradients of the substrate around the free-floating area of the specimen are low and the curvature at the free-floating end is shifted from downward to upward pointing.

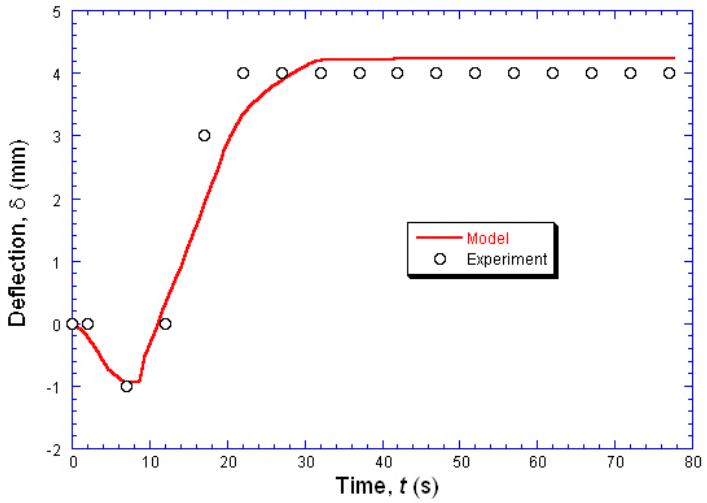

Figure 74: A comparison between the predicted and measured a) temperature histories, b) deflection histories.

Figure 75a is a plot of the through-thickness stresses distribution passing through a point where the molten pool of the substrate has just been solidified. The coating and the top surface of the substrate due to the thermal expansion are in tension. The area along the middle of the substrate is in compression since it is still colder than the upper surface and results in a high thermal expansion mismatch between this area and the area close to the top surface. Another effect of the thermal expansion mismatch is the bending of the sample which puts the back-surface of the sample in tension.
Figure 75b is a plot of the through-thickness stresses distribution passing through a point next to the substrate pool where the substrate has not been heated by the laser beam. The top surface of the substrate is a cold stiff surface next to an almost stress free melting pool. The substrate material that the laser beam has already heated expands resulting in compressive stresses at the top and back surface of the substrate.
Figure 75c illustrates a plot of the final stress field of the system. The coating is fully compressed due to the bending of the substrate.

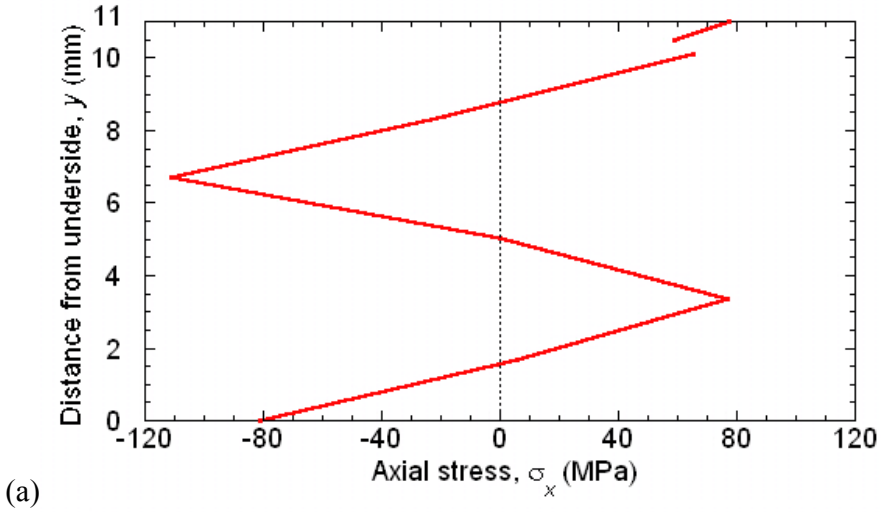

(a)

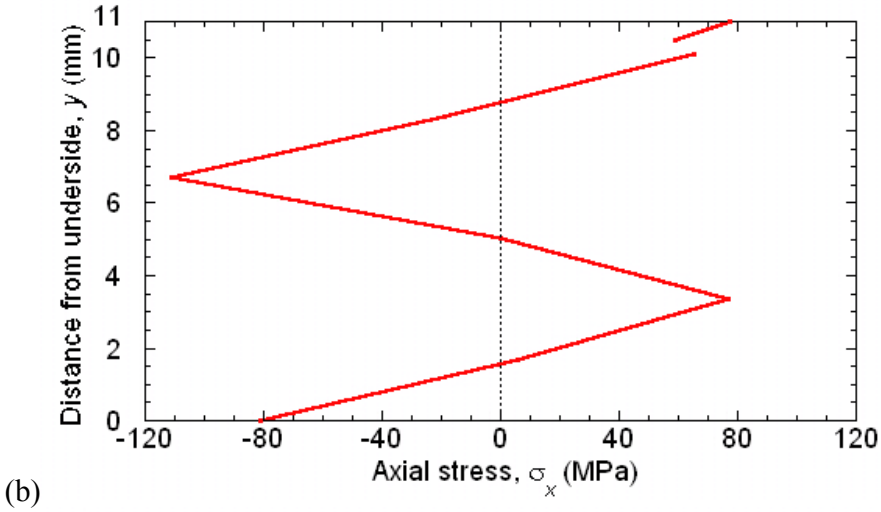

(b)

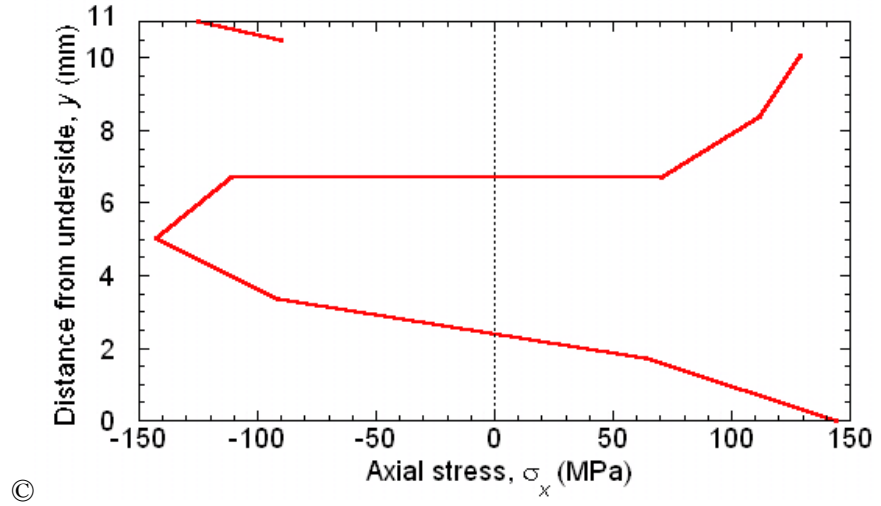

©

Figure 75: Predicted axial stress profiles a) at the solidified melting pool, b) at a point after the melting pool, c) at the final step of the analysis.

To verify the strong coupling between the coating stress field and the substrate bending, the mechanical analysis of the model was repeated using different boundary conditions. The model predicts that the coating is in tension when the back surface of the substrate is fixed, as shown in Figure 76. According to the stress analyses, the stress state of the coating strongly depends on the curvature that the substrate.

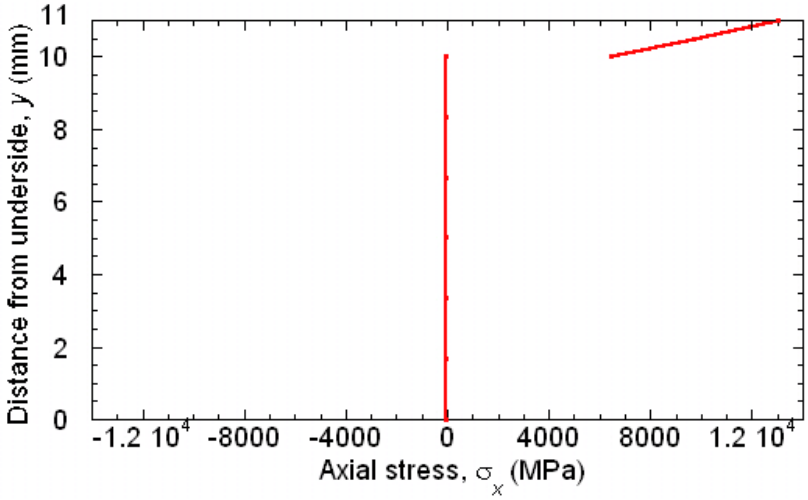

Figure 76: Predicted axial stress profiles of a laser clad specimen when the substrate is fixed.

8.2.4 Conclusions of the thermal and stress modelling

The following conclusions can be drawn from this modelling.

(a) A simple experimental set-up has been used to study the laser cladding process. A long, narrow substrate shape was used, clamped at one end, with an MMC powder being progressively deposited along part of its length, starting at the free end. A 3-D numerical finite element model was employed to simulate the associated heat flow and mechanical deformation. Comparisons have been made between measured and predicted thermal and specimen deflection histories. This specimen shape allowed attention to be focussed on the effects occurring during a single pass of the laser beam, primarily as a consequence of heat flow parallel to the direction of beam motion and in the through-thickness direction. Typical laser beam translation velocities are sufficiently high to ensure that the motion has a strong influence on the nature of the thermal field.

(b) During laser cladding, high thermal gradients tend to develop in the through-thickness direction. The associated differential thermal contraction often generates relatively high stresses, which are likely to cause yielding in the hot, near-surface regions. This plastic deformation leads to the generation of residual stresses and also tends to cause residual distortion of the work-piece. The specimen underwent changes in curvature during the process and these were in good agreement with predictions from the model, as were the observed thermal histories. It is therefore clear that the main thermo-mechanical features of the process have been captured in the model, which could be used to predict and

control stress generation and distortion during laser cladding of shaped components.

(c) The deposition of the coating, which in the present work was a Ni-based MMC, actually has relatively little effect on these thermomechanical phenomena occurring in the substrate, or on the residual stresses. This is unsurprising, partly because the coating is relatively thin and partly because much of the injected heat from the laser beam goes directly into the substrate, with only a relatively small proportion being first absorbed by the coating powder as it is deposited onto the substrate surface. However, there is a tendency for the cladding layer to be left under substantial residual stress at the end of the process, particularly if the substrate is able to adopt curvature (distort). For the conditions of these experiments, the cladding was left in residual compression, and this is likely to be the case under a wide range of conditions.

8.3 Decohesion modelling

A finite element model (FEM) simulating the stationary decohesion of a thick hard coating from a strain-hardening substrate after a first transverse coating crack has been developed in the framework of the COSTA project (figure 77). The aim of the model, done with ABAQUS code, is to determine the value of the interface toughness for strongly adherent thick coatings, in parallel with controlled straining tensile tests.

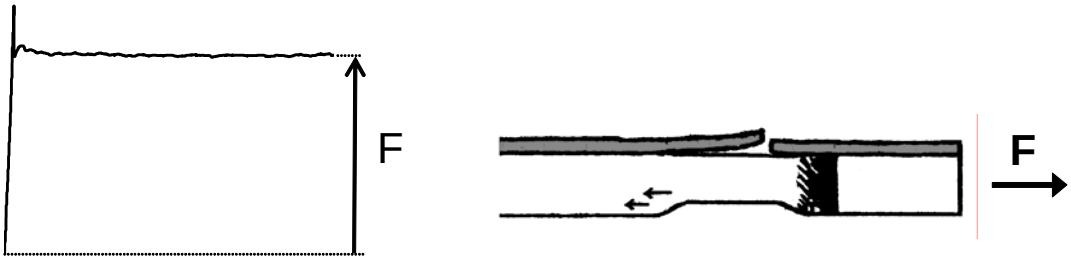

Figure 77: Stationary decohesion of thick coating with plastic deformation of substrate.

A cohesive zone model (CZM) is applied at the interface. The chosen CZM can be seen has fictitious springs connecting each interfacial substrate node to the corresponding interfacial coating node (figure 78). All these springs have the same mechanical behaviour, called the cohesive law, shown on figure 79; this law has a varying elastic modulus for the connector. The main parameters of this law are the maximum stress and opening displacement (COD) sustained by the spring and the fracture toughness (which is the integral of the stress/opening law). This cohesive zone simulates what is called the fracture process zone (FPZ) in front of the crack tip and has the capability of transferring stresses through material bonding until the COD reaches a critical value.

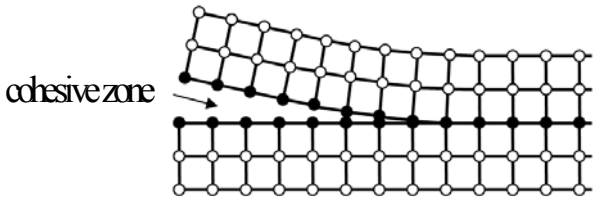

Figure 78: Cohesive zone model to simulate the interface.

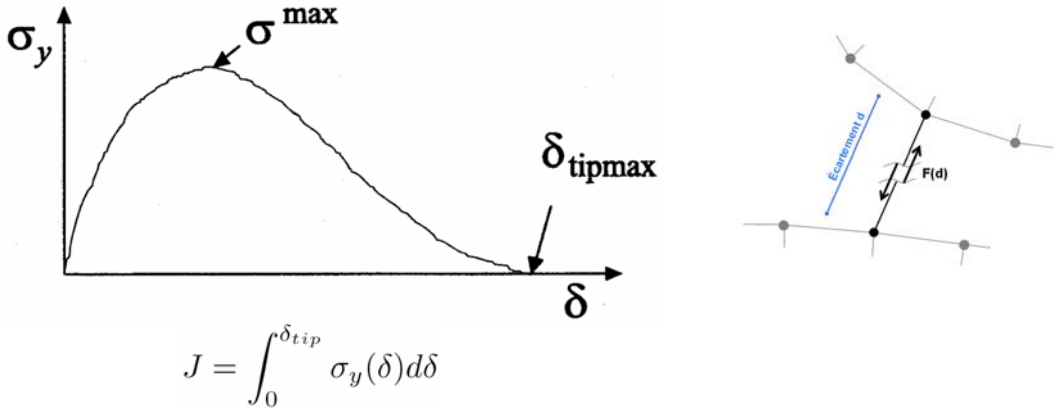

Figure 79: Parameters of the cohesive zone model: mode I opening simulated with spring connectors.

In our model, the coated sample is represented with 8 or 6 nodes linear finite elements as in figure 80, with

- a transverse plane of symmetry (A)
- a longitudinal plane of symmetry (B)
- an interfacial CZ on part of the sample (CZM)

The dimensions and elastic/plastic properties of the substrate and coating are defined in the model, as well as the cohesive law which is quite simple as it does not take into account the different fracture modes (pure opening, in-plane shear, out-of-plane shear) and the mode mixity of decohesion.

A displacement of the substrate face under the transverse crack (g) is imposed to the sample. In function of the cohesive law given to the interface and the mechanical properties of the materials, three modes of damage may appear:

- initiation and propagation of decohesion at the interface under a stationary mode at a constant force (figure 81);
- localisation of the deformation in the substrate under the cracked coating and fracture of the substrate;
- further transverse cracking of the coating.

The interest of the cohesive zone FE model is its capability to simulate the three damage modes (the transverse cracking has still to be implemented).

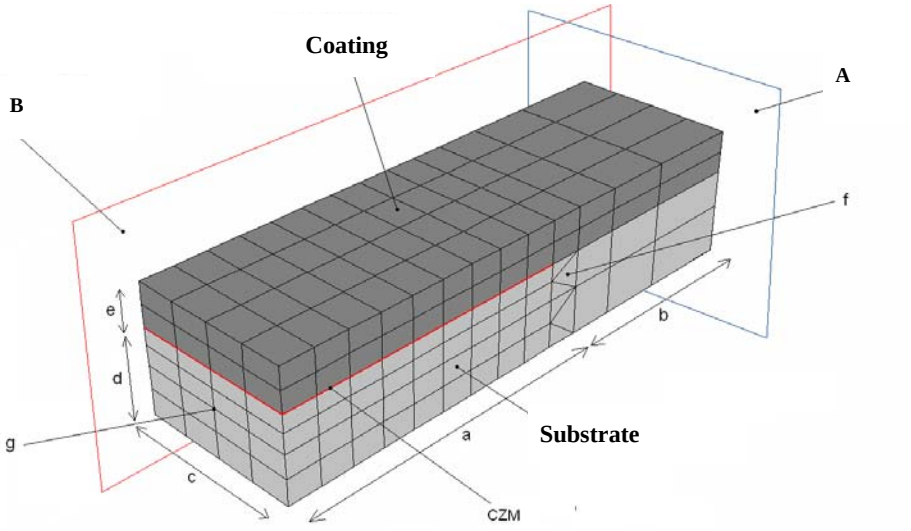

Figure 80: View of the sample meshing..

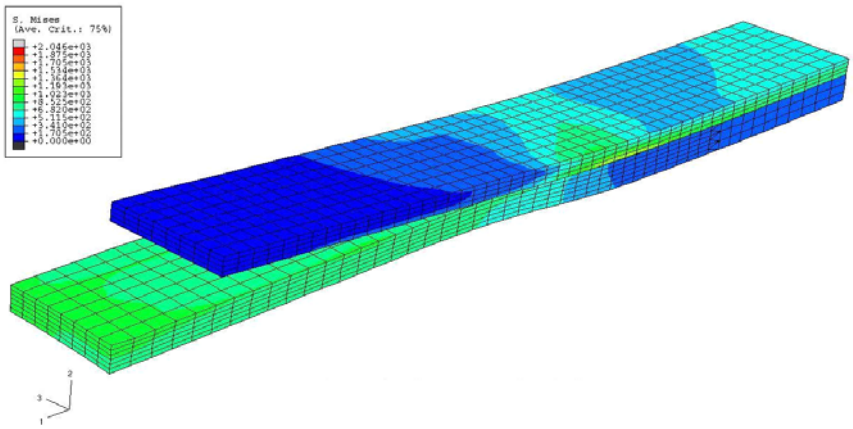

Figure 81: Mises stresses during simulation of decohesion of a laser clad 304 stainless steel sample for an interfacial toughness of 31.1 kJ/m^2.

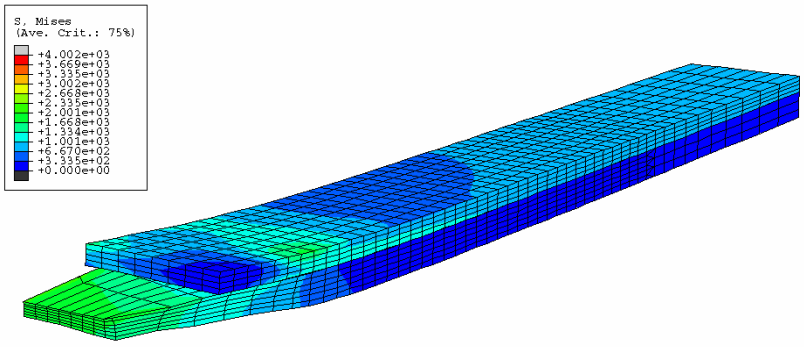

Figure 82: Mises stresses during simulation of decohesion of a laser clad 304 stainless steel sample for an interfacial toughness of 67.5 kJ/m2.

To validate the FEM developed here, the properties of the laser clad stainless steel samples tested in the framework of the COSTA project have been put in the model:

- stainless steel 304 substrate:

$E_s = 210\ GPa$

$\nu_s = 0.3$

$\sigma_s = 170 + 100 \cdot \varepsilon + 1375.838984 \cdot \varepsilon^{0.556358}\ MPa$ (*fit of tensile tests done on* 304 *samples*)

- Ni alloy with 40% WC coating:
-

$E_c = 350\ GPa$ (*measured*)

$\nu_c = 0.3$ (*assumption*)

$\sigma_{yc} = 1250\ MPa$ (*assumption*)

$\sigma_{\max c} = 4250\ MPa$ (*assumption*)

The cohesive zone law has been fitted on the results obtained by controlled straining on one laser clad 304 sample with a Cu interlayer ($h_c = e = 0.78$mm, $h_{si} = d = 1.32$ mm and $c = 6.24$ mm). The stationary force needed to propagate the decohesion at the interface was 10200 N. To obtain this force with the simulation, the cohesive law has been designed with a maximum force of 52 N and a critical opening displacement of 0.4 mm (see figure 82).

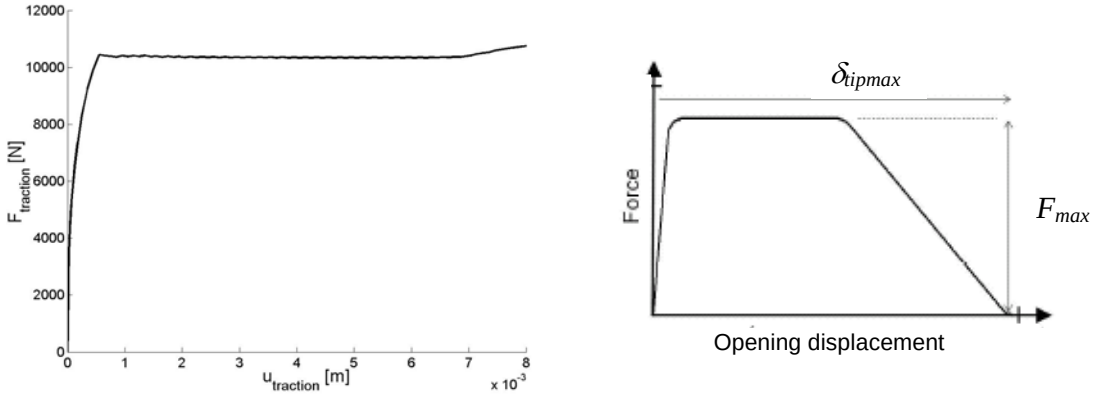

Figure 83: Simulated Cu layer sample stationary force/displacement curve obtained with a CZ law with F_{max} of 52 N and δ_{tipmax} of 0.4 mm (interfacial toughness of 31.1 kJ/m^2).

The same cohesive law is then applied to other substrate thicknesses in the model and comparison of the stationary force needed to propagate interfacial decohesion is made between the results obtained on tensile tested laser cladded samples with a Cu interlayer and the ones obtained with the FEM (figure 8). The concordance of the results shows a real adequation of the model with the controlled straining tests. With the model, the critical substrate thickness for which localisation appears is found to be of 0.56 mm.

The energy needed to break a "spring" is 18.936 mJ. The cohesive law developed in this case is dependent on the node density as a force/COD law is used instead of a stress/COD one. The interfacial fracture toughness given by the model is 31.1 kJ/m^2, which is of the same order of magnitude but below the analytical interfacial toughness, this latter being an upper bound as demonstrated in WP3.

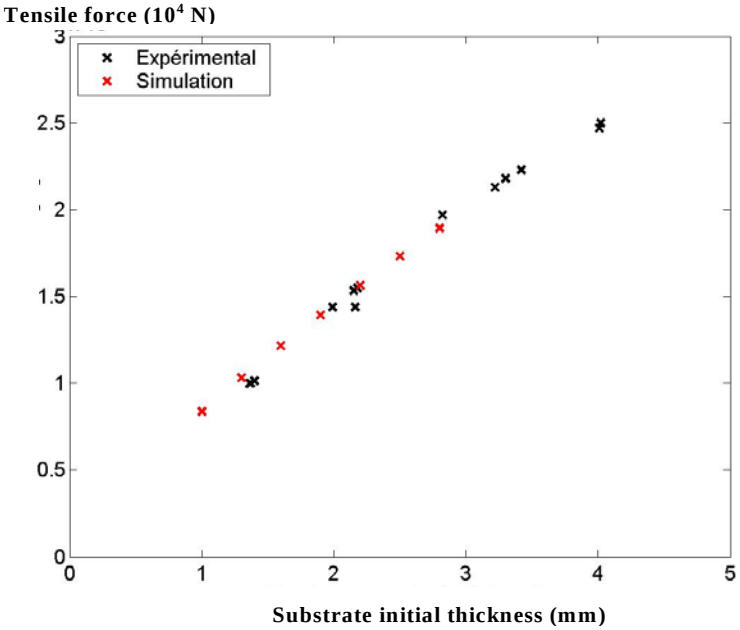

Figure 84: Comparison of the evolution of the tensile debonding stationary force obtained experimentally and with the FEM simulation in function of the substrate initial thickness for laser coated (h_c of 0.8 mm) samples having a Cu interlayer.

8.4 Conclusion

The internal stress state in the thick laser clad coating and the substrate has been calculated using FEM modelling. First, 3D heat flow modelling of laser cladding, based on simulation of conductive, convective and radiative heat transfer, predicts accurately the temperature profile of the substrate. Laser heating generates high T's and T gradients that lead to plastic deformation of the substrate. The coating deposition process has been modelled in FEM using element deactivation and reactivation and assuming elastic-perfectly plastic deformation behaviour. Creep effects have been neglected and the clad (particulate metal matrix composite) has been treated as a continuum. The results of the3D modelling show that laser clad coating is in compression due to the bending of the substrate. Comparisons between measured and simulated thermal fields and specimen deflection histories indicate that the main features of residual stress generation in this type of system have been captured in the model.

A FEM with cohesive zone at interface is developed to measure the exact interfacial toughness. The method simulates the stationary interfacial debonding in a uniaxial tensile test of a thick hard coating on a strain hardening substrate after a first transverse coating

crack has appeared. The model imposes a cohesive zone at the interface, consisting of fictitious springs connecting each interfacial substrate node to the corresponding interfacial coating node. The plastic behaviour of the substrate is known through separate tensile tests on uncoated substrates. The model results for the tensile debonding stationary force have been compared with experiments and show the same dependency of the substrate thickness. The calculated value for the interfacial fractgure toughness is of the same order of magnitude, but lower than the analytical values which constituted an upper bound.

9 VALIDATION – WP5

9.1 Interlaboratory exercise

As proposed, an interlaboratory exercise was organised based on the tensile test methodology for measuring the adhesion strength of the laser clad coating and the austenitic stainless steel substrate. The partners for this exercise were VITO, UCL, University of Cambridge (UCam), WTCM, BIL and K.U.Leuven/MRC (Leuven Materials Research Centre).

9.1.1 Test set-up

All tensile tests were executed at a cross head displacement of 1 mm/min. A preload at 100N before testing was imposed. The tests were proceeded up to about 15% of strain (around 10 mm of elongation).

Because of the important influence of the ratio of coating and substrate thickness, various sample thicknesses were used ranging from 2,0 mm to 3,0 mm (total thickness). The width and length at the prismatic section of the test samples instead depended on the load capacity of the available tensile test equipment. The specimen dimensions prior to testing are summarised in the following table 9-1 together with the initial distance for strain measurements on the test samples. The sides of the samples should be polished with SiC paper 320.

In order to establish the validity of the proposed test methodology for less adhesive coatings, some of the samples were coated after depositing a Cu-layer on the stainless steel surface.

Table 9-1: Nominal initial size of test specimens used by the partners for the interlaboratory exercise

Partner	Thickness (mm)	Width (mm)	Prismatic length (mm)	Initial distance for strain measurements (mm)
VITO	2,2 and 3,0	7,8	55,0	25,0
UCL	2,0 and 2,8	7,7	50,0	40,0
UCam	2,5 and 3,0	7,7	55,0	not applicable
WTCM	2,0 and 2,8	7,8	53,0	40,0
BIL	2,0 and 2,8	12,5	55,0	not applicable
K.U.Leuven	2,0 and 2,8	7,8	50,0	not applicable

Nearly all partners recorded plots of load against cross head displacement. Some partners also followed the actual strain by means of an extensometer positioned onto the specimen or optically. VITO measured cross head displacement or specimen strain. Strain measurements allow determining the specimen deformation at the occurrence of the first

crack in the coating. After this discontinuity, such measurements though are often uncertain as they depend on the crack location with regard to the position of the extensometer while also severe slipping of the extensometer may occur due to the shock effect of the crack.

If tensile testing is used for measuring adherence strength, then the former explains why recording of cross head displacement should be done in any case as these are less influenced by disturbances arising from crack phenomena. In order to compare cross head displacements for different specimen designs, it is preferable to express these for instance relative to the length of the prismatic specimen portion, which has been done for the subsequent evaluation. To take account of initial slipping of the specimen ends in the machine clamps, the elastic portion of all relevant plots have been linearised, i.e. the origin of the displacement has been corrected.

9.1.2 Results for debonding stress

The most important data for all interlaboratory tests are summarised in tables 9-2 to 9-6 including stress, relative displacement over prismatic length and strain corresponding with the occurrence of the first crack in the coating, the debonding stress and the specimen behaviour. An example of displacement-load curves is given in figure 85 and the results for the debonding stress are shown in figure 86.

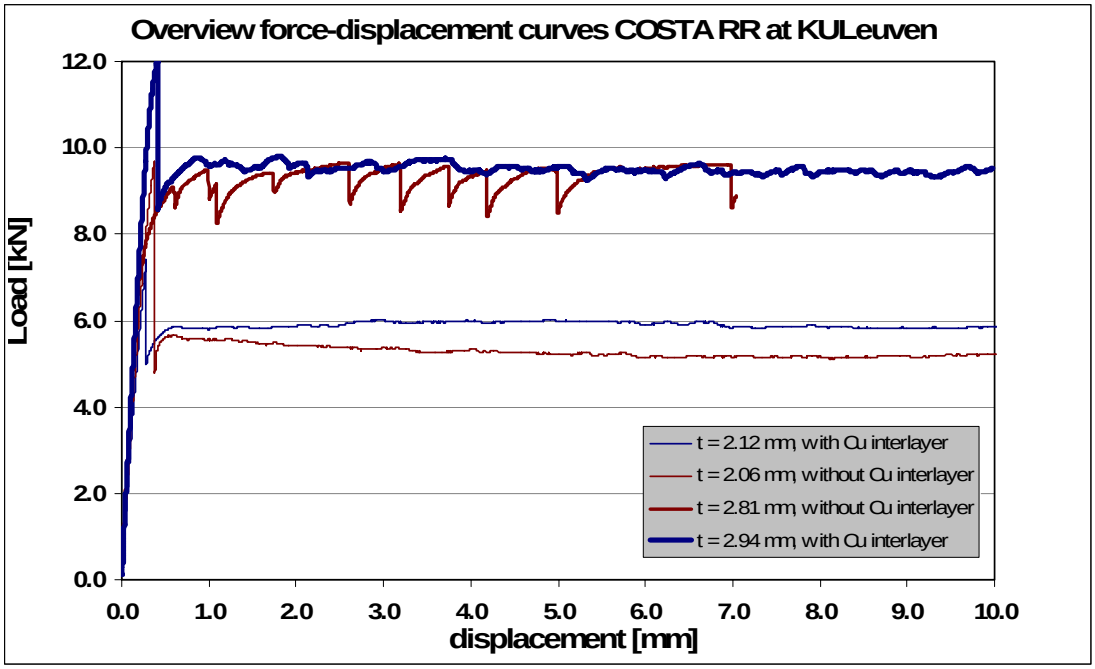

Figure 85: Comparison of the evolution of the tensile debonding stationary force obtained experimentally and with the FEM simulation in function of the substrate initial thickness for laser coated (h_c of 0.8 mm) samples having a Cu interlayer.

Table 9-2: Tensile test results of the 2,0 mm thick (nominal) laser clad samples

Partner	Adhesion strength [*]	Data at occurrence of first crack			Debonding stress	Specimen behaviour
		Stress	Relative displacement	Strain		
(-)	(-)	(MPa)	(%)	(%)	(MPa)	(-)
UCL	weakened	581	4,40	0,28	890	1 crack + debonding
		477	3,88	0,20	890	1 crack + debonding
	normal	193	2,22	? [**]	866	1 early crack + debonding
		491	3,78	0,23	849	1 crack + debonding
WTCM	weakened	458	2,98	0,19	788	1 crack + debonding
		561	3,26	0,37	815	1 crack + debonding
		563	3,58	0,40	739	1 crack + debonding
	normal	547	3,55	0,29	777	1 crack + debonding
BIL	weakened	510	3,65	-	708	1 crack + debonding
		510	2,80	-	671	1 crack + debonding
	normal	544	2,80	-	?	brittle fracture
KUL	weakened	454	0,56	-	753 [***]	1 crack + debonding
	normal	606	0,76	-	713 [***]	1 crack + debonding

[*] Weakened adhesion strength was achieved by means of interfacial Cu-layer
[**] Inaccurate measurement (irrelevant plot)
[***] Stress based on initial substrate width

Table 9-3: Tensile test results of the 2,2 mm thick (nominal) laser clad samples

Partner	Adhesion strength [*]	Data at occurrence of first crack			Debonding stress	Specimen behaviour
		Stress	Relative displacement	Strain		
(-)	(-)	(MPa)	(%)	(%)	(MPa)	(-)
VITO	weakened	442 [**]	-	0,43	688 [***]	1 crack + debonding
		532	1,69	-	821 [***]	1 crack + debonding
	normal	457 [**]	-	0,43	783 [***]	1 crack + debonding
		465 [**]	-	0,49	860 [***]	1 crack + debonding

[*] Weakened adhesion strength was achieved by means of interfacial Cu-layer
[**] Inaccurate data (true data point missing in plot)
[***] Stress based on initial substrate width

Table 9-4: Tensile test results of the 2,5 mm thick (nominal) laser clad samples

Partner	Adhesion strength [*]	Data at occurrence of first crack			Debonding stress	Specimen behaviour
		Stress	Relative displacement	Strain		
(-)	(-)	(MPa)	(%)	(%)	(MPa)	(-)
UCam	weakened	520 [**]	0,58	-	841	several cracks
		464 [**]	0,47	-	789	2 cracks + debonding
	normal	552 [**]	0,73	-	758	1 crack + debonding
		530 [**]	0,55	-	760	2 cracks + debonding

[*] Weakened adhesion strength was achieved by means of interfacial Cu-layer
[**] Inaccurate data (based on nominal cross section or thickness)

Table 9-5: Tensile test results of the 2,8 mm thick (nominal) laser clad samples

Partner	Adhesion strength [*]	Data at occurrence of first crack			Debonding stress	Specimen behaviour
		Stress	Relative displacement	Strain		
(-)	(-)	(MPa)	(%)	(%)	(MPa)	(-)
UCL	weakened	505	4,94	0,20	751	2 cracks + debonding
		448	3,18	0,21	794	3 cracks + debonding
	normal	489	4,76	0,23	743	multiple cracks
		409	3,88	0,11	772	multiple cracks
WTCM	weakened	511	3,81	0,32	705	2 cracks + debonding
		518	3,81	0,39	?	2 cracks
	normal	380	3,53	0,11 [**]	?	1 crack
		451	3,70	0,22	622	2 cracks + debonding
BIL	weakened	431	3,25	-	643	2 cracks + debonding
		365	2,84	-	712	2 cracks + debonding
		368	4,05	-	???	multiple cracks
	normal	377	4,05	-	???	multiple cracks
		350	4,38	-	728	1 crack + debonding
KUL	weakened	530	0,82	-	633 [***]	1 crack + debonding
	normal	414	1,20	-	?	several cracks

[*] Weakened adhesion strength was achieved by means of interfacial Cu-layer
[**] Inaccurate measurement (irrelevant plot)
[***] Stress based on initial substrate width

Table 9-6: Tensile test results of the 3,0 mm thick (nominal) laser clad samples

Partner	Adhesion strength [*]	Data at occurrence of first crack			Debonding stress	Specimen behaviour
		Stress	Relative displacement	Strain		
(-)	(-)	(MPa)	(%)	(%)	(MPa)	(-)
VITO	weakened	365 [**]	-	0,37	681 [***]	several cracks + debonding
	normal	493	2,13	-	668 [***]	multiple cracks
		428	2,20	-	630 [***]	1 crack + debonding
UCam	weakened	531 [**]	0,84	-	713	several cracks + debonding
	normal	491 [**]	0,56	-	734	1 crack + debonding
		478 [**]	0,58	-	?	several cracks
		345 [**]	0,33	-	?	1 early crack + multiple cracks

[*] Weakened adhesion strength was achieved by means of interfacial Cu-layer
[**] Inaccurate data (true data point missing in plot or based on nominal cross section or thickness)
[***] Stress based on initial substrate width

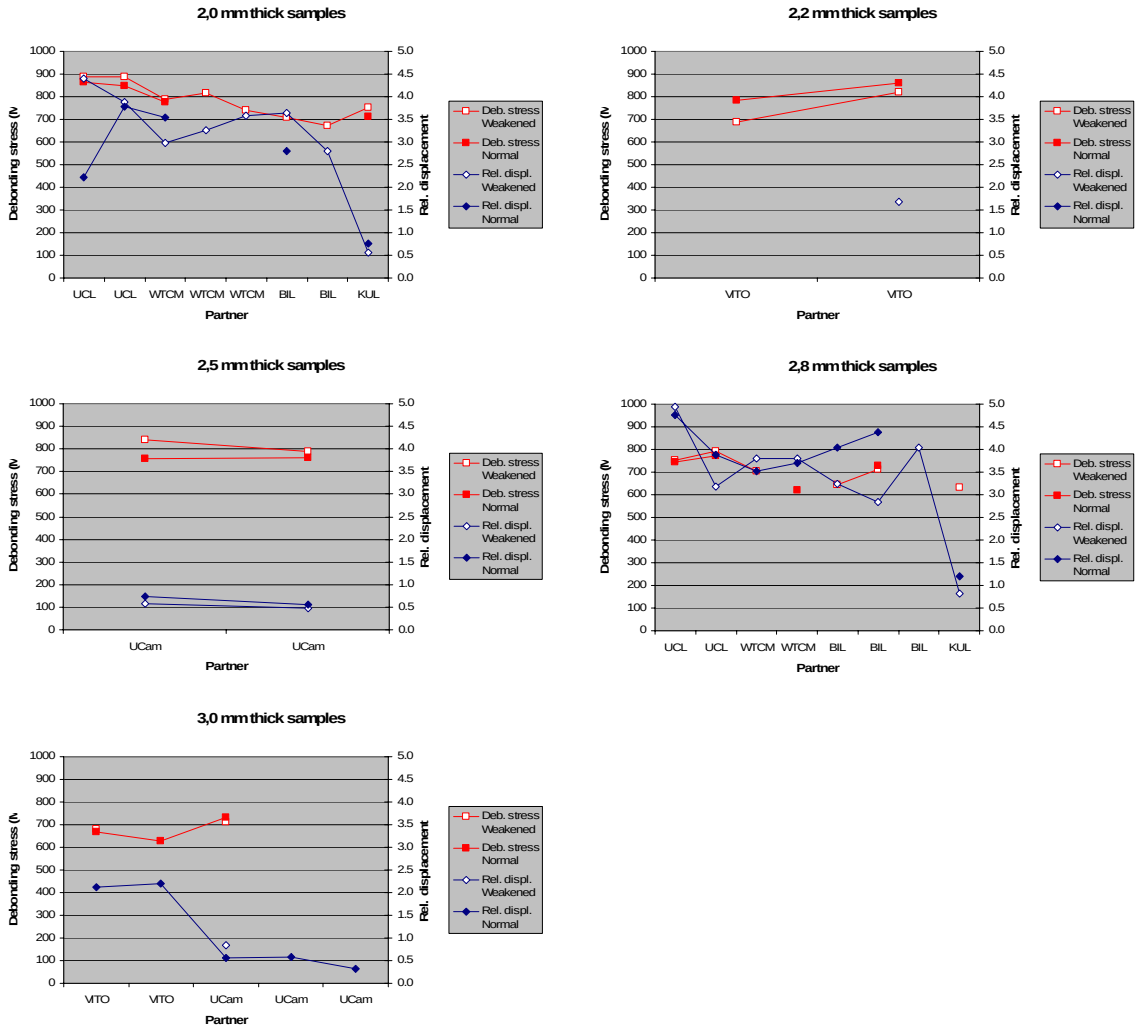

Figure 86. Results for the debonding stress at different substrate thickness.

As expected, the specimen behaviour for a thickness not above 2,2 mm and irrespective of the test house is governed by the occurrence of one crack at the coating followed by a continuous debonding of the coating. Such conditions are well fit for determining the adhesive strength of the laser cladding. Thicker samples tend to develop more cracks and therefore suppress debonding.

The debonding stress for 2,0 mm thick specimens varies between 713MPa (value should be higher for reasons explained before) and 866 MPa and between 671 MPa and 890 MPa respectively for the normal and weakened condition at the interface and this argues for test methods based on multiple specimens in order to obtain a good idea of the average adhesion strength between a coating and a substrate. It should be noted though that the mean debonding stress values vary between the partners involved, while no systematic difference is noticed between the normal samples and the so called weakened samples (with a Cu-layer). The trend for the 2,8 mm thick specimens is more or less

identical but debonding stresses for both conditions are less (between 622 MPa and 772 MPa and between more than 633 MPa and 794 MPa).

The relative displacement of the 2,0 mm thick samples at which the first crack occurs is fairly constant (generally between 2,2% and 3,8% for the normal condition and between 2,8% and 4,4% for the weakened condition) although one partner recorded early cracking already between 0,5% and 0,8%. The variation for the 2,8 mm thick specimens was even more restricted, especially for the normal condition as the relative displacement in this case changed only from 3,5% to 4,8%. Unfortunately, specimens evaluated again by one partner (same as before) cracked already at 0,8% or 1,2%.

Also the actual strain measured directly onto the specimen and coinciding with the first crack for samples with a thickness of 2,0 mm or 2,8 mm did not vary much between partners and ranged in general from 0,2% to 0,4%. Only in one instance did the coating crack at 0,11%.

The same trend holds for the other sample thicknesses of 2,2 mm, 2,5 mm and 3,0 mm where smaller series of tests have been executed. This means that debonding stress values are rather constant for each thickness separately and again the trend is that this adhesion strength tends to lower for increasing specimen sizes. One partner recorded relative displacements over the prismatic section at the occurrence of a first crack already at about 0,5%, irrespective of specimen thickness, and therefore always much lower than the other partners.

The conclusion from this interlaboratory exercise is that indeed pronounced debonding occurs for low ratios of substrate thickness to coating thickness. Multiple cracking instead may take place in case of higher ratios preventing the calculation of the adhesion strength. This also favours the choice of the tensile test as an appropriate test method for determining the interfacial strength of strongly adherent coatings.

It is recommended in this case to carefully record a plot of applied force against cross head displacement over a sufficient displacement range enabling the calculation of the mean debonding force. Direct strain measurements of the coating do not seem necessary but give an idea of the (low) deformation capacity of the coating before cracking occurs. Various pre- and post-test measurements of substrate and coating sizes are necessary to improve the accuracy of the results. The so determined data are considered as representative, as shown by the present interlaboratory exercise, but are liable to normal scatter originating from variations in production of the cladding and from the usual uncertainty of recording data under laboratory conditions.

9.1.3 Calculation of the interfacial toughness and results

The interfacial toughness has been calculated with the formula 7-3. The final strain of the substrate, needed for this formula, can be either derived from the measurement of the elongation of the delaminated part of the substrate after the test, or from the ratio between the section of the substrate in the delaminated part to the initial section of the substrate. The results are respectively shown in figure 87 and 88. It can be concluded that the interfacial toughness is not dependent on the substrate thickness (on condition the thickness is small enough to allow for stable debonding).

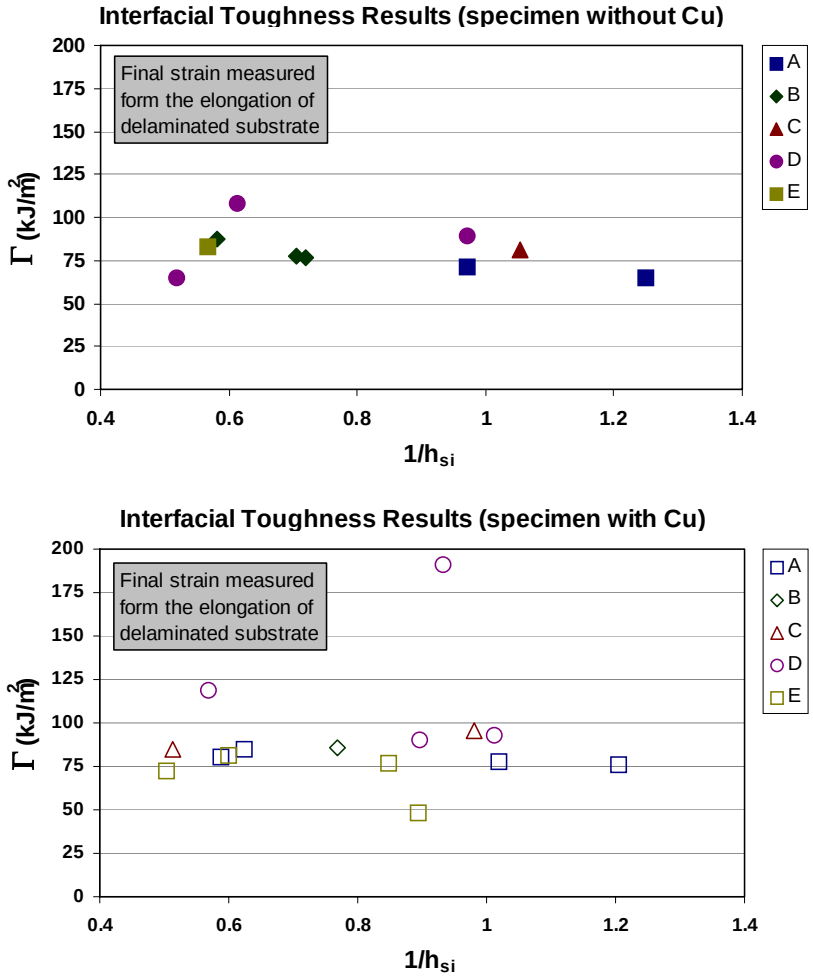

Figure 87: Test results of the interlaboratory exercises. The interfacial toughness is calculated, based on the final strain derived from the elongation of the delaminated part of the substrate.

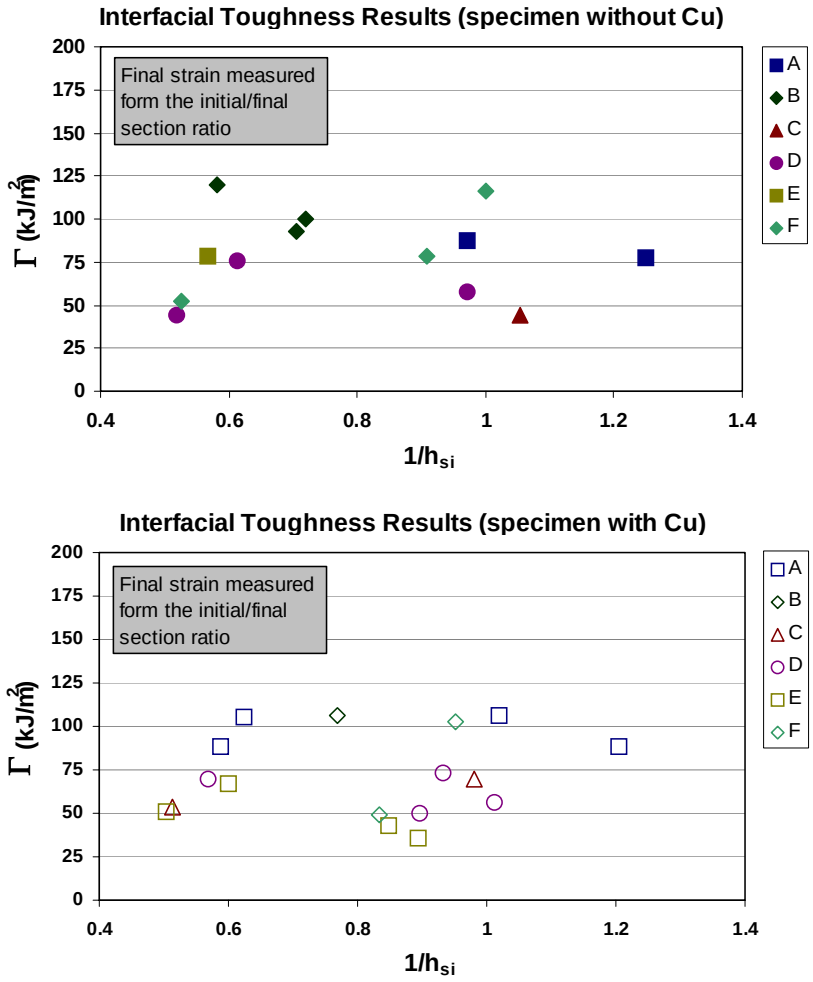

Figure 88: Test results of the interlaboratory exercises. The interfacial toughness is calculated, based on the final strain derived from the initial/final section ratio.

Since the calculations based on the ratio final/initial section gives the most complete set of data, the results from these calculations are further evaluated statistically. The reproducibility and repeatability of the results were analysed following the procedure laid down in ISO 5725 Part 2 [49]. Only the results of the laboratories who performed more than 1 test on a particular type of specimen, could be taken into account for the statistical evaluation. The results are summarized in table 9-7.

Table 9-7: Results of analysis of reproducibility and repeatability to ISO 5725 (Figures in brackets are percentage of means)

	Without Cu at the interface	With Cu at the interface
Number of participants	4	5
	Γ (kJ/m²)	Γ (kJ/m²)
Mean	81.9	69.2
sr	20.8 (18)	15.8 (33)
sR	25.5 (31)	27.9 (40)

For the tests on the laser clads without Cu at the interface, the repeatability (within labs) standard deviation sr is 18% for the interfacial toughness Γ . The reproducibility (between labs) standard deviation sR is 31% (see also figure 89 for an impression of the spread of the results within and between laboratories). The values for the samples with Cu at the interface are slightly less accurate: the repeatability is 31%, the reproducibility 40%. Remark the mean value of the interfacial toughness is indeed lower with Cu at the interface, than the value for the original laser clad. These values of reproducibility and repeatability are considered to be acceptable for an adhesion test.

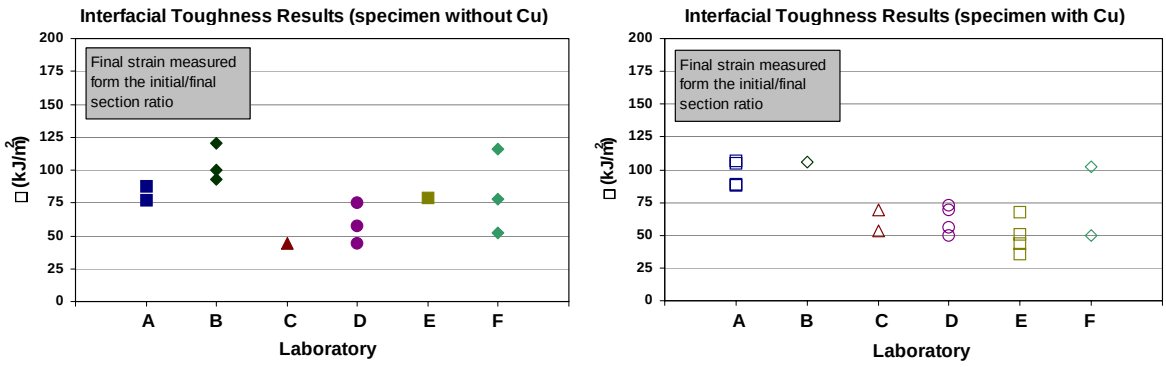

Figure 89. Test results of the interlaboratory exercises per laboratory. The interfacial toughness is calculated, based on the final strain derived from the initial/final section ratio.

9.2 Test procedures

The convenor of CEN Technical Committee 184, work group 5 (CEN/TC184/WG5) was contacted about how the measurement procedure developed within this project can be transformed in a CEN standard or guideline.
Since the proposed document is a test method containing a prescribed, recommended procedure for carrying out the test, an EN or CEN/TS seems to be the correct deliverable. The measurement method has been introduced as a new work item at the WG5-meeting at WTCM in Diepenbeek on February 10th, 2006 and will be further evaluated within the frame of this work group.

9.3 Other adhesion test methods : Indentation methods

At the beginning of the project, it was the objective to verify the obtained adhesion test with other adhesion test results. However, as discussed already above, no other adhesion tests are able to yield results on the thick and well-adherent coatings. One candidate was in the beginning believed to have some potential, but as will be seen below, also this test did not yield any result. This confirms the strain induced delamination test is the only alternative.

Indentation near the interface on a cross section of the coating can cause delamination. The length of the delaminated zone upon a certain indentation load and geometry, can be considered as a measure of the interfacial strength.

Several indentation tests had been done on cross sections of laser clad samples with a microVickerstester (maximum load 200 grams). (fig. 90). As can be seen from these photos the diagonals of the indentation are nearly perfectly aligned parallel with and perpendicular to the interface. The diagonals are between 20 and 25 µm for the 100 gram indentation, between 30 and 35 µm for the 200 gram indentation. Although it was possible to cause delamination and introduce cracks along the interface with this technique when used for thin ceramic coatings (like TiN, up to 5 µm thick) it wasn't possible to achieve the same results for the laser clad coatings. No cracks have been generated by this method.

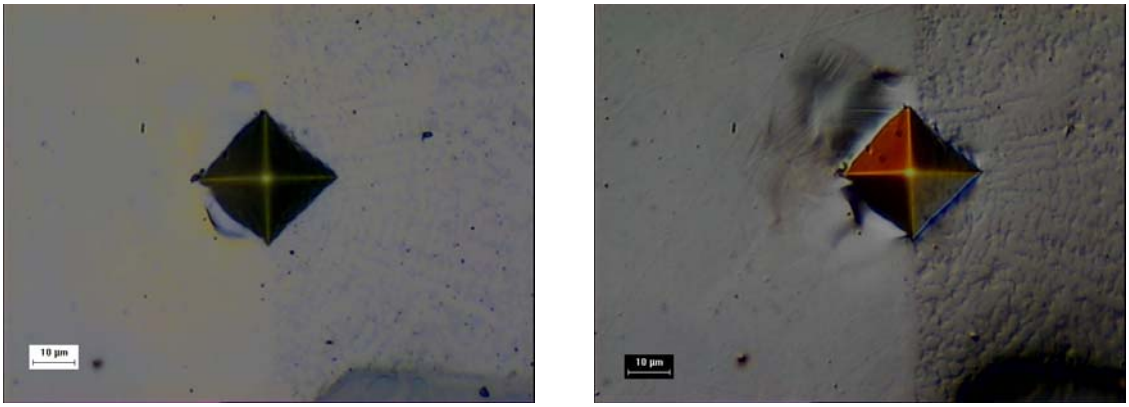

Figure 90: interface indentation with 200 gram load. The laser clad coating is at the lef ton the picutres. Left is a picture taken with bright field light, right with polarised light.

Using a Vickerstester and going up to 30 kilo wasn't successful neither (see figure 32): no delamination nor crack formation could be observed.

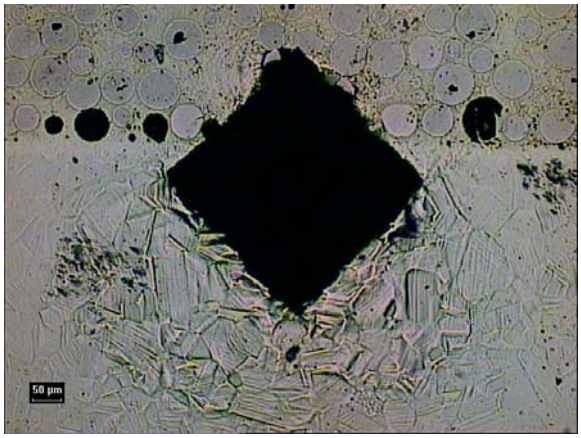

Figure 91:Vickers interface indentation at 30 kg..

Trials have also been performed on PEO coatings. During indentation of the aluminium substrate in a mounted cross-section, the indenter induced plastic deformation. Figure 92 is an SEM micrograph of a 20 N micro-indent. Cracks appear to start at the interface in this case but they rapidly deflect into the coating. This deflection is expected since the toughness of the coatings is relatively low. Nevertheless some cracks did appear to propagate for measurable distances along the interface before being deflected into the coating. This suggests that a more appropriate indent geometry could be used to propagate cracks further along the interface, allowing a quantitative measure of interfacial adhesion.

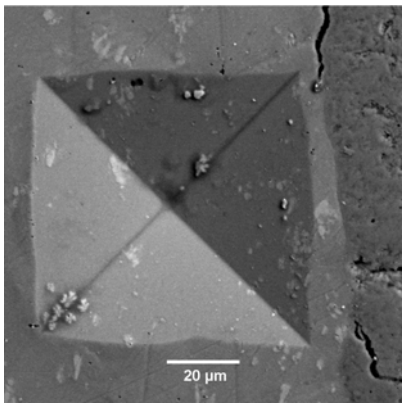

Figure 92. A 20 N indent in the Al substrate induces limited crack-propagation along the interface.

It can be concluded the interface indentation method is not applicable on laser clad not on PEO coatings.

10 CONCLUSIONS

There is in general a need for a more quantitative adhesion and damage resistance test method for well adherent thick coatings. An extended literature survey conducted in the beginning of the project proves this need. More specifically, there is only very few work done on the adhesion determination in laser clad as well as in Keronite coatings. The adhesion of those coatings is experienced as very good but is not understood yet. There was no suitable test method available for the assessment of the adhesion of those coatings. Even promising methods such as the interfacial indentation test, explored as well in this project, are not suited for the coatings studied here. The project aimed to fill up the gap of adhesion testing for thick well-adherent coatings.

The project focussed on the adhesion of thick well adherent coatings: viz. laser clad (LC) coatings and plasma electrolytic oxidation (PEO) coatings. The coatings have been optimised for the needed sample geometry and the selected material combination, namely Ni/45%WC on stainless steel AISI 304. Keronite coatings have been grown on Aluminium samples.

It is evident thorough examination of the coatings is indispensable as a solid basis for developing an adhesion test and for a better understanding of the results. Microstructural characterisation of the deposited coatings showed the metallurgical bond of the coatings to the substrate on the one hand, and the complexity in terms of phases and compositional changes on the other hand.

An overview has been made of the available mechanical test methods for intermediate and thick coatings. The overall hardness can be determined by Brinell and the hardness of the individual phases by instrumented nano-indentation. The E-modulus had to be determined on a free standing coating after labour-intensive grinding, by IET or four point bending. However, it is also possible to accurately calculated the overall E-modulus based on the values of the individual phases, obtained e.g. by nano-indentation. The determination of the internal stress was less straight-forward, though primordial for a correct calculation of adhesion strength. The classical methods by XRD and hole drilling were not successful, due to respectively the complex composition leading to a overlapping diffraction peaks and to the extreme hardness and abrasiveness of the WC carbides in the coating. Experiments have been set up to follow the bending of clad beams during deposition, and to etch the coating after deposition. The data of the former experiments were used as input for heat flow modelling of the laser cladding.

All mentioned methods have been evaluated on the laser clad coatings and most of them on the PEO coatings studied in this project. It can be concluded that the multiphase thick coatings, as LC coatings are, are extremely difficult to characterise, contrary to the general feeling that thick coatings are almost bulk materials and that the bulk test methods should apply. The hardness and Young's modulus were determined with success; however, the internal stress should only be estimated by developing complex models for the distortion during the deposition.

Four-point bending adhesion testing and pure mode I adhesion testing of coated substrates are the most obvious set up to impose a controlled straining. They were thoroughly examined, since the calculation of the adhesion is more straight forward. However, several test set-ups have been explored, with stiff overlayers and with pre-cracks, but none of them was successful in introducing delamination at the interface between the laser clad coating and substrate. They only yield lower boundary values for the adhesion strength.

Another way of imposing a controlled straining on a coating is by performing a tensile test. In such a test, the coated sample is subjected to an increasing tensile strain, causing the film to crack and break into segments. The crack initiation and further cracking and/or crack spacing can be observed optically or by acoustical emission. Tensile tests mostly are performed until multiple cracking occurs and the crack density reaches a saturation level. In the case of the studied laser clads, it turned out to be difficult to determine the maximum saturation crack spacing, which is needed to calculate the interfacial shear strength. Moreover, in such method the determined value of the interfacial shear strength is very much dependent on the model used for the stress distribution in the coating between the cracks, and it doesn't take possible delamination at the interface into account. It is not simple to check for delamination after the tensile test. Finally, the thickness and fracture strength of these thick coating is so high that the steel substrate deforms plastically at the crack tips.

The full fragmentation test method has been further explored with the use of image correlation. The crack initiation and crack growth during straining could be accurately followed in that way. It was found that differences in damaging behaviour could be accounted for by the different thickness ratios of the samples. Micro-tensile carried within a scanning electron microscope confirmed the observation of the competition between coating fracture toughness and the debonding due to the energy dissipated by the plastic deformation of the substrate. This means that the plastic strain in the substrate will be sufficient to propagate the interfacial debonding after a first transverse crack when coating and substrate have a critical thickness ratio, depending on the physico-mechanical properties of the materials as well as the interfacial properties.

Another approach of the controlled straining test has been derived from these experiments. The idea is that decreasing the substrate thickness h_{si} with respect to the coating thickness h_c will decrease the number of cracks in the coating and promote the delamination between the coating and substrate. The driving force for the delamination will increase, with decreasing substrate thickness and even a stable interfacial crack growth will be obtained due to the strain hardening of the substrate.

Single cracking followed by delamination has been obtained in the laser clad coated samples. The critical ratio h_c/h_{si} could be determined for coatings with and without Cu interlayer, i.e. respectively ± 0.25 and 0.4. The larger the number, the better the interfacial toughness. Stable debonding occurred at a constant force at and above this critical h_c/h_{si} ratio. In principle, coatings can be compared and ordered on basis of the

found critical h_c/h_{si} ratio. The method can clearly discriminate between highly adherent laser clad coatings.

An analytical model has been proposed to calculate the interfacial toughness from the plastic properties of the substrate and the elastic properties of both coating and substrate. This model yields an upper bound of the interfacial toughness. The latter is typically plotted in function of the inverse of the substrate thickness. One may observe on figure 66 the lower toughness of the interface containing a Cu interlayer and the quite high toughness of both interfaces studied here. These toughness values may be compared to the toughness of ductile metals where crack extension involves nucleation and growth of voids.

Further research was however indispensable to determine by FEM modelling the exact interface toughness based on the force needed for the stable delamination. A FEM with cohesive zone at interface is developed to measure the exact interfacial toughness. The method simulates the stationary interfacial debonding in a uniaxial tensile test of a thick hard coating on a strain hardening substrate after a first transverse coating crack has appeared. The model imposes a cohesive zone at the interface, consisting of fictitious springs connecting each interfacial substrate node to the corresponding interfacial coating node. The plastic behaviour of the substrate is known through separate tensile tests on uncoated substrates. The model results for the tensile debonding stationary force have been compared with experiments and show the same dependency of the substrate thickness. The calculated value for the interfacial fracture toughness is of the same order of magnitude, but lower than the analytical values which constituted an upper bound.

A modelling tool has been developed for the prediction of curvature and internal stress generation during cladding and after cooling to room temperature. The heat capacity has been successfully measured and the thermal conductivity calculated as additional input values for the model. First, 3D heat flow modelling of laser cladding, based on simulation of conductive, convective and radiative heat transfer, predicts accurately the temperature profile of the substrate. Laser heating generates high T's and T gradients that lead to plastic deformation of the substrate. The coating deposition process has been modelled in FEM using element deactivation and reactivation and assuming elastic-perfectly plastic deformation behaviour. Creep effects have been neglected and the clad (particulate metal matrix composite) has been treated as a continuum. The results of the3D modelling show that laser clad coating is in compression due to the bending of the substrate. Comparisons between measured and simulated thermal fields and specimen deflection histories indicate that the main features of residual stress generation in this type of system have been captured in the model.

Finally, the procedure for testing the coatings by the here developed strain-induced delamination test method has been proposed at CEN and a work item has been opened to standardize the method. A round robin with 6 participating laboratories has been set up and the results show an acceptable repeatability and reproducibility of the test results, which confirms the applicability of the proposed method.

REFERENCES

1. Katipelli, L.R., A. Agarwal, and N.B. Dahotre, *Interfacial strength of laser surface engineered TiC coating on 6061 Al using four-point bend test.* Materials Science and Engineering A, 2000. **289**(1-2): p. 34-40.
2. Kadolkar, P. and N.B. Dahotre, *Effect of processing parameters on the cohesive strength of laser surface engineered ceramic coatings on aluminum alloys.* Materials Science and Engineering A, 2003. **342**(1-2): p. 183-191.
3. Huang, S., M. Samandi, and M. Brandt, *Abrasive wear performance and microstructure of laser clad WC/Ni layers.* Wear, 2004. **256**: p. 1095-1105.
4. Kutsuna, M. and G. Xu, *Crack behaviour and microstructure of clad layer in laser cladding of stellite 6 and WC powder*, in *Proceedings of ICALEO 2004, 23rd International Congress on Applications of Lasers & Electro Optics*. October 4-7, 2004: San Francisco.
5. Man, H.C., Y.Q. Yang, and W.B. Lee, *Laser induced reaction synthesis of TiC+WC reinforced metal matrix composites coatings on Al 6061.* Surface and Coatings Technology, 2004. **185**: p. 74-80.
6. Tobar, M.J., et al., *Morphology and characterization of laser clad composite NiCrBSi-WC coatings on stainless steel.* Surface and Coatings Technology. **In Press, Corrected Proof**.
7. Navas, C., et al., *Abrasive wear behaviour of laser clad and flame sprayed-melted NiCrBSi coatings.* Surface and Coatings Technology. **In Press, Corrected Proof**.
8. Chen, H., et al., *Sliding wear behaviour of laser clad coatings based upon a nickel-based self-fluxing alloy co-deposited with conventional and nanostructured tungsten carbide-cobalt hardmetals.* Wear, 2005. **259**(7-12): p. 801-806.
9. Fernandez, E., et al., *Wear behaviour of laser clad NiCrBSi coating.* Wear, 2005. **259**(7-12): p. 870-875.
10. Van Acker, K., et al., *Influence of tungsten carbide particle size and distribution on the wear resistance of laser clad WC/Ni coatings.* Wear, 2005. **258**(1-4): p. 194-202.
11. Xue, W.B., *Microstructure and Mechanical Properties near Interface between Micro Arc Oxidation and Al Alloy Substrate.* Surface and Coatings Technology, 2000. **16**: p. 344-348.
12. Gnedenkov, S.V., *Composition and Adhesion of Protective Coatings on Aluminium.* Surface and Coatings Technology, 2001. **145**(1-3): p. 146)151.
13. Nie, X., *Thickness Effects on the Mechanical Properties of Micro-Arc Discharge Coatings on Aluminium Alloys.* Surface and Coatings Technology, 1999. **119**: p. 1055-1060.
14. Yerokhin, A.L., *Plasma Electrolysis for Surface Engineering (Review).* Surface and Coatings Technology, 1999. **122**(2-3): p. 73-93.
15. Meletis, E.I., *Electrolytic plasma processing for cleaning and metal-coating of steel surfaces.* Surface and Coatings Technology, 2001. **150**: p. 246-256.
16. Pei, Y.T., V. Ocelik, and J.T.M. De Hosson, *Interfacial adhesion of laser clad functionally graded materials.* Materials Science and Engineering A, 2003. **342**(1-2): p. 192-200.

17. Blickensderfer, R., *A multi-step shear test for bond strength of claddings.* Journal of Testing and Evaluation, 1984. **12**(1).
18. Choi, H.W., et al., *Fracture behavior of diamond-like carbon films on stainless steel under a micro-tensile test condition.* Diamond and Related Materials, 2006. **15**(1): p. 38-43.
19. Lin, C.-K. and C.C. Berndt, *Acoustic emission studies on thermal spray materials.* Surface and Coatings Technology, 1998. **102**(1-2): p. 1-7.
20. Delannay, F. and P. Warren, *On crack interaction and crack density in strain-induced cracking of brittle films on ductile substrates.* Acta Metallurgica and Materialia, 1991. **39**: p. 1061-1072.
21. Drory, M. and J.W. Hutchinson, Proc. Roy. Soc., 1996. **A452**(2319-2341).
22. Andritschky, M. and P. Alpuim, *Strength measurements of thin brittle ZrO2 coatings produced by magnetron sputtering on steel substrates.* Vacuum, 1997. **48**(5): p. 417-422.
23. Laribi, M., A.B. Vannes, and D. Treheux, *On a determination of wear resistance and adhesion of molybdenum, Cr-Ni and Cr-Mn steel coatings thermally sprayed on a 35CrMo4 steel.* Surface and Coatings Technology, 2006. **200**(8): p. 2704-2710.
24. Watanabe, M., et al., *Effect of WC size on interface fracture toughness of WC-Co HVOF sprayed coatings.* Surface and Coatings Technology. **In Press, Corrected Proof**.
25. Ye, M., et al., *Characterization and adhesion strength study of Zn coatings electrodeposited on steel substrates.* Surface and Coatings Technology, 1998. **105**(1-2): p. 184-188.
26. Chung, H.G.P., M.V. Swain, and T. Mori, *Evaluation of the strain energy release rate for the fracture of titanium-porcelain interfacial bonding.* Biomaterials, 1997. **18**(23): p. 1553-1557.
27. Kucuk, A., et al., *Influence of plasma spray parameters on mechanical properties of yttria stabilized zirconia coatings. I: Four point bend test.* Materials Science and Engineering A, 2000. **284**(1-2): p. 29-40.
28. Ollendorf, H. and D. Schneider, *A comparative study of adhesion test methods for hard coatings.* Surface and Coatings Technology, 1999. **113**(1-2): p. 86-102.
29. Richard, C.S., et al., *Four-point bending tests of thermally produced WC-Co coatings.* Surface and Coatings Technology, 1996. **78**(1-3): p. 284-294.
30. Andritschky, M., et al., *Study of the mechanics of the delamination of ceramic functional coatings.* Materials Science & Engineering A (Structural Materials: Properties, Microstructure and Processing), 1999. **A271**(1-2): p. 62-69.
31. Erickson, L.C., et al., *Cohesion in plasma-sprayed coatings-a comparison between evaluation methods.* Wear, 1998. **214**(1): p. 30-37.
32. Wiklund, U., et al., *Cracking resistance of thin hard coatings estimated by four-point bending.* Surface and Coatings Technology, 1997. **91**(1-2): p. 57-63.
33. Hjornhede, A. and A. Nylund, *Adhesion testing of thermally sprayed and laser deposited coatings.* Surface and Coatings Technology, 2004. **184**(2-3): p. 208-218.

34. Mesrati, N., et al., *Characterization of thermal fatigue damage of thermal barrier produced by atmospheric plasma spraying.* Surface and Coatings Technology, 2004. **187**(2-3): p. 185-193.
35. Hsueh, C.H. and A.A. Wereszczak, *Multiple cracking of brittle coatings on strained substrates.* Journal of Applied Physics, 2004. **96**(6): p. 3501-3506.
36. Kamiya, S., et al., *A comparative study of the mechanical properties of PVD coatings evaluated by new techniques and conventional methods.* Thin Solid Films, 2004. **469-470**: p. 248-253.
37. Kamiya, S., et al., *A comparative study of the mechanical strength of chemical vapor-deposited diamond and physical vapor-deposited hard coatings.* Thin Solid Films, 2005. **473**(1): p. 123-131.
38. Bouzakis, K.-D., et al., *The inclined impact test, an efficient method to characterize coatings' cohesion and adhesion properties.* Thin Solid Films, 2004. **469-470**: p. 254-262.
39. Bouzakis, K.-D. and A. Siganos, *Fracture initiation mechanisms of thin hard coatings during the impact test.* Surface and Coatings Technology, 2004. **185**: p. 150-159.
40. Lima, M.M., et al., *Coating fracture toughness determined by Vickers indentation: an important parameter in cavitation erosion resistance of WC-Co thermally sprayed coatings.* Surface and Coatings Technology, 2004. **177-178**: p. 489-496.
41. Curran, J.A. and T.W. Clyne, *Thermo-Physical Properties of Plasma Electrolytic Oxide Coatings on Aluminium.* Surface and Coatings Technology, 2004.
42. Xue, W.B., *Analysis of Phase Distribution for Ceramic Coatings formed by Microarc Oxidation on Aluminium Alloy.* J. Amer. Ceram. Soc., 1998. **81**(5): p. 1365-1368.
43. Meneve, J.L., et al., *Surface mechanical property testing by depth sensing indentation.* Applied Surface Science, 1996. **100-101**: p. 64-68.
44. Vanacker, K., et al., *Characterization of Thin Nickel Electrocoatings by the Low-Incident-Beam-Angle Diffraction Method.* Journal of Applied Crystallography, 1994. **27**: p. 56-66.
45. Tsui, Y.C. and T.W. Clyne. *Adhesion of Thermal Barrier Coating Systems and Incorporation of an Oxidation Barrier Layer*. in *Thermal Spray: Practical Solutions for Engineering Problems. Proceedings of the 9th Nat. THermal Spray Conf.* 1996. Cincinatti: ASM.
46. Gedda, H., Journal of Laser Applications, 2002. **14**(2): p. 78.
47. Fanous, I.F.Z., Trans., 2003. **125**: p. 144.
48. Mills, K.C., *Recommended values of thermophysical properties for selected commercial alloys.* 2002, UK.
49. *ISO 5725 Part 2 - Accuracy (trueness and precision) of measurement methods and results*. 1994.

Distribution list

D. Harmegnies Project Officer	– Belgian Federal Science Policy Office	– 1 copy + electronic version
F. Delannay	– UCL	– electronic version
S. Ryelandt	– UCL	– electronic version
E. Deleu	– BIL	– electronic version
A. Dhooge	– BIL	– electronic version
K. De Bruyn	– WTCM	– electronic version
A. Plati	– UCambridge	– electronic version
T.W. Clyne	– UCambridge	– electronic version
Karel Van Acker	– Vito	– 1 original
Rosita Persoons	– Vito	– electronic version
SecMat	– Vito	– 2 copies
H. Delrue	– Bekaert VDS	– 1 copy
F. Hindryckx	– Techspace-Aero	– 1 copy
M. De Bonte	– VOM	– 1 copy
B. Vandewiele	– Surface Treatment Company	– 1 copy
A. Van Acker	– VATIS bvba	– 1 copy
D. Van Dromme	– VVM De Lijn	– 1 copy
A. Laret	– RMI	– 1 copy